Politecnico di Torino

Department of Mechanical, Aerospace
and Automotive Engineering

Master of Science in Aerospace Engineering

Master Thesis

Study of a Nonlinear Dynamic Model of Vortex Ring State for Bell 412 Helicopter

Supervisor
Prof.ssa Elisa CAPELLO
Co-advisor
Dr. Linghai LU

Candidate
Marco LALLONI

Academic Year
2024-2025

Contents

List of Figures

List of Tables

Nomenclature

Latin letters

$\ddot{a_0}$ Coning angle accelereration [rad/s^2]

$\ddot{a_1}$ Longitudinal angle acceleration [rad/s^2]

$\ddot{b_1}$ Lateral angle acceleration [rad/s^2]

$\dot{a_0}$ Coning angle velocity [rad/s]

$\dot{a_1}$ Longitudinal angle velocity [rad/s]

$\dot{b_1}$ Lateral angle velocity [rad/s]

$\tilde{D}$ TPP damping matrix

$\tilde{f}$ TPP forcing matrix

$\tilde{K}$ TPP stiffness matrix

$\vec{r_B}$ Center of gravity position vector

$\vec{V_B}$ Body velocities vector

$\vec{V_L}$ Local velocities vector

A Surface [m^2]

a Main rotor blade lift slope [1/rad]

a_0 Coning angle [rad]

a_1 Longitudinal TPP angle [rad]

a_T Tail rotor blade lift slope [1/rad]

A_{1c} Lateral cyclic in wind-hub axes [rad]

b_1 Lateral TPP angle [rad]

B_{1c} Longitudinal cyclic in wind hub axes [rad]

c Mean chord [m]

C' Inflow deficency factor

c_i Cosine(-) [rad]

C_l, C_d Lift and drag coefficient

C_T Thrust coefficient

$C_X, C_Y, C_Z, C_L, C_M, C_N$ Force and moment coefficient

C_{d_0}, C_{d_1} First and second order drag coefficient [1/rad]

C_{l_α} Lift slope coefficent [1/rad]

eR Hinge offset [m]

F_T Tail rotor blockage factor

g Gravity acceleration [m/s^2]

h Vertical distance from the center of gravity [m]

I_β Flapping inertia of the blade [kg m^2]

is Tilt angle of the main rotor [rad]

is	Tilt angle of the main rotor [rad]
k_3	Pitch-roll coupling ratio [rad]
K_β	Blade flapping stiffness [Nm/rad]
k_λ	Main rotor downwash factor
l	Longitudinal distance from the center of gravity [m]
N_b	Number of blades
p, q, r	Angular rates [rad/s]
R	Radius [m]
S	Surface [m^2]
s_i	Sine(-) [rad]
T	Thrust [N]
u_r, u_t, u_p	Radial,tangential and in plane velocity of the blade [m/s]
v_∞	Velocity [m/s]
v_c	Climb velocity [m/s]
v_h	Hover induced velocity [m/s]
v_i	Induced velocity [m/s]
w_λ	Induced velocity on the fuselage [m/s]
w_H	Vertical velocity [m/s]
x, y, z	Position [m]

Greek letters

α	Incidence angle [rad]
α_0	Initial incidence [rad]
β	Sideslip angle [rad]
$\beta_0, \beta_{1s}, \beta_{1c}$	Coning, lateral and longitudinal flapping angle [rad]
β_w	Rotor sideslip angle [rad]
χ	Wake angle [rad]
δ	Blade drag coefficient [1/rad]
δ_0, δ_2	First and second order drag coefficient [1/rad]
ϵ	Hinge-offset to radius ratio
γ	Lock number
λ	Adimensional induced velocity
λ_β	Flapping frequency [Hz]
λ_{0T}	Tail rotor adimensional induced velocity
$\lambda_{1_{cw}}$	Longitudinal inflow
μ	Advance ratio
μ_d	Vertical advance ratio
Ω	Rotor angular velocity [rad/s]
ϕ	Roll angle [rad]
ψ	Azimuth angle [rad]
ρ	Density [kg/m^3]
σ	Solidity
θ	Pitch angle [rad]
$\theta_0, \theta_{1s}, \theta_{1c}, \theta_{0T}$	Collective,longitudinal cyclic, lateral cyclic, pedal [rad]
θ_{tw}	Blade twist [rad]
$\vec{\omega_B}$	Body angular rates vector

Subscripts

b	Body
fn	Vertical fin
h	Hub
R	Main rotor
T	Tail rotor
tp	Tail plane
w	Wind

Acknowledgements

Abstract

The main objective of this thesis is to develop a Level 1 simulator specifically for the Bell 412 helicopter to study the Vortex Ring State (VRS). This is an unsteady aerodynamic condition that occurs at certain descent rates and low forward speeds. Entering the VRS causes a sudden loss of thrust, an increase in descent rate and a loss of controllability. It is therefore necessary that the flight envelope avoids this possibility and, if this state occurs, pilots are trained in recovery manoeuvres to get out. This is the context in which the project was developed to provide a satisfactory model for possible pilot training. It was divided into the following phases: modelling, trim evaluation, validation, development and implementation of VRS models. First, a non-linear model of the helicopter was built in the Matlab-Simulink environment. The main elements of an helicopter were modelled, while the engine was considered ideal. Next, the trim was studied. This is in fact the necessary starting condition for any simulation and the assessment of a good equilibrium point is therefore crucial for the progress of the project. The model was then validated by time scale comparison with results from FlightLab, an high fidelity simulator developed and validated as part of a joint project between the University of Liverpool and the National Research Council of Canada. Different flight conditions were analysed, to cover as wide a range as possible to confirm the validity of the model. The simulations were carried out with a doublet input of collective, longitudinal cyclic, lateral cyclic and pedal. Once the model was validated, the next step was to develop algorithms that would describe the variation of the inflow during the descent and thus allow the development of VRS to be observed or not. Two models were therefore studied: Young and Jhonson. A validation was also carried out by comparing them on a time scale with the results obtained by FlightLab, focusing in particular on the variation of the climb rate and the activation of the VRS. The model described by Jhonson gives satisfactory results and is suitable for the purpose of the project.

Chapter 1

Introduction

1.1 The role of helicopters

The development of helicopters and VTOL aircraft has opened the door to numerous applications unthinkable with fixed-wing aircraft. In 1940, engineer Igor Sikorsky took the first step towards the definitive development of this aviation milestone, creating the first modern helicopter. From that moment on, the applications of this machine ranged from simple transport to rescue, from civil to military use. Despite significant disadvantages, including slower speed, limited range, noise and high cost, they are actually indispensable. Indeed, helicopters offer unique flight capabilities such as hovering, vertical take-off and landing, lateral and reverse flight. In addition, their axial flight ability allows them to reach difficult terrain and hover over a target without landing.

These important features make the helicopters suitable for the following applications:

- Rescuing and recovering in extreme environments
- Transporting goods and people in mountainous or offshore environments
- Transporting private
- Operating in both offensive and defensive military scenarios
- Patrolling and controlling operations

1.2 Challenges

Although the above advantages are undoubtedly important for commercial applications, the absence of a fixed wing and the introduction of two rotors introduce some rather complex challenges. In addition to vibrations, resonance problems and gyroscopic coupling, the introduction of the main rotor as a replacement for the fixed wing is particularly important from

Figure 1.1: First helicopter flight in 1939 [2]

a safety point of view. In the event of an engine failure resulting in the loss of propulsion, the only safety manoeuvre is autorotation. Furthermore, the fact that a tail rotor is generally used as an anti-torque function for the main rotor means that its loss or damage would result in a loss of control of the rotorcraft.

Moreover, the possibility of steep or even vertically descending, introduces problems from an aerodynamic point of view as well. In fact, the irregular circulation of the airflow through the rotor and its stagnation in the plane of the blades causes vortex formation and entry into unsteady states such as the Vortex Ring State. This can occur at both high descent rates and high ramp angles. The key factor is that the descent velocity is comparable to the module of the velocity normal to the disc. In this way, the wake formed by the blades cannot be ejected away, but accumulates in the plane of the rotor, forming a turbulent flow. The mean thrust experiences a significant reduction, accompanied by intense oscillations, a loss of control authority, and potential reversals in cyclic and collective control. The aerodynamic nature of the VRS phenomenon is closely linked to the aircraft's dynamic response, flight mechanics, and the pilot's reaction to the developing instability. If not promptly corrected, this condition can result in a rapid, uncontrolled descent with potentially severe consequences. In view of its dangerousness, it is essential to have tools that are useful not only for studying

the inner limits of the flight envelope, but also for training pilots in the prevention of this state and the aircraft's recovery should it occur. Hence the need to implement algorithms in real-time simulators for training in these techniques.

1.3 Role of flight simulation

The availability of simulators makes it possible to study the flight envelope and train pilots in a safer and more economical way. In fact, numerical simulations, when properly validated, are a reliable tool for describing the dynamic behaviour of aircraft and offer not negligible advantages:

– Economic savings in fuel and aircraft maintenance
– Increased safety for instructors and pilots during the training phase
– The ability to train one-shot manoeuvres such as autorotation or recovery from unstable conditions
– Ability to safely study flight envelope extensions
– Ability to optimise flight hours for training
– Low environmental impact

In this context, flight simulators play a crucial role, leading to a distinction based on the purpose for which they are designed. Ground simulators can then be divided into:

– Training simulators, designed to train pilots or personnel in manoeuvres and procedures.
– Research simulators, designed to study new aircraft architectures and flight control system and extend the flight envelope.

1.4 FlightLab

FlightLab is a state of art sowftare for helicopter flight simulation developed by Advanced Rotorcraft Technolgy (ART) to perform various engineering task, from design to stability and control evaluation to pilot training. In particular, this software is used within the Heliflight-R Flight Simulator at the University of Liverpool. This is a reconfigurable research simulator for different types of helicopters and is also certified at level 5 by the FAA for pilot training. It was also used to create the Bell412 simulator with which the model developed in this thesis was validated, as reported in 3.

Figure 1.2: HeliFlight-R flight simulator of Liverpool University [2]

1.5 Bell 412

The Bell 412 is a four-bladed, semi-rigid-rotor helicopter that was developed as an upgrade of its predecessor, the Bell 212. It was developed by the American company Bell from the late 1970s and made its first flight in August 1979. It was then officially certified by the FAA in 1981 and marketed for civil, rescue and military purposes. To the present day, it has been produced in eleven different variants and over a thousand have entered service. General characteristics are reported in table:

Maximum speed	260 km/h
Maximum range	611 km
Service ceiling	5897 m
Maximum take off weight	5398 kg
Capacity	1-2 pilots + up to 13 passenger
Engines	2 turboshaft Pratt&Whitney

Table 1.1: Bell 412 performance

The Bell 412 used as a reference belongs to the National Council Research of Canada and was used for research purposes. In particular, the test campaign from which the data were obtained was part of a project to develop a high-fidelity flight simulator to study new flight control laws for handling qualities improvement. All the data used are therefore taken from the report [9], result of a collaboration between the University of Liverpool and NCR.

Figure 1.3: NCR Bell 412 [9]

Chapter 2

Helicopter modeling

2.1 Assumptions

The mathematical modelling of an helicopter is quite a difficult task, as it is made up of several components that must work together to ensure the perfect functioning of the machine. The presence of two rotors causes gyroscopic coupling, out-of-phase responses along the revolution depending on the input, and vibratory phenomena that affect performance. In addition, the main rotor is the source of aerodynamic interference on the other components due to the variation of the downwash, so that the response and efficiency of each component is affected by the flight condition and the state of the rotor. The mathematical description of the helicopter assembly is therefore very complex and delicate. In terms of component function, the main rotor is responsible for generating the thrust required for hovering, axial and directional flight. The torque required to move it is provided by the engines. The tail rotor, on the other hand, counterbalances the torque experienced by the fuselage in response to that generated by the main rotor. It is therefore responsible for directional stability.

It is undoubtedly very important to understand the mechanism of the two rotors in the generation of forces and moments. As far as the main rotor is concerned, the simultaneous variation of the pitch of all the blades leads to an increase in thrust, which in turn leads to an increase in torque. It is therefore necessary, following a collective command, to also increase the pitch of the tail rotor. By varying the pitch of the main rotor along the revolution, the effect is a directional change in thrust. This is followed by a moment imbalance and a consequent longitudinal or lateral angular rates response.

Before constructing an helicopter model, it is important to define its purpose. As suggested by Padfield [6], the level of complexity of a mathematical model varies depending on its application. As shown in table 2.1, if the objective is to study the flight dynamics of the

helicopter - for example, to design a low-bandwidth flight controller or to analyse the operational envelope of the aircraft - the rotor blades can be modelled as rigid bodies that can move freely in flap, lead-lag and pitch directions relative to the hub, either through a physical or virtual hinge, and subjected to 2D steady-state aerodynamics. Since the purpose of this thesis is to develop a flight dynamics model for an helicopter, the level 1 modelling approach has been chosen.

Aerodynamics	Dynamics	Applications
linear 2D dynamic	rigid blades	parametric trends for flying
inflow/local momentum theory	(1) quasi steady motion	qualities and performance studies
analitically integrated	(2) 3 DoF flap	well within operational flight envelop
	(3) 6 DoF flap+lag	low bandwith control
	(4) 6 DoF flap+lag+ quasy steady torsion	

Table 2.1: Type 1 flight simulator

2.2 Reference system

Referring to the figure 2.1,the following frames are used.
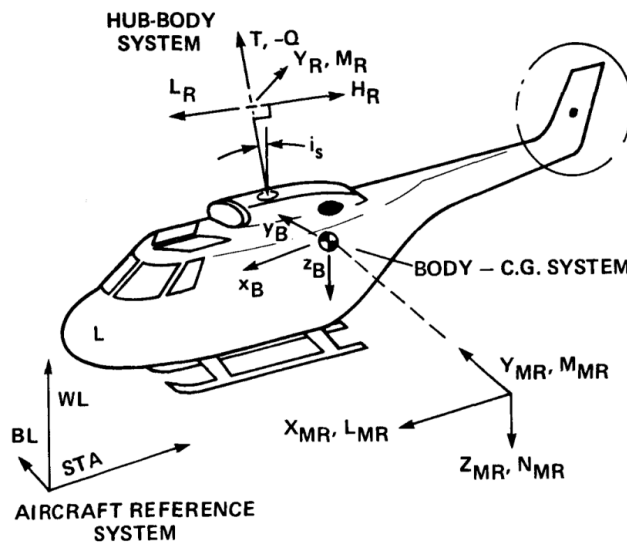
Figure 2.1: Reference systems [3]

NED frame

The NED (North, East, Down) reference system, considered as an inertial for brief time, is used to evaluate the kinematics. The z-axis (Down) points downwards, the x-axis (North) towards the bow of the helicopter and the y-axis (East) is outgoing to the pilot's right.

7

Aircraft reference system

Aircraft reference system is used to measure typical reference lengths and mutual distances of helicopter parts. Referring to 2.1, the origin is located below the fuselage 20 inches inboard. The x-axis, which indicates the station line, points towards the tail, the z-axis, known as the waterline, points upwards, and the y-axis, the buttline, points to the pilot's right.

Body frame

The body frame is centered in the CoG of the helicopter and is oriented as the NED system. Used to evaluate the total forces and moments to study the dynamics, is attached to the CoG. To change from the body reference system to the NED reference system, the following series of rotations is carried out:

– rotation around the z-axis of the azimuth angle ψ
– rotation around the y'-axis of the pitch angle θ
– rotation about the x"-axis of the roll angle ϕ

In a matrix form results:

$$\begin{bmatrix} x_0 \\ y_0 \\ z_0 \end{bmatrix}_{NED} = \begin{bmatrix} c_\theta c_\psi & -c_\theta s_\psi + s_\phi s_\theta c_\psi & s_\phi s_\psi + c_\phi s_\theta c_\psi \\ c_\phi s_\psi & c_\phi c_\psi + s_\phi s_\theta s_\psi & -s_\phi c_\psi + c_\phi s_\theta s_\psi \\ -s_\theta & s_\phi c_\theta & c_\phi c_\theta \end{bmatrix} \begin{bmatrix} x \\ y \\ z \end{bmatrix}_b \tag{2.1}$$

Wind frame

The wind frame is aligned with the total velocity and used to evaluate the aerodynamic forces. The orientation of that frame changes with the flight conditions. The x-axis is aligned with the total velocity vector, the z-axis point downwards and the y-axis concludes the right-handed system.

Changing from a wind frame to a body frame is required and achieved thanks to the following rotations:

– rotation about the z-axis of the sideslipe angle β
– rotation about the y'-axis of the incidence angle α

It results the above equation:

$$\begin{bmatrix} x \\ y \\ z \end{bmatrix}_b = \begin{bmatrix} c_\alpha c_\beta & -c_\alpha s_\beta & -s_\alpha \\ s_\beta & c_\beta & 0 \\ s_\alpha c_\beta & -s_\alpha s_\beta & c_\alpha \end{bmatrix} \begin{bmatrix} x \\ y \\ z \end{bmatrix}_w \tag{2.2}$$
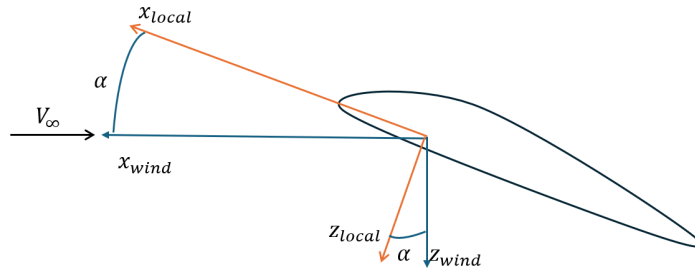
Figure 2.2: Wind system

Hub frame

In the hub reference system, rotor forces are evaluated in the rotor plane. It is a fixed reference system and centred in the shaft. The z-axis points upwards, the x-axis points towards the aft and the y-axis completes the right-hand tern. To change from a hub reference system to a body reference system, the following transformations must be performed:

 – rotation about the z-axis of the sideslipe angle β

 – rotation about the y'-axis of the tilt angle is

It results the above equation:

$$
\begin{bmatrix} x \\ y \\ z \end{bmatrix}_b = \begin{bmatrix} c_{is}c_\beta & -c_{is}s_\beta & -s_{is} \\ s_\beta & c_\beta & 0 \\ s_{is}c_\beta & -s_{is}s_\beta & c_{is} \end{bmatrix} \begin{bmatrix} x \\ y \\ z \end{bmatrix}_h
\tag{2.3}
$$
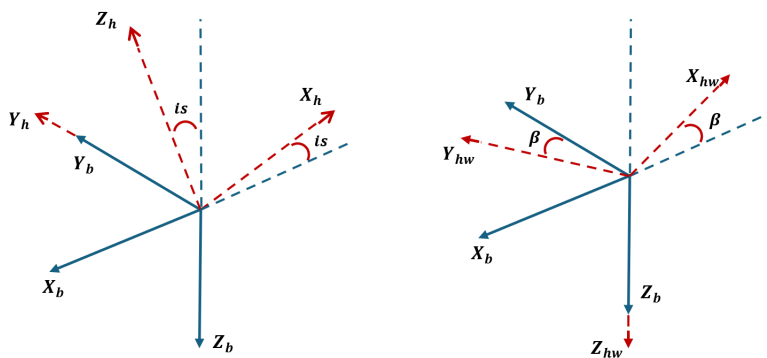
Figure 2.3: Hub-wind system

Reference plane

For the present work, equations of the main rotor are referred to the Tip Path Plane. This is the plane described by the blade tips and is commonly used to perform aerodynamic analisys.
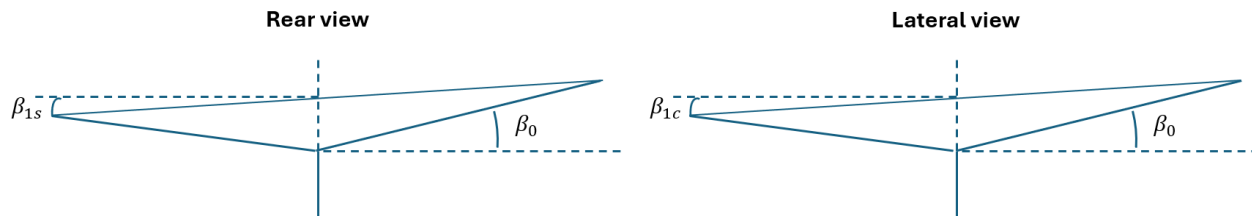
Figure 2.4: Tip Path Plane

2.3 Main rotor

The main purpose of the rotor is to produce thrust. Many theories have been developed to describe this phenomena, starting from the simple Momentun Theory and arriving to the more complex Blade Element Momentum Theory.

2.3.1 Momentum Theory

The main rotor is approximated as a solid disc of infinitesimal thickness. Considering a flow tube passing through the rotor disc, the three laws of conservation of mass, momentum and energy can be applied to the two control volumes shown in figure 2.5. The simplicity of this theory does not allow the study of phenomena such as the aerodynamic interaction of the blades, nonlinear or non-uniform inflow or the study of the behavior of individual blades. Furthermore, thrust is simply approximated as a jump pressure through the disk. It is therefore used as a first approximation to study rotor performance in terms of thrust and power generated in a given flight condition and for a given rotor size.

Referring to Leishman [7], in hover thrust is given by:

$$T = 2\rho A v_i^2 \tag{2.4}$$

By inverting the equation, the induced velocity can be calculated as follows:

$$v_h = v_i = \sqrt{\frac{T}{2\rho A}} \tag{2.5}$$

10
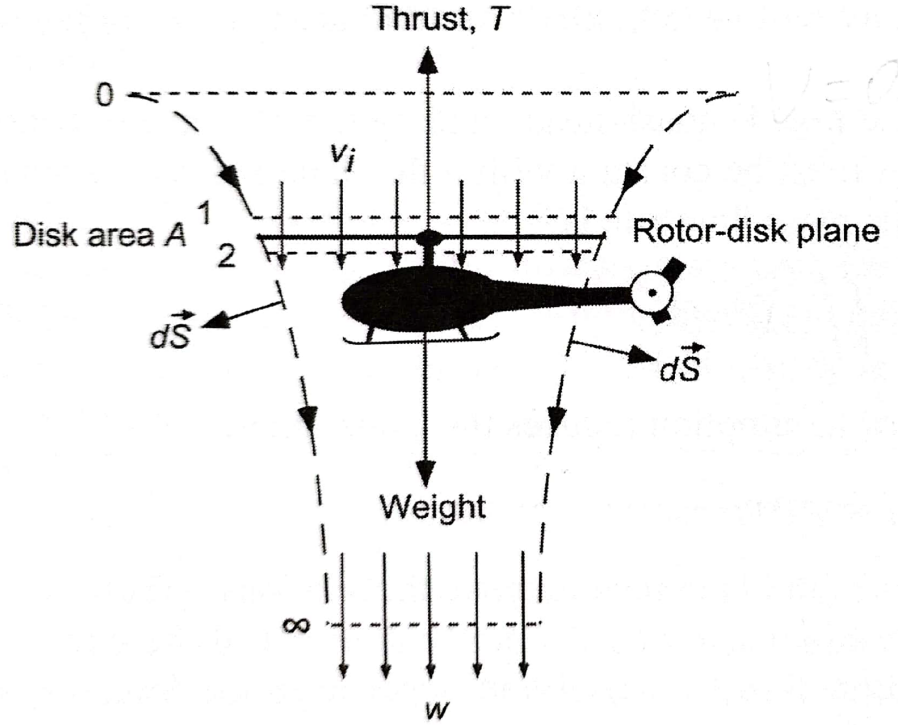
Figure 2.5: Momentum theory control volume [7]

Developing for the forward flight, it results:

$$T = 2\rho A v_i \sqrt{(V_\infty cos\alpha)^2 + (V_\infty sin\alpha + v_i)^2} \tag{2.6}$$

where:

$$v_i = \frac{v_h^2}{\sqrt{(V_\infty cos\alpha)^2 + (V_\infty sin\alpha + v_i)^2}} \tag{2.7}$$

Both for the hover and forward flight conditions the thrust coefficient is evaluated as:

$$C_T = \frac{T}{\rho \pi R^2 V^2} \tag{2.8}$$

2.3.2 Blade Momentum Theory

This theory allows the study of aerodynamic loads along the blade radial and azimuthal direction. Each blade is divided into a finite number of stations where the loads are calculated and then integrated on the blade radius, as shown in figure 2.6.

11
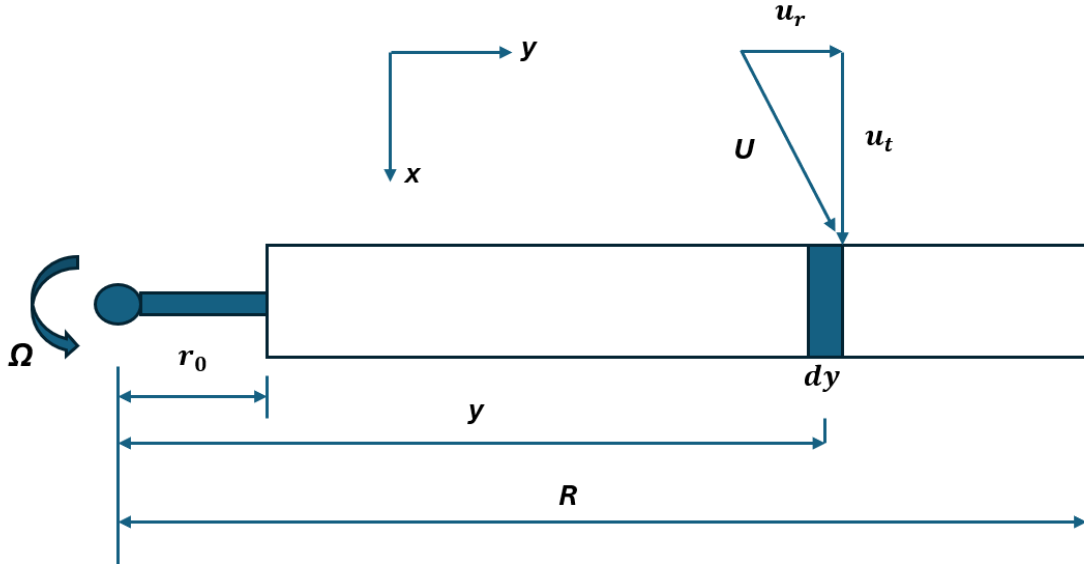
Figure 2.6: Incident velocity and radial decomposition of the blade
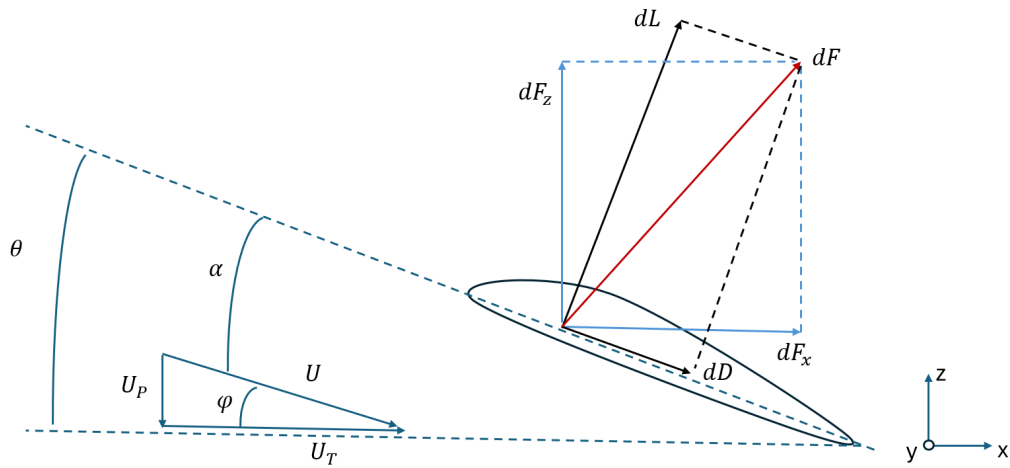
Figure 2.7: Incident velocity and loads decomposition on the blade section

Referring to the figure 2.7 and following Leishman explanation, the total velocity investing the blade section is given by:

$$U = \sqrt{U_t^2 + U_P^2} \tag{2.9}$$

12

while the angle of attack induced by the velocity is equal to:

$$\phi = tan^{-1}\left(\frac{U_P}{U_t}\right) \tag{2.10}$$

From this, we obtain that the effective incidence of the blade is:

$$\alpha = \theta - \phi = \theta - tan^{-1}\left(\frac{U_P}{U_t}\right) \tag{2.11}$$

With which the lift and drag are calculated as:

$$dL = \frac{1}{2}\rho C_l U^2 c dy \tag{2.12}$$

$$dD = \frac{1}{2}\rho C_d U^2 c dy \tag{2.13}$$

By decomposing the two forces along the normal and parallel direction to the disc, the resultant components can be evaluated:

$$dF_z = dL cos\phi - dD sin\phi \tag{2.14}$$

$$dF_x = dL sin\phi + dD cos\phi \tag{2.15}$$

These are finally used to evaluate thrust and torque:

$$dT = N_b dF_z \tag{2.16}$$

$$dQ = N_b dF_x y \tag{2.17}$$

Using the BET, thrust coefficient is evaluated taking into account the contribution of the collective input, blade twist and local inflow. Assuming linear twist and uniform inflow, it is then equal to:

$$C_T = \frac{1}{2}\sigma C_{l_\alpha}\left[\frac{\theta_0}{3} + \frac{\theta_{tw}}{4} - \frac{\lambda}{2}\right] \tag{2.18}$$

2.3.3 Blade Element Momentum Theory

Combining the two theories described above results in the Blade Element Momentum Theory, which allows the estimation of inflow distribution along the blade. This theory splits the rotor disc into infinitesimal annuli along which aerodynamic loads and inflow are calculated, as can be seen in figure 2.8. The values obtained for the individual annulus are then integrated on the disc to compute the total loads.
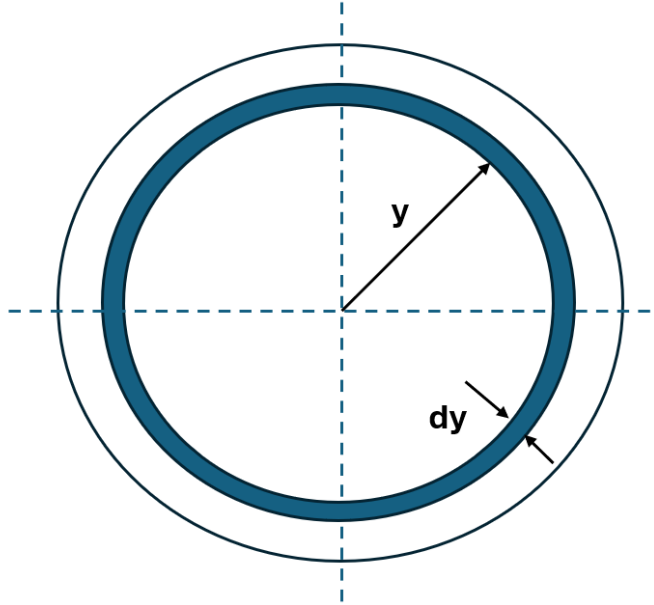
Figure 2.8: Disk rotor subdivision

Applying the conservation laws, thrust is given by:

$$dT = 4\pi\rho \left(V_c + v_i\right) y\, dy \tag{2.19}$$

It is then possible to evaluate the thrust coefficient as:

$$dC_T = 4\lambda\lambda_i r\, dr \tag{2.20}$$

It can be seen that in this case the two equations depend not only on the axial velocity, but also on the radial position and the induced velocity.

2.3.4   Main rotor inflow

The velocity flow through the rotor has a rather complex composition of vortices and regions where the flow reverses. For a precise study, tools such as computational fluid dynamics should be used, but these are computationally too expensive to be implemented in a real time flight simulator. The theories described above therefore provide a formulation that is simpler but still able to consider the evolution of the flow along the blade. Under hover conditions, the flow is symmetrical on the disc, as can be seen in the picture 2.9.
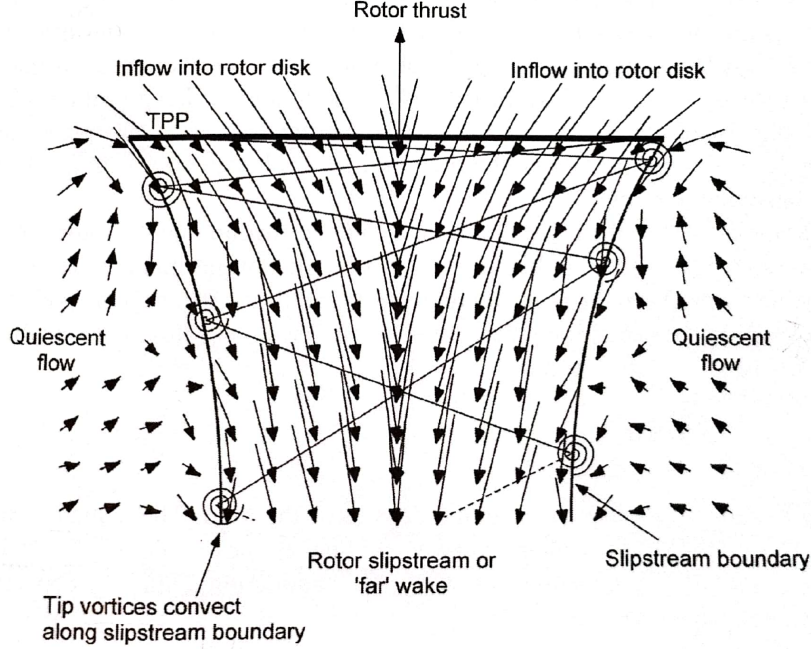
Figure 2.9: Hover velocity flow [7]

According to Momentum Theory, the inflow in this condition is evaluated as:

$$\lambda_h = \sqrt{\frac{C_T}{2}} \tag{2.21}$$

where C_T is given by equation 2.8. Using instead the BET or the BEMT, the thrust coefficient results from equation 2.18 or 2.20.

In axial flight, a more complex flow field develops, and the simultaneous contribution of induced velocity and axial velocity must be considered. The inflow value can then be calculated from momentum theory by solving the quadratic equation:

$$\left(\frac{v_i}{v_h}\right)^2 + \frac{V_c}{v_h}\left(\frac{v_i}{v_h}\right) = 1 \tag{2.22}$$

The simplest case is the climb phase, for which the solution is given by:

$$\frac{v_i}{v_h} = -\left(\frac{V_c}{2v_h}\right) + \sqrt{\left(\frac{V_c}{2v_h}\right)^2 + 1} \tag{2.23}$$

More complex is the descent phase, during which the rotor can find itself in very different situations due to the development of vortices along the radius and unsteady aerodynamic phenomena such as the Vortex Ring State can arise. From 2.22, the equation that results at

15

this stage is:

$$\frac{v_i}{v_h} = -\left(\frac{V_c}{2v_h}\right) - \sqrt{\left(\frac{V_c}{2v_h}\right)^2 + 1} \tag{2.24}$$

However, equation 2.24 is only valid for $\mu_d/\lambda_h < -2$, since between the range $-2 \leq \mu_d/\lambda_h \leq 0$ more complex phenomena happen and momentum theory is no longer valid, as reported in the figure 2.10. Other mathematical models are then needed and they will be discussed in the chapter 4.
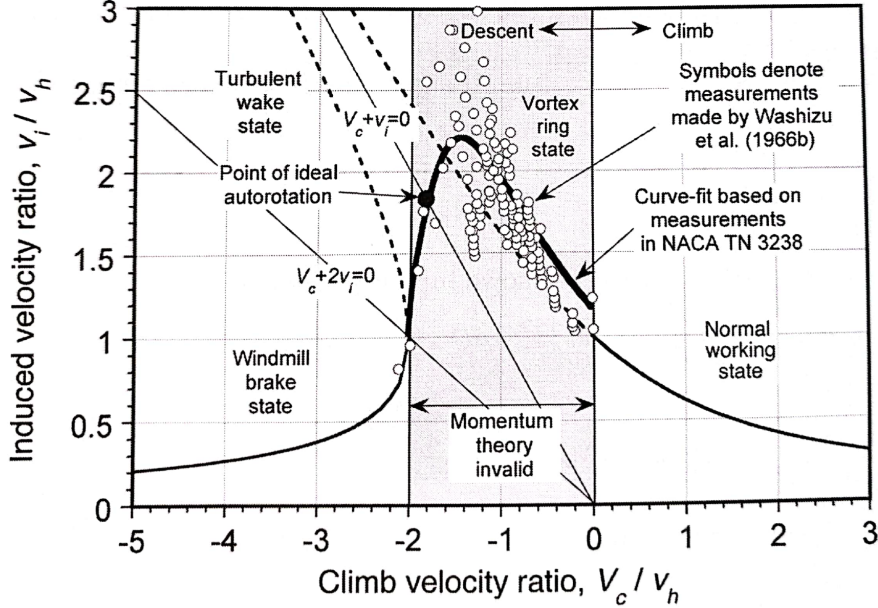
Figure 2.10: Range of validity of the Momentum Theory [7]

In the case of advanced flight, referring to the model presented by Chen [3], the inflow is described as follows:

$$\lambda_0 = \frac{w_H}{\Omega R} - \frac{C_T}{2\sqrt{\mu^2 + \lambda^2}} \tag{2.25}$$

The equation is solved iteratively through the Ralphson-Newton method using as initial condition the value calculated in the trim conditions.

The flight conditions in which there is the greatest non-uniformity in terms of inflow are those of transition from hover to forward flight, between $0 \leq \mu \leq 0.1$. During this phase, the presence of vortices at the blade tips and their movement along the rotor plane cause the greatest imbalance in terms of induced velocity. Padfield [6] proposed the following model

to take into account the non linearity of the inflow during this transition phase:

$$\lambda_i = \lambda_0 + \frac{r_b}{R}\lambda_{1cw}cos\psi_w \tag{2.26}$$

where λ_{1cw} is function of the wake angle:

$$\lambda_{1cw} = \lambda_0 tan\left(\frac{\chi}{2}\right), \quad \chi < \frac{\pi}{2} \tag{2.27}$$

$$\lambda_{1cw} = \lambda_0 cot\left(\frac{\chi}{2}\right), \quad \chi > \frac{\pi}{2} \tag{2.28}$$

The wake angle is given by the expression:

$$\chi = tan^{-1}\left(\frac{\mu}{\lambda_0 - \mu_z}\right) \tag{2.29}$$

One of the weaknesses of Momentum Theory is that it cannot evaluate transients, but only stationary conditions or those of slow maneuvers. In order to take into account these conditions, a deficency function is used, as proposed by Padfield [6], such that the thrust coefficient is penalised by a factor dependent on the inflow speed or the forward ratio. The variation of the thrust coefficient can therefore be described as follows:

$$\delta C_T = C'\delta C_{T_{QS}} \tag{2.30}$$

where:

$$C' = \frac{1}{1 + \frac{a_0 s}{16\lambda_i}} \quad , \mu = 0 \tag{2.31}$$

$$C' = \frac{1}{1 + \frac{a_0 s}{8\mu}} \quad , \mu > 0.2 \tag{2.32}$$

2.3.5   Flapping dynamic

The action of aerodynamic loads along the revolution characterises the typical dynamics of the blade, namely flapping and lead-lag. With respect to the flapping dynamics, the blade flaps up or down out of the plane around the flapping hinge.
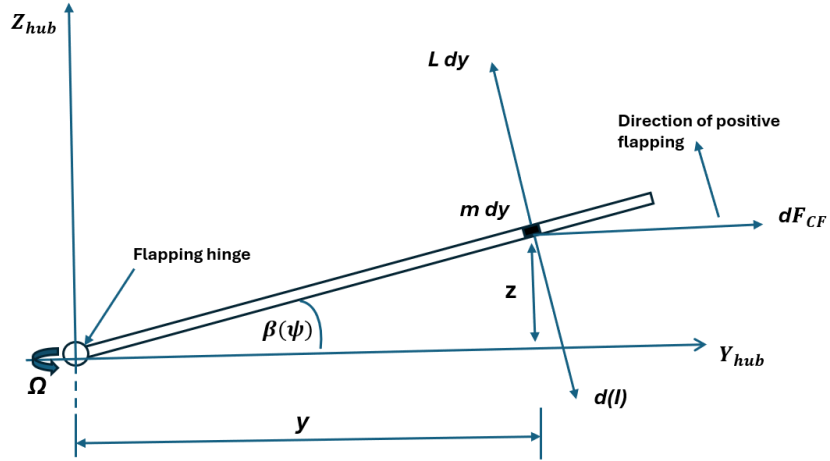
Figure 2.11: Blade free body diagram around the flapping hinge

Looking at the figure 2.11, it is possible to derive the flapping dynamics equation, which turns out to be:

$$\int_0^R m\Omega^2 \beta y \, dy + \int_0^R m\ddot{\beta}y^2 \, dy - \int_0^R Ly \, dy = 0 \tag{2.33}$$

The first term represents the centrifugal moment around the flapping hinge, the second is the blade moment of inertia, while the third considers the aerodynamic moment around the flapping hinge. The lift is obtained according to the BET or BEMT.

2.3.6   Tip Path Plane formulation

Equations used for the main rotor are presented by Chen in [3]. They describe the rotor dynamics in the Tip Path Plane. This formulation is obtained from the Blade Element Momentum Theory with the following assumptions:

  – Rigid blades
  – Small flapping and inflow angle
  – Flapping affected only from the angular accelerations $\dot{p}, \dot{q}$ and angular rates p,q
  – Reversed flow ignored
  – Uniform inflow
  – Tip loss factor assumed equal to one

The flapping dynamics is described by a second-order system with the following formulation:

$$\ddot{a} + \tilde{D}\dot{a} + \tilde{K}a = f \tag{2.34}$$

The damping, stiffness and forcing matrix are reported below:

$$
\tilde{D} = \Omega \begin{bmatrix} \frac{\gamma}{2}\left(\frac{1}{4} - \frac{2}{3}\epsilon + \frac{\epsilon^2}{2}\right) & 0 & -\frac{\gamma}{4}\left(\frac{1}{3} - \epsilon + \epsilon^2\right) \\ 0 & \frac{\gamma}{2}\left(\frac{1}{4} - \frac{2}{3}\epsilon + \frac{\epsilon^2}{2}\right) & 2 \\ -\frac{\gamma}{2}\left(\frac{1}{3} - \epsilon + \epsilon^2\right) & -2 & \frac{\gamma}{2}\left(\frac{1}{4} - \frac{2}{3}\epsilon + \frac{\epsilon^2}{2}\right) \end{bmatrix} \tag{2.35}
$$

$$
\tilde{K} = \Omega^2 \begin{bmatrix} P^2 + \gamma K_1 \mu^2 \frac{1}{4}\left(\frac{1}{2} - \epsilon + \frac{\epsilon^2}{2}\right) & -\frac{\gamma\mu}{4}\left(\frac{\epsilon}{2} - \epsilon^2\right) & -\gamma K_1 \mu \frac{1}{4}\left(\frac{2}{3} - \epsilon\right) \\ -\frac{\gamma\mu}{2}\left(\frac{1}{3} - \epsilon + \frac{\epsilon^2}{2}\right) & P^2 - 1 + \frac{\gamma K_1 \mu^2}{8}\left(\frac{1}{2} - \epsilon + \frac{\epsilon^2}{2}\right) & \frac{\gamma}{2}\left(\frac{1}{4} - \frac{2}{3}\epsilon + \frac{\epsilon^2}{2}\right) + \frac{\gamma\mu}{8}\left(\frac{1}{2} - \epsilon + \frac{\epsilon^2}{2}\right) \\ -\gamma K_1 \mu \frac{1}{2}\left(\frac{2}{3} - \epsilon\right) & -\frac{\gamma}{2}\left(\frac{1}{4} - \frac{2}{3}\epsilon + \frac{\epsilon^2}{2}\right) + \frac{\gamma\mu}{8}\left(\frac{1}{2} - \epsilon + \frac{\epsilon^2}{2}\right) & P^2 - 1 + \frac{3}{8}\gamma K_1 \mu^2 \left(\frac{1}{2} - \epsilon + \frac{\epsilon^2}{2}\right) \end{bmatrix} \tag{2.36}
$$

$$
\tilde{F} = \Omega^2 \begin{bmatrix} -\frac{M_\beta}{I_B \Omega^2} + \frac{\gamma}{2}\left[\left(\frac{1}{4} - \frac{\epsilon}{3}\right) + \frac{\mu^2}{2}\left(\frac{1}{2} - \epsilon + \frac{\epsilon^2}{2}\right)\right]\theta_0 - \frac{\gamma}{2}\left[\mu\left(\frac{1}{3} - \frac{\epsilon}{2}\right)\right]B_{1c} + \frac{\gamma}{2}\left[\left(\frac{1}{5} - \frac{\epsilon}{4}\right) + \frac{\mu^2}{2}\left(\frac{1}{3} - \frac{\epsilon}{2}\right)\right]\theta_t + \frac{\gamma}{2}\left(\frac{1}{3} - \frac{\epsilon}{2}\right)\lambda \\ +\frac{\gamma}{8}\mu\left(\frac{2}{3} - \epsilon\right)\left(\frac{p_h}{\Omega}\cos\beta_w + \frac{q_H}{\Omega}\sin\beta_w\right) \\[2mm] -2\left(1 + \frac{eM_\beta}{gI_\beta}\right)\left(\frac{p_H}{\Omega}\cos\beta_w + \frac{q_H}{\Omega}\sin\beta_w\right) + \left(\frac{\dot{p}_H}{\Omega^2}\cos\beta_w - \frac{\dot{q}_H}{\Omega^2}\sin\beta_w\right) + \frac{\gamma}{2}\left[\left(\frac{1}{4} - \frac{\epsilon}{3}\right) + \frac{\mu^2}{4}\left(\frac{1}{2} - \epsilon + \frac{\epsilon^2}{2}\right)\right]A_{1c} \\ +\frac{\gamma}{2}\mu\left(\frac{1}{4} - \frac{\epsilon}{3}\right)\left(\frac{p_h}{\Omega}\sin\beta_w - \frac{q_H}{\Omega}\cos\beta_w\right) \\[2mm] -2\left(1 + \frac{eM_\beta}{gI_\beta}\right)\left(\frac{p_H}{\Omega}\sin\beta_w - \frac{q_H}{\Omega}\cos\beta_w\right) - \left(\frac{\dot{p}_H}{\Omega^2}\cos\beta_w + \frac{\dot{q}_H}{\Omega}\sin\beta_w\right) - \frac{\gamma}{2}\mu\left(\frac{2}{3} - \epsilon\right)\theta_0 - \frac{\gamma}{2}\mu\left(\frac{1}{2} - \frac{2}{3}\epsilon\right)\theta_0 + \frac{\mu^2}{4} \\ +\frac{\gamma}{2}\left[\left(\frac{1}{4} - \frac{\epsilon}{3}\right) + \frac{3\mu^2}{4}\left(\frac{1}{2} - \epsilon + \frac{\epsilon^2}{2}\right)\right]B_{1c} - \frac{\gamma\mu}{2}\left(\frac{1}{2} - \epsilon + \frac{\epsilon^2}{2}\right)\lambda - \frac{\gamma}{2}\left(\frac{1}{4} - \frac{\epsilon}{3}\right)\left(\frac{p_H}{\Omega}\cos\beta_w + \frac{q_H}{\Omega}\sin\beta_w\right) \end{bmatrix} \tag{2.37}
$$

where the parameter P in equation 2.36 is given by

$$
P^2 = 1 + \frac{K_\beta}{I_\beta \Omega^2} + \frac{eM_\beta}{gI_\beta} + \frac{\gamma K_1}{8}\left(1 - \frac{4}{3}\epsilon\right) \tag{2.38}
$$

Solving equation 2.34 is possible to find the TPP state $a = (a_0, a_1, b_1)^T$. Having found these values, one can easily calculate the flapping angle according to the following relationship:

$$
\beta(t) = a_0(t) - a_1(t)cos\psi - b_1(t)sin\psi \tag{2.39}
$$

By deriving it, the flapping speed and acceleration can then be evaluated.

Below is a representation of the flapping angles calculated in the TPP and then evaluated in a rotating reference system for a flight condition of 60 knots and following a collective input. It can be seen in figure 2.12 that, from the rotor trim conditions and in the absence of perturbations, the blades flap with a constant amplitude. Similarly, the flapping speed also appears to have constant amplitude and phase shift with respect to position, as in figure 2.13. In the presence of an external perturbation, such as a change in collective, the blades respond with a flapping variation that is damped in a very short time, as shown in 2.14.
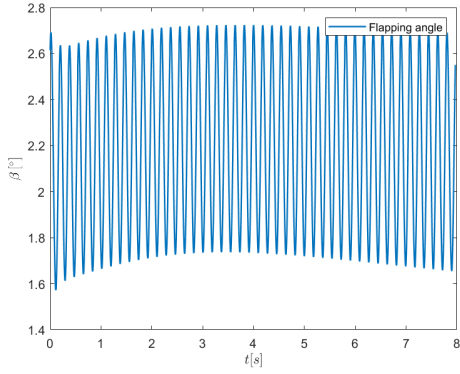
(a) Flapping angle
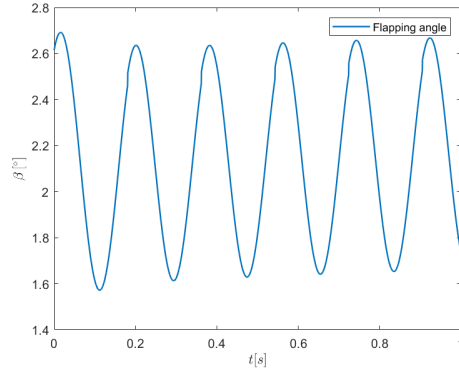
(b) Flapping angle in the first second

Figure 2.12: Flapping angle variation
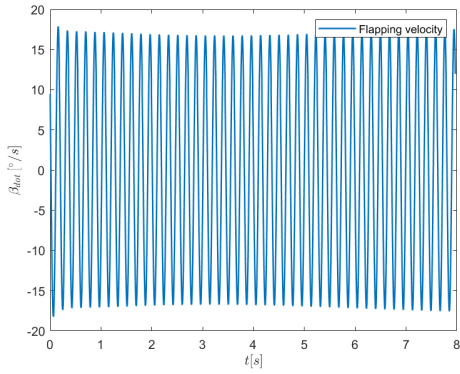
(a) Flapping velocity
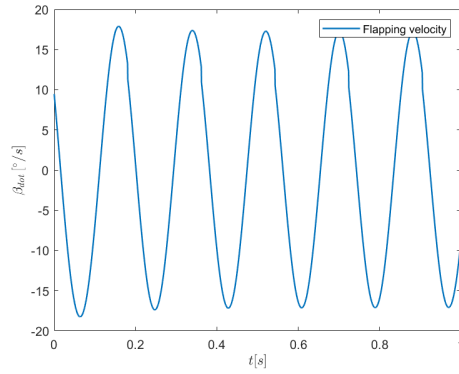
(b) Flapping velocity in the first second

Figure 2.13: Flapping velocity variation
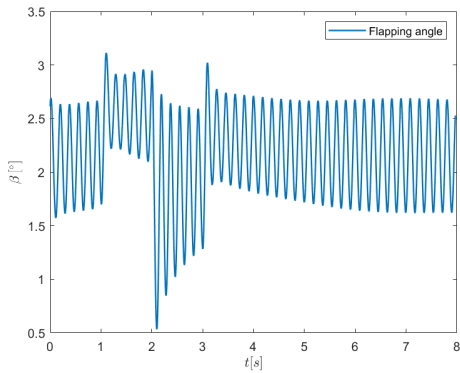
(a) Collective doublet
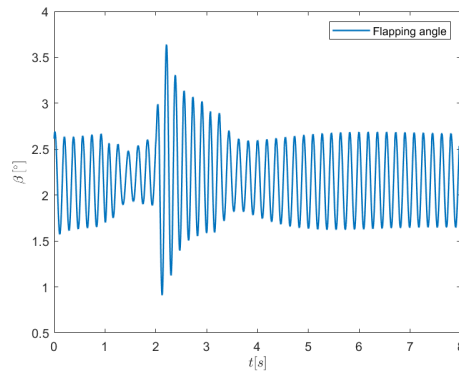
(b) Lateral doublet

Figure 2.14: Flapping angle variation after a disturbance

20

Assessed the TPP angles and rates, these are used to calculate the rotor forces and moments in the hub system. These are then evaluated according to the following expressions:

$$
\begin{aligned}
T = &\frac{N_b}{2} Cl_\alpha \rho c_m R \left(\Omega R\right)^2 \left\{ \frac{1}{2}\left(1-\epsilon^2\right)\lambda + \theta_0\left[\frac{1}{3}+\frac{\mu^2}{2}\left(1-\epsilon\right)\right] + \frac{\theta_t}{2}\left[\frac{1}{4}+\frac{\mu^2}{4}\left(1-\epsilon^2\right)\right] \right. \\
&- \frac{\mu}{2}\left(1-\epsilon^2\right)\left(B_{1c}-K_1 b_1\right) - a_0\left[\frac{1}{3}+\frac{\mu^2}{2}\left(1-\epsilon\right)\right]K_1 + a_1\left[\frac{\mu}{2}\epsilon\left(1-\epsilon\right)\right] - \frac{\dot{a}_0}{\Omega}\left(\frac{1}{3}-\frac{\epsilon}{2}\right) \\
&\left. + \frac{\dot{b}_1}{\Omega}\left(\frac{\mu}{4}\left(1-\epsilon\right)^2\right) + \frac{\mu}{4}\left(1-\epsilon^2\right)\left(\frac{p_h}{\Omega}\cos(\beta_w)+\frac{q_h}{\Omega}\sin(\beta_w)\right) - \frac{N_b M_\beta}{g}\ddot{a} \right\}
\end{aligned}
\tag{2.40}
$$

$$
\begin{aligned}
H_W = &\frac{N_b}{2}\rho Cl_\alpha c_m R\left((\Omega R)^2\right)\left\{\frac{\delta\mu}{2Cl_\alpha}\left(1-\epsilon^2\right)-\frac{1}{4}\left(\theta_0-K_1 a_0\right)\left(2\lambda\mu\left(1-\epsilon\right)\right)\right. \\
&-\mu\left(1-\epsilon\right)^2\frac{\dot{a}_0}{\Omega}-\left(\epsilon-\frac{2}{3}\right)\left(\frac{\dot{b}_1}{\Omega}-a_1\right)-\frac{2}{3}a_1+\frac{2}{3}\left(\frac{p_h}{\Omega}\cos(\beta_w)+\frac{q_h}{\Omega}\sin(\beta_w)\right)\right)-\frac{\theta_t}{4}\left[\mu\lambda\left(1-\epsilon^2\right)\right. \\
&+\frac{\dot{a}_0}{\Omega}\mu\left(\epsilon-\frac{2}{3}\right)-2\left(\frac{\epsilon}{3}-\frac{1}{4}\right)\left(\frac{\dot{b}_1}{\Omega}-a_1\right)-\frac{a_1}{2}+\frac{1}{2}\left(\frac{p_h}{\Omega}\cos(\beta_w)+\frac{q_h}{\Omega}\sin(\beta_w)\right)\right]+\frac{1}{4}\left(A_{1c}-K_1 a_1\right) \\
&\left[-\frac{b_1\mu}{4}\left(1-\epsilon^2\right)+\frac{1}{4}\mu\left(1-\epsilon\right)^2\left(\frac{\dot{a}_1}{\Omega}+b_1\right)+\frac{2}{3}a_0+\frac{\mu}{4}\left(1-\epsilon^2\right)\left(-\frac{p_h}{\Omega}\sin(\beta_w)+\frac{q_h}{\Omega}\cos(\beta_w)\right)\right] \\
&+\frac{1}{4}\left(B_{1c}-K_1 b_1\right)\left[\frac{3}{4}\mu\left(1-\epsilon\right)^2\left(\frac{\dot{b}_1}{\Omega}-a_1\right)+\left(1-\epsilon^2\right)\left(\lambda-\frac{a_1\mu}{4}\right)\right. \\
&\left.+\left(\epsilon-\frac{2}{3}\right)\frac{\dot{a}_0}{\Omega}+\frac{3\mu}{4}\left(1-\epsilon^2\right)\left(\frac{p_h}{\Omega}\cos(\beta_w)+\frac{q_h}{\Omega}\sin(\beta_w)\right)\right]+\frac{1}{4}\left(\epsilon\left(1-\epsilon\right)\left(\frac{b_1}{\Omega}-a_1\right)4\lambda\right. \\
&-\left(1-\epsilon^2\right)\left(2\lambda\left(\frac{\dot{b}_1}{\Omega}-a_1\right)-a_1\lambda\right)-\left(\frac{2}{3}-\epsilon\right)\left(a_1\frac{\dot{a}_0}{\Omega}+a_0\left(\frac{\dot{a}_1}{\Omega}+b_1\right)\right) \\
&-\frac{2a_0}{3}\left(-\frac{p_h}{\Omega}\sin(\beta_w)+\frac{q_h}{\Omega}\cos(\beta_w)\right)-\left(2\left(1-\epsilon^2\right)\lambda-4\left(\frac{1}{3}-\frac{\epsilon}{2}\right)\frac{\dot{a}_0}{\Omega}\right)\left(\frac{p_h}{\Omega}\cos(\beta_w)+\frac{q_h}{\Omega}\sin(\beta_w)\right) \\
&+4\frac{\dot{a}_0}{\Omega}\left(\frac{b_1}{\Omega}-a_1\right)\left(\frac{1}{3}-\epsilon+\epsilon^2\right)\right)+\frac{\mu}{4}\left(\epsilon\left(1-\epsilon\right)\left(a_1\left(\frac{\dot{b}_1}{\Omega}-a_1\right)+b_1\left(\frac{\dot{a}_1}{\Omega}+b_1\right)\right)\right. \\
&+\frac{1}{4}\left((1-\epsilon)^2\right)\left(b_1\left(\frac{\dot{a}_1}{\Omega}+b_1\right)+a_1\left(\frac{\dot{b}_1}{\Omega}-a_1\right)\right) \\
&-\frac{1}{2}\left(1-\epsilon^2\right)\left(a_1\left(\frac{\dot{b}_1}{\Omega}-a_1\right)+b_1\left(\frac{\dot{a}_1}{\Omega}+b_1\right)-2a_0^2-\frac{b_1^2}{2}-\frac{3}{2}a_1^2\right) \\
&\left.-\frac{a_1}{4}\left(1-\epsilon^2\right)\left(\frac{p_h}{\Omega}\cos(\beta_w)+\frac{q_h}{\Omega}\sin(\beta_w)\right)-\frac{b_1}{4}\left(1-\epsilon^2\right)\left(-\frac{p_h}{\Omega}\sin(\beta_w)+\frac{q_h}{\Omega}\cos(\beta_w)\right)\right\}
\end{aligned}
\tag{2.41}
$$

$$
\begin{aligned}
Y_W = {} & \frac{N_b}{2}\rho C l_\alpha c_m R\left((\Omega R)^2\right)\Bigg\{-\frac{1}{4}(\theta_0 - K_1 a_0)\left(\left(\epsilon - \frac{2}{3}\right)\left(\frac{\dot{a}_1}{\Omega} + b_1\right) - \frac{2}{3}b_1 + 3a_0(1-\epsilon^2)\mu - 2b_1(1-\epsilon)\mu^2\right.\\
& -\frac{2}{3}\left(-\frac{p_h}{\Omega}\sin(\beta_w) + \frac{q_h}{\Omega}\cos(\beta_w)\right)\Bigg) - \frac{\theta_T}{4}\left(\left(\frac{2\epsilon}{3} - \frac{1}{2}\right)\left(\frac{\dot{a}_1}{\Omega} + b_1\right) - \frac{b_1}{2} + 2a_0\mu - b_1(1-\epsilon^2)\mu^2\right.\\
& -\frac{1}{2}\left(-\frac{p_h}{\Omega}\sin(\beta_w) + \frac{q_h}{\Omega}\cos(\beta_w)\right)\Bigg) - \frac{1}{4}(A_{1c} - K_1 a_1)\\
& \left(\left(\epsilon - \frac{2}{3}\right)\frac{\dot{a}_0}{\Omega} + \lambda(1-\epsilon^2) + \mu\left(\frac{5a_1}{4}(1-\epsilon^2) + \frac{1}{4}(1-\epsilon)^2\left(\frac{\dot{b}_1}{\Omega} - a_1\right)\right) + \frac{\mu}{4}(1-\epsilon^2)\right.\\
& \left(\frac{p_h}{\Omega}\cos(\beta_w) + \frac{q_h}{\Omega}\sin(\beta_w)\right)\Bigg) - \frac{1}{4}(B_{1c} - K_1 b_1)\left(-\frac{2}{3}a_0 + \mu\left(\frac{7}{4}b_1(1-\epsilon^2) + \frac{1}{4}(1-\epsilon)^2\left(\frac{\dot{a}_1}{\Omega} + b_1\right)\right.\right.\\
& \left.\left. +\frac{1}{4}\left(-\frac{p_h}{\Omega}\sin(\beta_w) + \frac{q_h}{\Omega}\cos(\beta_w)\right)\right) - \mu^2\left(2a_0(1-\epsilon)\right)\right)\\
& -\frac{1}{4}\left(4\left(\frac{1}{3} - \epsilon + \epsilon^2\right)\frac{\dot{a}_0}{\Omega}\left(\frac{\dot{a}_1}{\Omega} + b_1\right) - 2\lambda(1-\epsilon)^2\left(\frac{\dot{a}_1}{\Omega} + b_1\right) + \frac{2a_0}{3}\left(\frac{p_h}{\Omega}\cos(\beta_w) + \frac{q_h}{\Omega}\sin(\beta_w)\right)\right.\\
& +2a_0\left(\frac{1}{3} - \frac{\epsilon}{2}\right)\left(\frac{\dot{b}_1}{\Omega} - a_1\right) - 2b_1\left(\frac{\lambda}{2}(1-\epsilon^2) - \frac{\dot{a}_0}{\Omega}\left(\frac{1}{3} - \frac{\epsilon}{2}\right)\right) + \left(4\left(\frac{1}{3} - \frac{\epsilon}{2}\right)\frac{\dot{a}_0}{\Omega} - 2(1-\epsilon^2)\lambda\right)\\
& \left(-\frac{p_h}{\Omega}\sin(\beta_w) + \frac{q_h}{\Omega}\cos(\beta_w)\right)\Bigg) - \frac{\mu}{4}\left(6a_0\lambda(1-\epsilon) - \frac{a_1 b_1}{2}(1-\epsilon^2) - 3(1-\epsilon^2)a_0\frac{\dot{a}_1}{\Omega}\right.\\
& -\frac{7}{4}(1-\epsilon^2)a_1\left(\frac{\dot{a}_1}{\Omega} + b_1\right) - \frac{5}{4}b_1(1-\epsilon^2)\\
& \left(\frac{p_h}{\Omega}\cos(\beta_w) - \frac{q_h}{\Omega}\sin(\beta_w)\right) - \frac{7}{4}a_1(1-\epsilon^2)\left(-\frac{p_h}{\Omega}\sin(\beta_w) + \frac{q_h}{\Omega}\cos(\beta_w)\right)\\
& \left.-\frac{5}{4}(1-\epsilon)^2 b_1\left(\frac{\dot{b}_1}{\Omega} - a_1\right)\right) - \mu^2\left(a_0 a_1(1-\epsilon)\right)\Bigg\}
\end{aligned}
$$

(2.42)

$$
\begin{aligned}
L_W = {} & \frac{N_b}{2}\left[K_\beta b_1 - \frac{eM_\beta}{g}\left(\ddot{b}_1 - 2\dot{a}_1\Omega - b_1\Omega^2\right)\right] - \frac{N_b}{2}I_b\Omega^2\gamma\epsilon\Bigg\{\frac{\mu}{2}(1-\epsilon^2)\left(\theta_0 - K_1 a_0\right) - \left(\frac{1}{6} + \frac{3}{8}\mu^2(1-\epsilon)\right)\\
& \left(B_{1c} - K_1 b_1\right) + \frac{\mu}{3}\theta_T + \frac{\mu}{2}(1-\epsilon)\lambda + \frac{\mu^2}{8}(1-\epsilon)a_1 - \frac{\mu}{4}(1-\epsilon)^2\frac{\dot{a}_0}{\Omega} + \left(\frac{1}{6} - \frac{\epsilon}{4}\right)\\
& \left(\frac{\dot{b}_1}{\Omega} - a_1\right) + \frac{1}{6}\left(\frac{p_h}{\Omega}\cos(\beta_w) + \frac{q_h}{\Omega}\sin(\beta_w)\right)\Bigg\}
\end{aligned}
$$

(2.43)

$$
\begin{aligned}
M_W = {} & \frac{N_b}{2}\left(K_\beta a_1 - \frac{eM_\beta}{g}\left(\ddot{a} + 2\dot{b}_1\Omega - a_1\Omega^2\right)\right) - \frac{N_b}{2}I_\beta\Omega^2\gamma\epsilon\Bigg\{-\left[\frac{1}{6} + \frac{\mu^2}{8}(1-\epsilon)\right]\left(A_{1c} - K_1 a_1\right)\\
& -\frac{\mu}{4}(1-\epsilon^2)a_0 + \frac{\mu^2}{8}(1-\epsilon)b_1 + \left(\frac{1}{6} - \frac{\epsilon}{4}\right)\left(\frac{\dot{a}_1}{\Omega} + b_1\right) + \frac{1}{6}\left(-\frac{p_h}{\Omega}\sin(\beta_w) + \frac{q_h}{\Omega}\cos(\beta_w)\right)\Bigg\}
\end{aligned}
$$

(2.44)

$$Q_W = \frac{N_b}{2}\rho Cl_\alpha c_m R^2 (\Omega R)^2 \left\{ \frac{\delta}{4Cl_\alpha}\left(1 + (1-\epsilon^2)\mu^2\right) - \left(\theta_0 - K_1 a_0\right) \right.$$

$$\left(\frac{\lambda}{3} + \left(\frac{\epsilon}{3} - \frac{1}{4}\right)\frac{\dot{a}_0}{\Omega} + \frac{\mu}{6}\frac{\dot{b}_1}{\Omega} - \frac{\mu\epsilon}{4}\left(\frac{\dot{b}_1}{\Omega} - a_1\right) + \frac{\mu}{6}\left(\frac{p_h}{\Omega}\cos(\beta_w) + \frac{q_h}{\Omega}\sin(\beta_w)\right)\right)$$

$$+ \left(A_{1c} - K_1 a_1\right)\left(\left(\frac{1}{8} - \frac{\epsilon}{6}\right)\left(\frac{\dot{a}_1}{\Omega} + b_1\right) - \frac{\mu}{6}a_0 + \frac{b_1}{16}(1 - \epsilon^2)\mu^2\right.$$

$$\left.+ \frac{1}{8}\left(-\frac{p_h}{\Omega}\sin(\beta_w) + \frac{q_h}{\Omega}\cos(\beta_w)\right)\right) + \left(B_{1c} - K_1 b_1\right)\left(\left(\frac{1}{8} - \frac{\epsilon}{6}\right)\left(\frac{\dot{b}_1}{\Omega} - a_1\right)\right.$$

$$\left.+ \left(\frac{\epsilon}{4} - \frac{1}{6}\right)\mu\frac{\dot{a}_0}{\Omega} + \frac{1}{2}(1 - \epsilon^2)\left(\frac{\mu\lambda}{2} + \frac{a_1}{8}\mu^2\right) + \frac{1}{8}\left(\frac{p_h}{\Omega}\cos(\beta_w) + \frac{q_h}{\Omega}\sin(\beta_w)\right)\right)$$

$$- \theta_T\left(\frac{\lambda}{4} + \left(\frac{\epsilon}{4} - \frac{1}{5}\right)\frac{\dot{a}_0}{\Omega} + \frac{\mu}{8}\frac{\dot{b}_1}{\Omega} - \frac{\epsilon\mu}{6}\left(\frac{\dot{b}_1}{\Omega} - a_1\right)\right) - \frac{1}{2}(1 - \epsilon^2)\left(\lambda^2 + \lambda\mu a_1 + 2\lambda\epsilon\frac{\dot{a}_0}{\Omega}\right.$$

$$\left.+ \mu\epsilon\left(a_1\frac{\dot{a}_0}{\Omega} + a_0\left(\frac{\dot{a}_1}{\Omega} + b_1\right)\right) + \mu^2\left(\frac{a_0^2}{2} + \frac{3}{8}a_1^2 + \frac{1}{8}b_1^2\right)\right) + \frac{\mu}{3}\left(a_1\frac{\dot{a}_0}{\Omega} + a_0\left(\frac{\dot{a}_1}{\Omega} + b_1\right)\right) + \frac{2}{3}\lambda\frac{\dot{a}_0}{\Omega}$$

$$- \left(-\frac{\mu}{3}a_0 + \left(\frac{1}{4} - \frac{\epsilon}{3}\right)\left(\frac{\dot{a}_1}{\Omega} + b_1\right)\right)\left(-\frac{p_h}{\Omega}\sin(\beta_w) + \frac{q_h}{\Omega}\cos(\beta_w)\right) - \left(\frac{1}{4} - \frac{\epsilon}{3}\right)\left(\frac{\dot{b}_1}{\Omega} - a_1\right)$$

$$\left(\frac{p_h}{\Omega}\sin(\beta_w) + \frac{q_h}{\Omega}\cos(\beta_w)\right) - \frac{1}{8}\left(-\frac{p_h}{\Omega}\sin(\beta_w) + \frac{q_h}{\Omega}\cos(\beta_w)\right)^2$$

$$\left. - \frac{1}{8}\left(\frac{p_h}{\Omega}\sin(\beta_w) + \frac{q_h}{\Omega}\cos(\beta_w)\right)^2 - \left(\frac{1}{4} - \frac{2\epsilon}{3} + \frac{\epsilon^2}{2}\right)\left(\left(\frac{\dot{a}_0}{\Omega}\right)^2 + \frac{1}{2}\left(\left(\frac{\dot{a}_1}{\Omega} + b_1\right)^2 + \left(\frac{\dot{b}_1}{\Omega} - a_1\right)^2\right)\right)\right\}$$

(2.45)

The equations reported must then be transformed in the body axes frame thanks to the transformation 2.3.

2.3.7   Bell 412 main rotor

The main rotor of the Bell 412 is a four-bladed rotor with a clockwise direction of rotation. The blades have a linear twist and a variable chord. Although the Bell 412's blade consists of four separate airfoils, the model implemented considers a constant profile of the Boeing VR-7 type with a constant chord. The aerodynamic coefficients are evaluated as variation of Mach and angle of incidence, as can be seen in the pictures 2.15. In particular, the incidence varies between $[-44° : -0.5 : 44°]$, while the Mach number is evaluated between $[0.34 : 0.05 : 0.84]$.

(a) Lift coefficient   (b) Drag coefficient
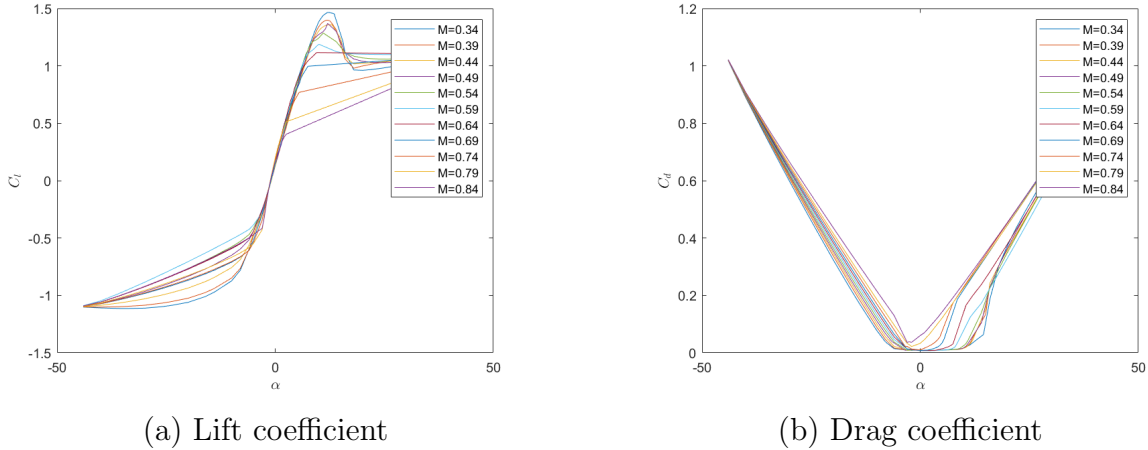
Figure 2.15: Boeing VR-7 airfoil aerodynamic coefficient

Considering only the linear section of the lift coefficient curve, thus not considering aerodynamic stall, it is possible to calculate the C_{L_α} derivative. Its variation with respect to the Mach is shown in the following graph:
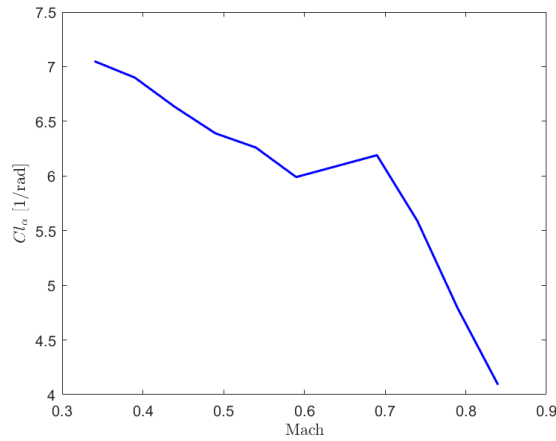
Figure 2.16: C_{L_α} variation with respect to the Mach

With regard to the drag coefficient, both Chen and Padfield described it as:

$$C_d = C_{d,0} + C_{d,1} C_T^2 \tag{2.46}$$

By using the thrust coefficient and interpolating drag coefficient data, it is possible to obtain values for each flight condition.

Since the rotor of the Bell 412 is a semi-rigid rotor, the mathematical model used to calculate

the flapping dynamics is that of the Centre-Spring Equivalent Rotor. The blade stiffness is approximated by a spring and no offset from the shaft position is considered for the development of the flapping dynamics. Using this formulation, the rotor characteristics, as given in [9], are considered as follows:

Parameter	Value
K_β	75057 [Nm/rad]
λ_β	1.03 [Hz]
ϵ	0 [m]
M_β	262.8898 [kg m]
I_β	1069.7 [kg m^2]

Table 2.2: Main rotor parameter

2.4   Tail rotor

The Bell 412 tail rotor is a clockwise rotor made by two blades mounted on the right side of the tail, with the attachment point above the plane of the main rotor disc.
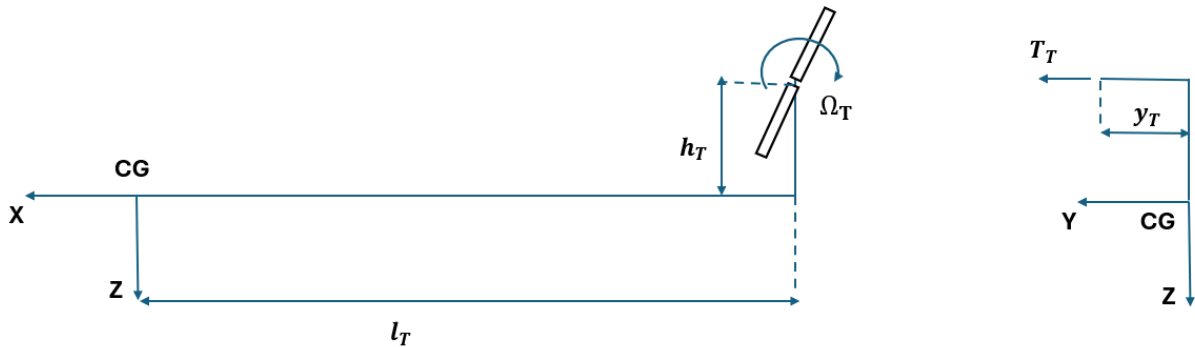
Figure 2.17: Tail rotor configuration

The main purpose of the tail rotor is to generate the lateral thrust required to create a moment to counterbalance the torque of the main rotor. The modelling of this component is based on the Padfield model [6]. In this case, two models were followed. The first does not take flapping into account, while the second considers this dynamic. As reported, the lateral thrust of the tail is given by the following expression:

$$T_{TR} = \frac{1}{2}\sigma_T Cl_\alpha \rho \left(\Omega_T R_T\right)^2 \left(\pi R_T\right)^2 C_T F_T \tag{2.47}$$

where the thrust coefficient is given by

$$C_{T_T} = \frac{\theta_{0T}^*}{3}\left(1 + \frac{3}{2}\mu_t^2\right)\left(\frac{\mu_{zt} - \lambda_0 T}{2}\right) + \frac{\mu_t}{2}K_{1T}\beta_{1sT} \tag{2.48}$$

and F_T is the tail blockage factor. This considers the flow blockage caused by the vertical fin and has a reducing effect on the overall thrust. It is defined as:

$$F_T = 1 - \frac{3S_{fin}}{4\pi R_T^2} \tag{2.49}$$

It can be seen that this effect depends directly on the fin surface to tail rotor surface ratio, and growing the rotor radius has a benefical effect on the thrust generation.

The tail rotor velocities can be evaluated as:

$$\mu_t = \frac{\sqrt{u^2 + (w - k_{\lambda_T}\lambda_0 + q(l_T + x_{cg})^2}}{\Omega_T R_T} \tag{2.50}$$

$$\mu_{zt} = \frac{v - r(l_T + x_{cg}) + ph_T}{\Omega_T R_T} \tag{2.51}$$

where $k_{\lambda T}$ is the main rotor interference factor and it must be tuned for every flight condition to take into account the main rotor downwash.

To evaluate the thrust, is first necessary to calculate the effective collective given by the pedal input. Considering the flapping dynamics, this is equal to:

$$\theta_{0T}^* = \frac{\theta_{0T} + k_3 \left(\frac{\gamma}{8\lambda_\beta^2}\right)_T \frac{4}{3}(\mu_z - \lambda_{0T})}{1 - k_3 \left(\frac{\gamma}{8\lambda_\beta^2}\right)_T (1 + \mu_T^2)} \tag{2.52}$$

If no flapping dynamic is taken into account, then the pedal input is equal to the θ_{0T} imposed. The lateral and longitudinal flapping angles are then evaluated with the expressions:

$$\beta_{1sT} = \frac{\frac{8}{3}\mu_t\left[k_3 + \left(\frac{\gamma}{16\lambda_\beta^2}\right)_T\right]\theta_{0T} + 2\mu_t\left[k_3 + \left(\frac{\gamma}{16\lambda_\beta^2}\right)_T\left(\frac{4}{3}\right)^2\right](\mu_{zt} - \lambda_{0T})}{\left[1 + k_3\left(\frac{\gamma}{16\lambda_\beta^2}\right)_T\left(\frac{4}{3}\mu_T\right)^2 + k_3^2\left(1 + 2\mu_T^2\right)\right]} \tag{2.53}$$

$$\beta_{1cT} = -\frac{8}{3}\mu_T\theta_{0T} - 2\mu_t(\mu_{zt} - \lambda_{0T}) - k_3\left(1 + 2\mu_t^2\right)\beta_{1sT} \tag{2.54}$$

To compute the tail inflow, an iterative procedure based on the Ralphson-Newton metodology

is applied on the equation:

$$\lambda_{0T} = \frac{C_{T_T}}{2\sqrt{\mu_t^2 + (\mu_{zt} - \lambda_{0T})^2}} \tag{2.55}$$

In contrast to the main rotor, calculation of the tail rotor inflow does not use the value calculated at the previous temporal step as initial condition, but the hover value is always taken as initial value of the algorithm. In fact, due to the higher rotation speed of the blades, the feedback of this value would have required integration step too small, deteriorating the computational performance of the model.

For the torque calculation the following expression is used:

$$Q_T = \frac{1}{2}\rho\left(\Omega_T R_T\right)^2\left(\pi R_T^2\right)R_T Cl_\alpha \sigma_T \left[\left(\mu_{zt} - \lambda_{0T}\right)\left(\frac{2C_{T_T}}{Cl_\alpha \sigma_T}\right) + \frac{\delta_T}{4Cl_\alpha}\left(1 + 3\mu_T^2\right)\right] \tag{2.56}$$

where $\delta_T = \delta_{0T} + \delta_{2T}C_{T_T}^2$ is the blade drag. The δ_{iT} coefficients are taken constant, so drag results only a function of the thrust.

With the model presented, it is possible to calculate the forces and moments as follows:

$$X_T \sim T_T \beta_{1c} \tag{2.57}$$

$$Y_T = T_T \tag{2.58}$$

$$Z_T \sim -T_T \beta_{1sT} \tag{2.59}$$

$$L_T \sim h_T Y_T \tag{2.60}$$

$$M_T \sim (l_T + x_{cg})Z_T - Q_T \tag{2.61}$$

$$N_T = -(l_T + x_{cg})Y_T \tag{2.62}$$

In case of no flapping dynamic effects, the X_T and Z_T forces are equal to zero and the moment M_T is just opposite to the rotor torque. Equations used for the model that do not consider tha flapping dynamic are the same as those proposed in this paragraph, but with zero flapping angles.

Differences between the flapping tail and the no flapping tail

The differences between the model with and without flapping are now shown. The case of the isolated rotor in a speed condition of 60 knots is considered, an intermediate case between those used for validation as reported in chapter 3. Both the stationary case, figure 2.18, and a case where a pedal doublet input is provided, figure 2.19, are shown.
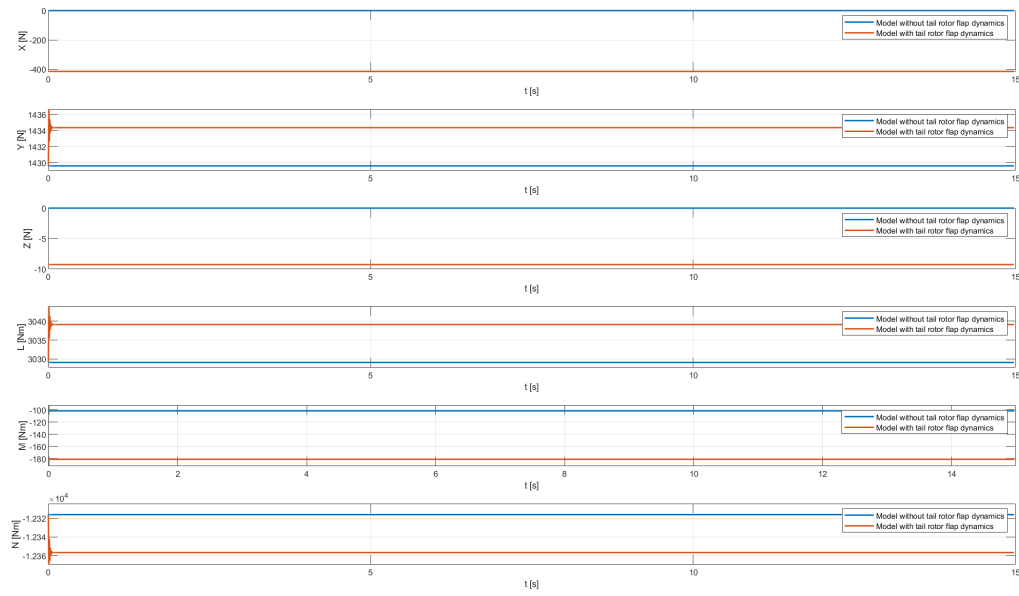
Figure 2.18: Isolated tail rotor in a steady state
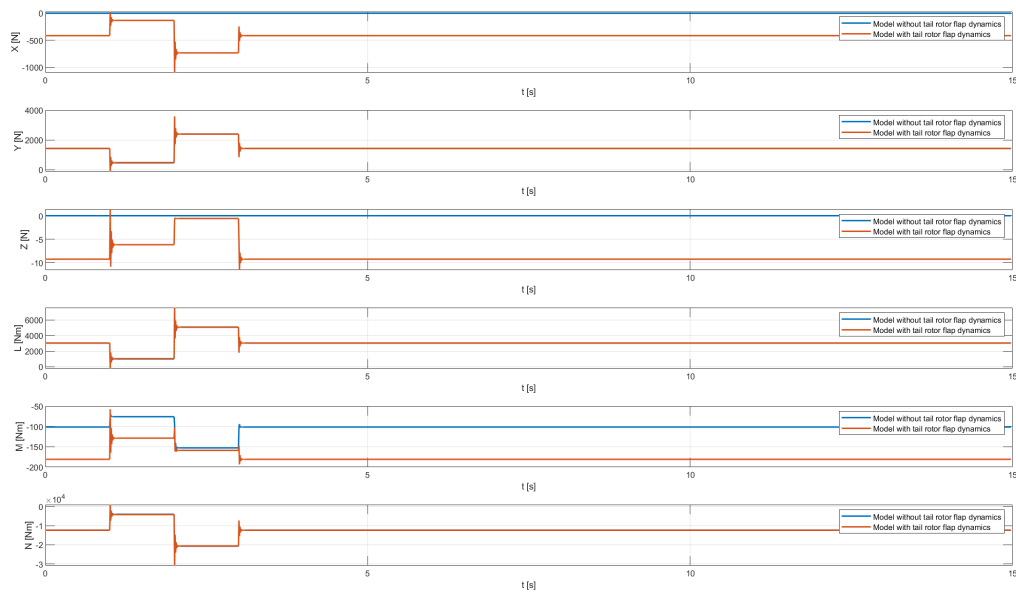
Figure 2.19: Isolated tail rotor perturbed by a doublet input

Observing the behavior of the isolated rotor, as in figure 2.18-2.19, the following differences

28

can be noted. First, with the former model, there is a force component along both the x-axis and the z-axis, due to the projection of the lateral force along the longitudinal and lateral flapping angles. Additionally, flapping dynamics influences also the lateral force and the moments generated by the tail rotor. In particular, the side force and the roll moment results slightly higher when the flapping is taken into account, as well as the pitch and yaw moment which are higher. This is less evident in the presence of a doublet input. In fact, it can be seen that in this case there is only a large difference in the longitudinal forces and the pitching moment, while the other components are almost identical. For the former, the difference is only due to the fact that it is zero in the first model.

The model without flapping dynamics was used for the development of the simulator. This choice was made because the model presented by Padfield has a rather high degree of approximation in the calculation of the flapping dynamics, and during the validation of the results it was found that the quality of the simulation deteriorated when the flapping dynamics were taken into account. In figures 2.20,2.21 are reported the comparison with FlightLab simulations. Considering the flapping dynamics involves a significant difference to the Flight-Lab model in terms of longitudinal force, vertical force and pitch moment.Therefore, if this dynamic were to be taken into account, it would have to be described by a more accurate model.
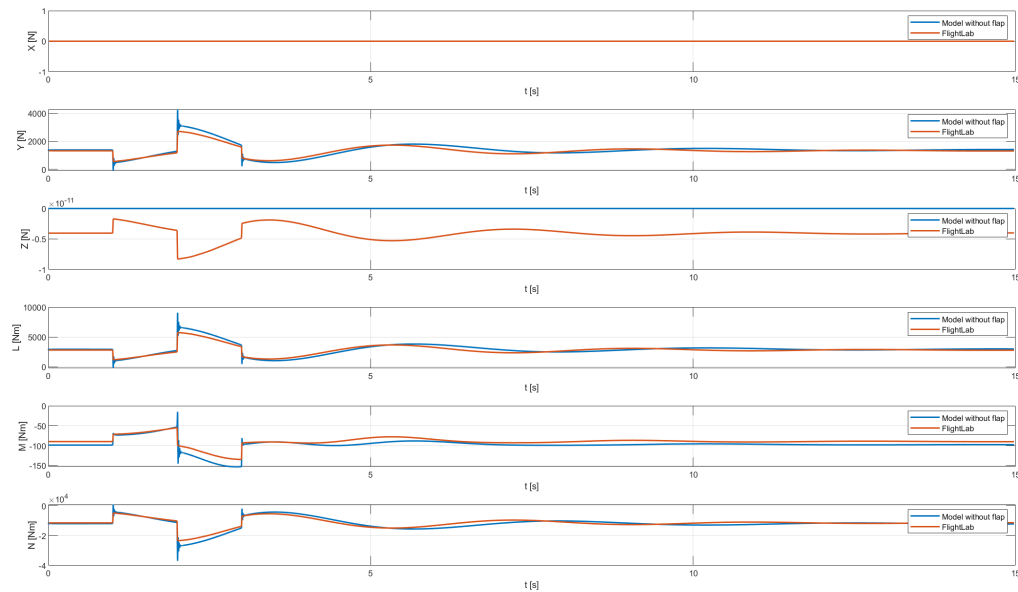
Figure 2.20: Comparison between the model without flapping dynamic and FlightLab
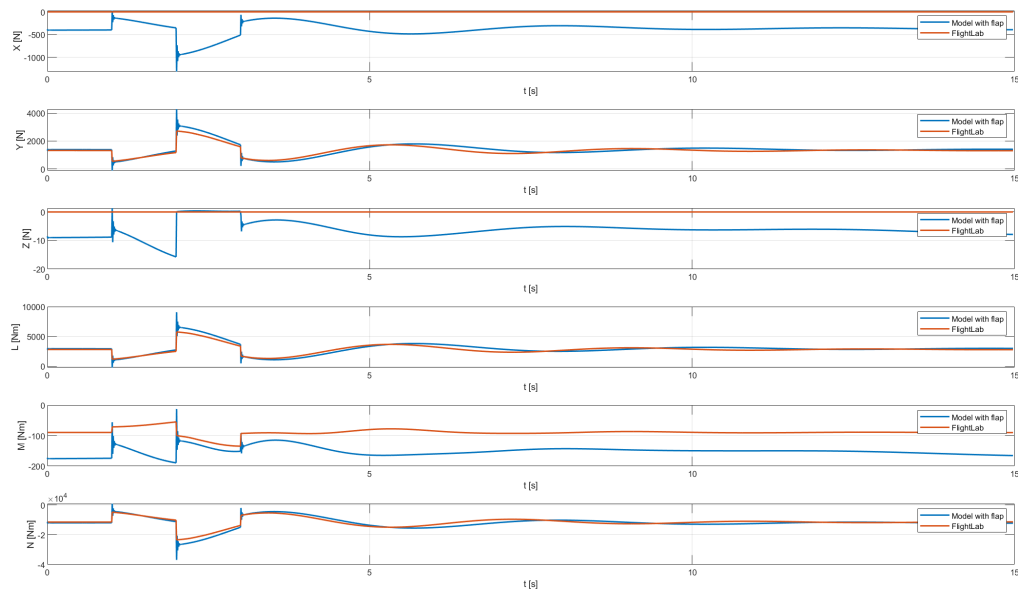
Figure 2.21: Comparison between the model with flapping dynamic and FlightLab
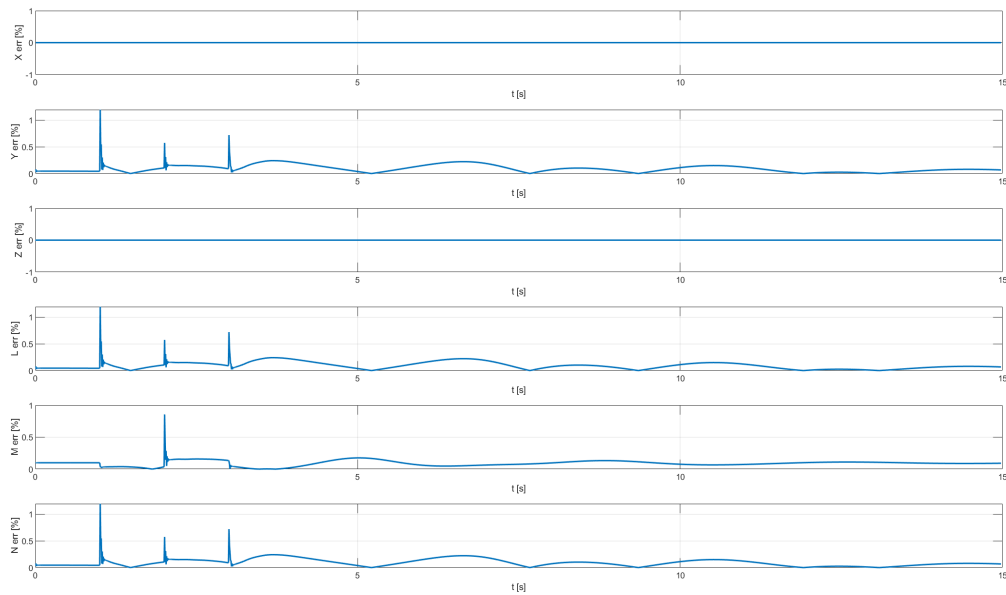
Figure 2.22: Tail rotor relative error between the model choosen and FlightLab

Furthermore, looking at the figure 2.22, the relative error variation during the simulation

can be observed. In steady-state, there is an error of less than 5% in all cases, except for the pitching moment where it is 9.9%. Greater fluctuations occur as soon as the pedal amplitude is changed, as a result of the inflow calculation algorithm used, but then the error converge to the steady-state.

2.5   Stabilizer

The main purpose of the stabilizer is to generate a vertical force to balance the pitch moment of the rotor and increase the stability in forward flight.
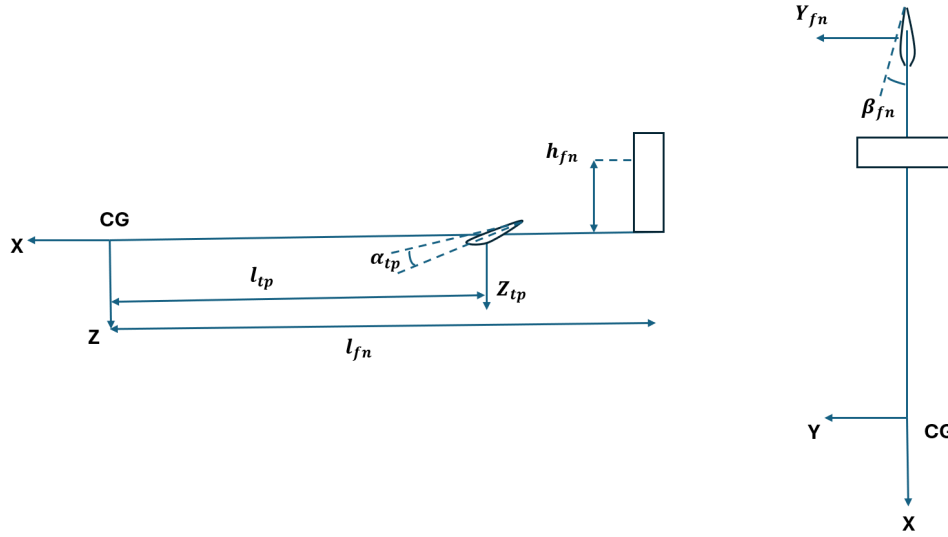
Figure 2.23: Empennages general configuration

Regarding the matemathical model, the explanation proposed by Padfield [6] has been followed. Looking at the figure 2.23, the effective incidence on the tail is given by:

$$\alpha_{tp} = \alpha_{0_{tp}} + tan^{-1}\left[\frac{\left(w + (l_{tp} + x_{cg}) - k_{\lambda_{tp}}\Omega R\lambda_0\right)^2}{u}\right], \quad u \geq 0 \tag{2.63}$$

$$(\alpha_{tp})_{reverse} = (\alpha_{tp})_{forward} + \pi, \quad u < 0 \tag{2.64}$$

The normalized total velocity is calculated as:

$$\mu_{tp} = \frac{\sqrt{u^2 + \left(w + q\left(l_{tp} + x_{cg}\right) - k_{\lambda_{tp}}\Omega R\lambda_0\right)^2}}{\Omega R} \tag{2.65}$$

The parameter $k_{\lambda_{tp}}$ represents the main rotor downwash. It must be noted that not in every

flight conditions the tail plane is affected by the downwash. As can be seen in figure 2.24, this effect only occurs when the wake angle satisfies the following relation:

$$tan^{-1}\left(\frac{l_{tp}-R}{h_r-h_{tp}}\right) \leq \chi \leq tan^{-1}\left(\frac{l_{tp}}{h_r-h_{tp}}\right) \tag{2.66}$$

where $\chi = tan^{-1}\left(\frac{\mu}{\lambda_0-\mu_z}\right)$.
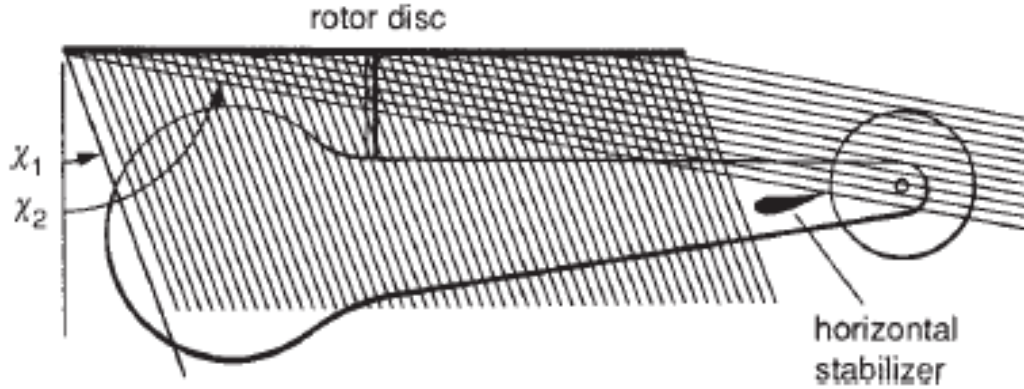
Figure 2.24: Effect of the wake on the stabilizer [6]

The horizontal stabilizer generates as a primary effect a vertical force and a pitching moment, those given by the following expressions:

$$Z_{tp} = \frac{1}{2}\rho V_{tp}^2 S_{tp} C_{z_{tp}}\left(\alpha\right) \tag{2.67}$$

$$M_{tp} = \left(l_{tp} + x_{cg}\right)Z_{tp} \tag{2.68}$$

Forces and moments are evaluated in wind axis and then transformed in body axis using equation 2.2.

Bell 412 stabilizer

The Bell 412's stabiliser features a ClarkY profile mounted inversely on the tailplane with no swirling. The left and right sides have different initial settings, specifically -6.2° for the left stabiliser and -3.6° for the right. Aerodynamic coefficients are interpolated from look up tables obtained by varying the incidence and shown in figure 2.25.
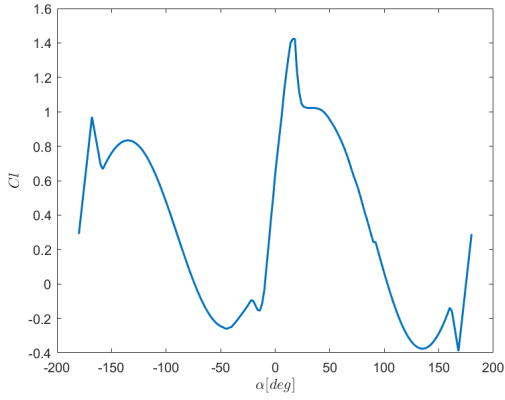
(a) Lift coefficient
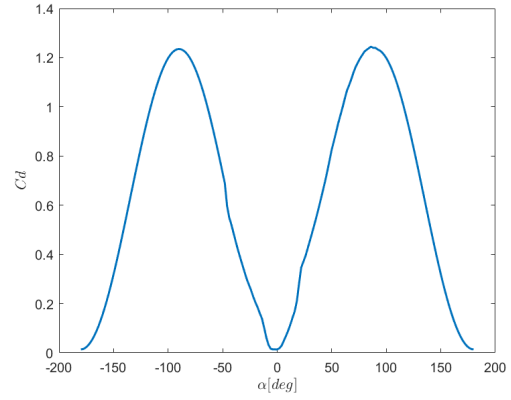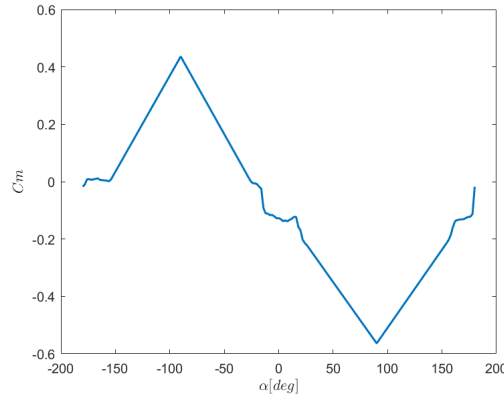
(b) Drag coefficient

(c) Pitch coefficient

Figure 2.25: Stabilizer aerodynamic coefficient

2.6 Vertical Fin

The model followed, as for the horizontal stailizer, is the Padfield one [6]. Referring to the figure 2.23, the sideslip on the fin is computed as:

$$\beta_{fn} = sin^{-1} \left[\frac{v - r \left(l_{fn} + x_{cg} \right) + h_{fn} p}{\mu_{fn} \Omega R} \right] \tag{2.69}$$

where the adimensional total velocity is calculated with the equation:

$$\mu_{fn} = \left[\frac{\sqrt{\left(v - r \left(l_{fn} + x_{cg} \right) \right)^2 + u^2}}{\Omega R} \right] \tag{2.70}$$

The vertical fin is primarily responsible of generating a lateral force, as well as a rolling and a yawing moment. They can be calculated in the following way:

$$Y_{fn} = \frac{1}{2}\rho V_{fn}^2 S_{fn} C_{y_{fn}}(\beta_{fn}) \tag{2.71}$$

$$N_{fn} = -\left(l_{fn} + x_{cg}\right) Y_{fn} \tag{2.72}$$

$$L_{fn} = \left(h_{fn} - y_{cg}\right) Y_{fn} \tag{2.73}$$

these are then transformed into body axes with the equation 2.2.

Bell412 vertical fin

The Bell412's vertical fin is made by a simmetric airfoil of the type NACA0021. Aerodynamic coefficient are evaluated interpolating the look-up tables with respect to the sideslip variation and are reported in figure 2.26.

(a) Lift coefficient   (b) Drag coefficient
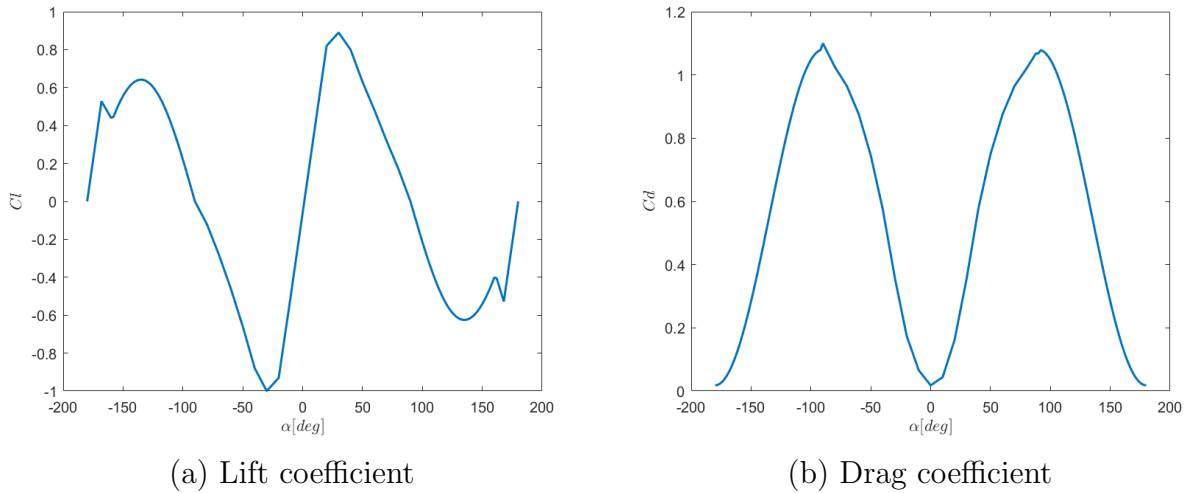
Figure 2.26: Vertical fin aerodynamic coefficient

2.7   Fuselage

As suggested by Padfield [6], to properly model the fuselage is necessary to compute total airspeed and incidence angle, defined as:

$$V_f = \sqrt{u^2 + v^2 + w^2}, \quad \alpha_f = tan^{-1}\left(\frac{w}{u}\right), \quad \lambda_0 < 0 \tag{2.74}$$

$$V_f = \sqrt{u^2 + v^2 + w_\lambda^2}, \quad \alpha_f = tan^{-1}\left(\frac{w_\lambda}{u}\right), \quad \lambda_0 > 0 \tag{2.75}$$

where

$$w_\lambda = w - k_{\lambda_f} \Omega R \lambda_0 \tag{2.76}$$

The parameter k_{λ_f} takes into account the main rotor downwash and also in this case a tuning is required for every flight condition. The sideslip is given by:

$$\beta_F = sin^{-1} \left(\frac{v}{V_f} \right) \tag{2.77}$$

The aerodynamic loadings are evaluated in the following way:

$$X_f = \frac{1}{2} \rho V_f^2 S_p C_{xf} \left(\alpha_f, \beta_f \right) \tag{2.78}$$

$$Y_f = \frac{1}{2} \rho V_f^2 S_s C_{yf} \left(\alpha_f, \beta_f \right) \tag{2.79}$$

$$Z_f = \frac{1}{2} \rho V_f^2 S_p C_{zf} \left(\alpha_f, \beta_f \right) \tag{2.80}$$

$$L_f = \frac{1}{2} \rho V_f^2 S_s l_f C_{lf} \left(\alpha_f, \beta_f \right) \tag{2.81}$$

$$M_f = \frac{1}{2} \rho V_f^2 S_p l_f C_{mf} \left(\alpha_f, \beta_f \right) \tag{2.82}$$

$$N_f = \frac{1}{2} \rho V_f^2 S_s l_f C_{nf} \left(\alpha_f, \beta_f \right) \tag{2.83}$$

Also in this case, is required to transform forces from a wind reference system to a body frame.

Bell412 fuselage

Knowing the incidence and the sideslip, the aerodynamic coefficients are calculated interpolating the look up tables given for every flight conditions. These, take into account ranges between $[-180° : 180°]$ for the sidelispe and $[-90° : 90°]$ for the angle of incidence.
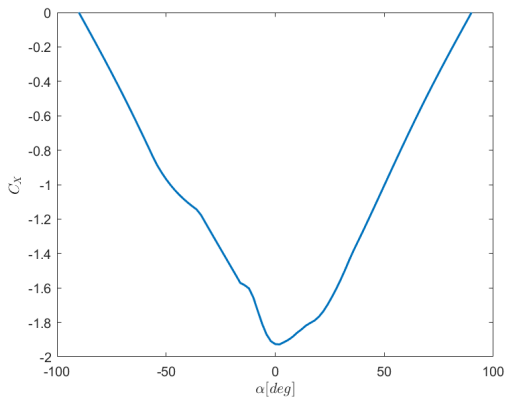
(a) X force coefficient
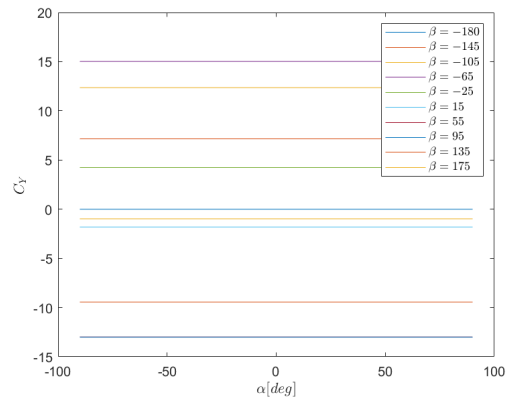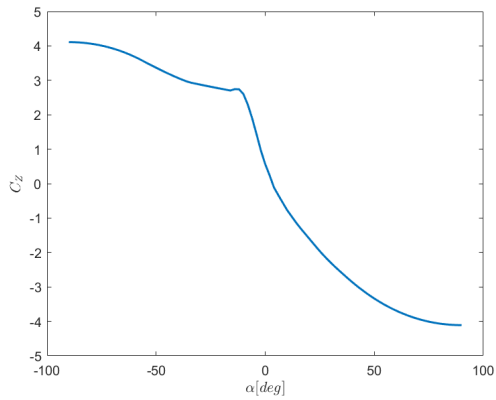
(b) Y force coefficient

(c) Z force coefficient
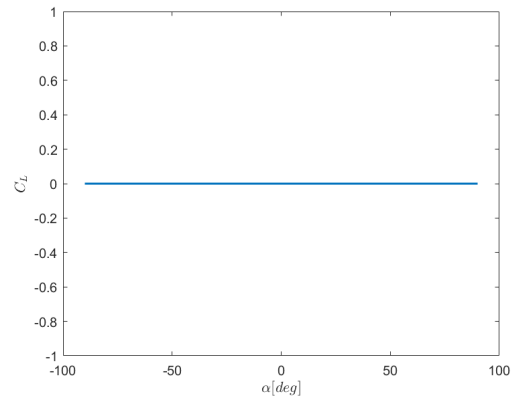
(d) L moment coefficient
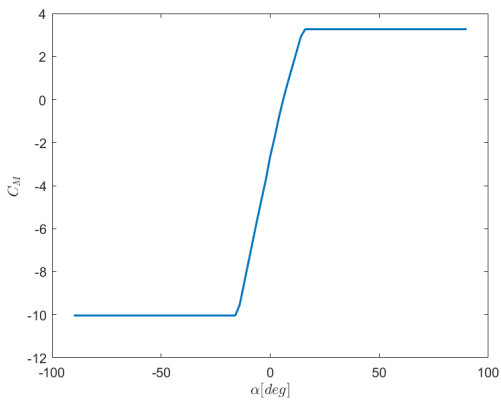
(e) M moment coefficient
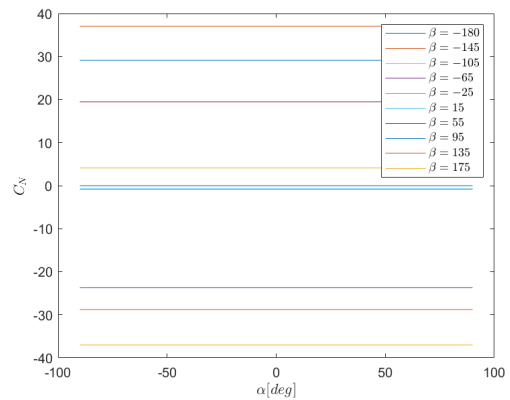
(f) N moment coefficient

Figure 2.27: Fuselage aerodynamic coefficient with respect to α
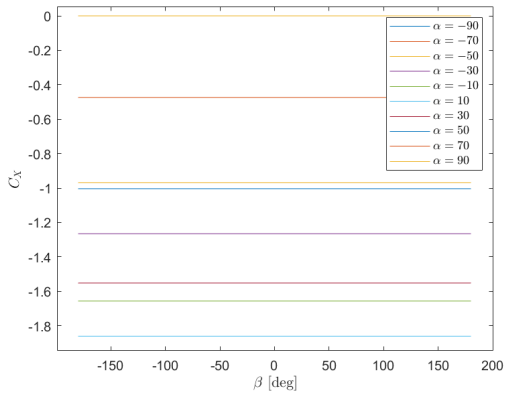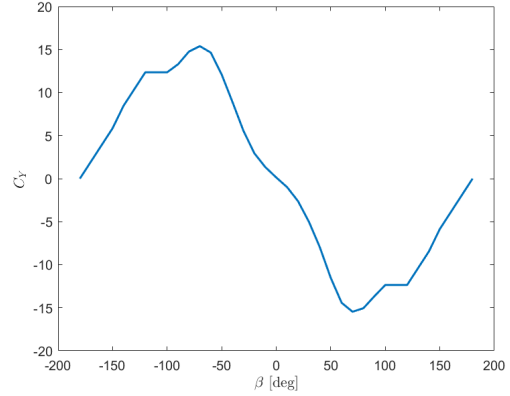
(a) X force coefficient

(b) Y force coefficient
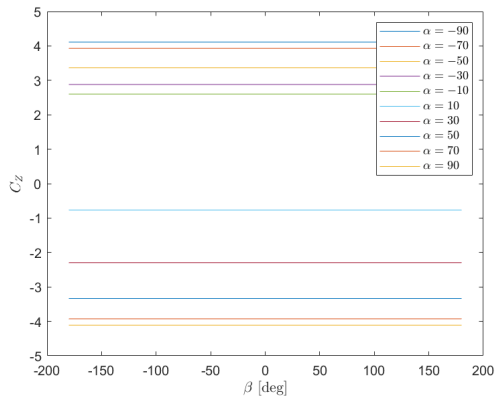
(c) Z force coefficient
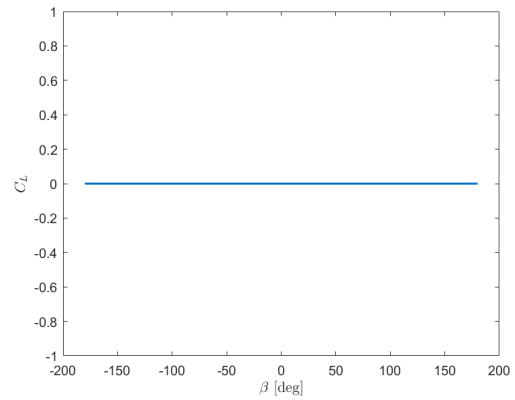
(d) L moment coefficient
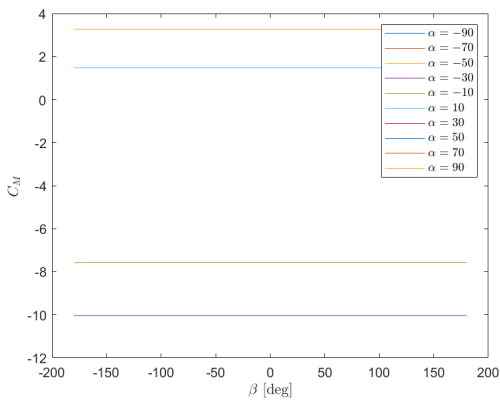
(e) M moment coefficient
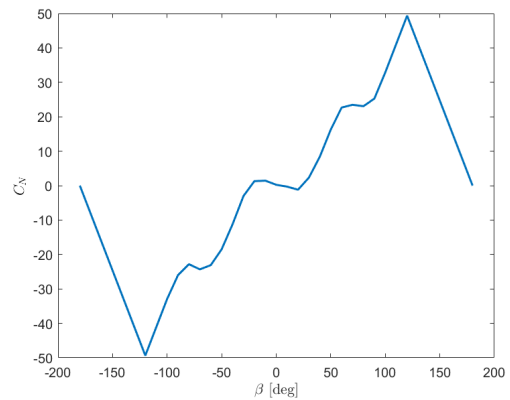
(f) N moment coefficient

Figure 2.28: Fuselage aerodynamic coefficient with respect to β

Figure 2.27-2.28, show the aerodynamic coefficient of the Bell412's fuselage. As can be

seen, with respect to the variation of the angle of incidence, there is also a difference in the coefficients with respect to the sideslip angle only in the case of the Y force and the yaw moment. Similarly, calculating the derivatives with respect to the variation of β, it can be seen that the variation of α only affects the derivatives of the forces X,Z and moments N.

2.8   Engines

An engine model has not been implemented in this work. Therefore, the thrust is only given by the projection of the vertical force generated by the rotor along the longitudinal axis. Furthermore, the torque and the angular velocity of the rotor are kept constant.

2.9   Equation of motion

After evaluating the overall loads as described in the previous sections, these are used to solve the following set of non-linear differential equations.

$$X = mgsin\theta + m\left(\dot{u} + qw - rv\right) \tag{2.84}$$

$$Y = -mgcos\theta sin\phi + m\left(\dot{v} + ru - pw\right) \tag{2.85}$$

$$Z = -mgcos\theta cos\phi + m\left(\dot{w} + pv - qu\right) \tag{2.86}$$

$$L = I_x\dot{p} - I_{xz}\dot{r} + qr(I_z - I_y) - I_{xz}pq \tag{2.87}$$

$$M = I_y\dot{q} + rq(I_x - I_z) + I_{xz} + (p^2 - r^2) \tag{2.88}$$

$$N = -I_{xz}\dot{p} + I_z\dot{r} + pq(I_y - I_x) + I_{xz}qr \tag{2.89}$$

The diagram 2.29 is representative of how this process takes place within the simulator.
To properly calculate the aerodynamic loads of each component, the kinematics variables obtained by equations 2.84-2.89 are trasformed from a body frame to a local frame. To perform it, the following calculations are carried out:

$$\vec{V_L} = \left(\vec{V_B} + \vec{\omega_B} \times \vec{r_B}\right) \tag{2.90}$$

$$\vec{\omega_L} = \vec{\omega_B} \tag{2.91}$$

where $\vec{V_B} = (u_B, v_B, w_B)^T$, $\vec{\omega_B} = (p_B, q_B, r_B)$.
In the specific case of the main rotor, an additional transformation is required to express

these values in the hub frame. It follows that the main rotor velocities are evaluated as:

$$\vec{V_L} = L_{B2H} \left(\vec{V_B} + \vec{\omega_B} \times \vec{r_B} \right) \tag{2.92}$$

$$\vec{\omega_L} = L_{B2H} \vec{\omega_B} \tag{2.93}$$

where the matrix L_{B2H} is given by:

$$L_{B2H} = \begin{bmatrix} c_{is} & 0 & s_{is} \\ 0 & 1 & 0 \\ -s_{is} & 0 & c_{is} \end{bmatrix} \tag{2.94}$$
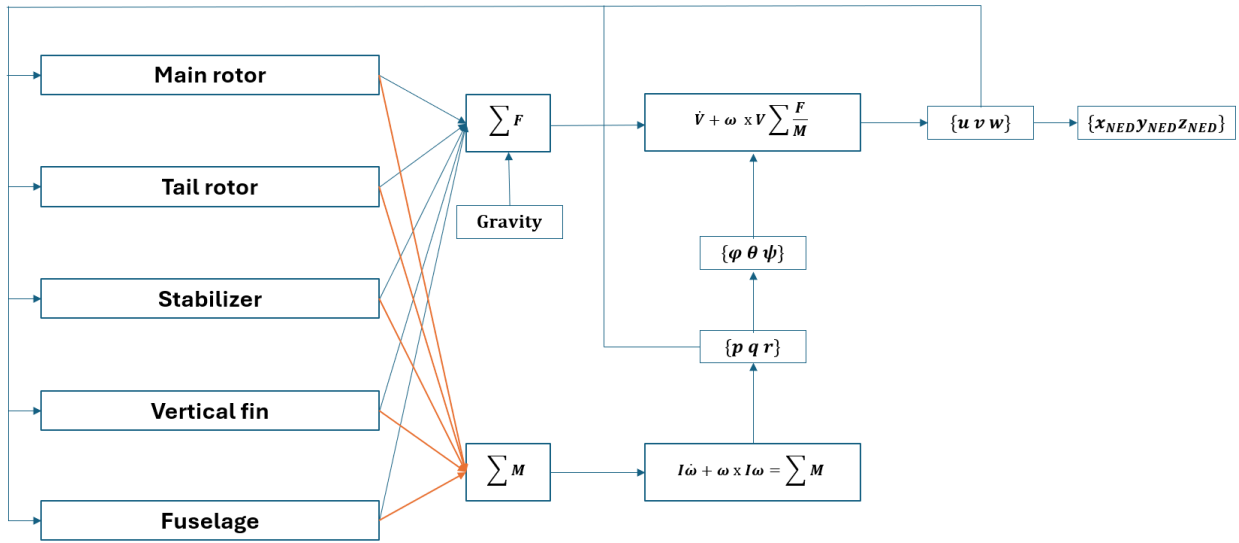
Figure 2.29: Simulator scheme

2.10 Model structure

Following the scheme in figure 2.29, the model is made up of specific blocks within which equations of each component are implemented and aerodynamic coefficients are calculated. In particular, each block follows the scheme showed in the figure 2.30
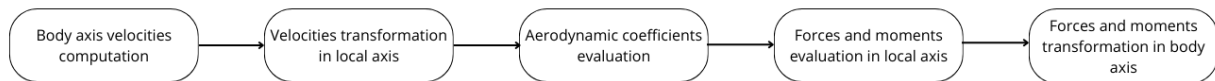
Figure 2.30: General scheme implementation

In the particular case of the main rotor, there is a sub-block dedicated to solving first the inflow and then the flapping dynamics in the tip path plane, as described in figure 2.31. The resulting coefficients are then used as input to the rest of the model.
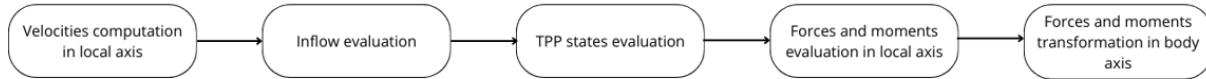
Figure 2.31: Main rotor scheme

Once the total forces and moments have been calculated, they are passed to the Simulink 6DOF block, which outputs the kinematic variables in both body and inertial axes. Variables in the body axes are fed back to the model, while those in the inertial axes are used to monitor the simulation. There are also two control input blocks at the beginning of the model, as shown in figure 2.32. The first is used to call the model within the trim calculation routine, as explained in the next section, while the second is used to test the trim with the calculated equilibrium conditions and to perform simulations. It is important to specify that the input blocks are connected one at a time, depending on the type of simulation to be run.
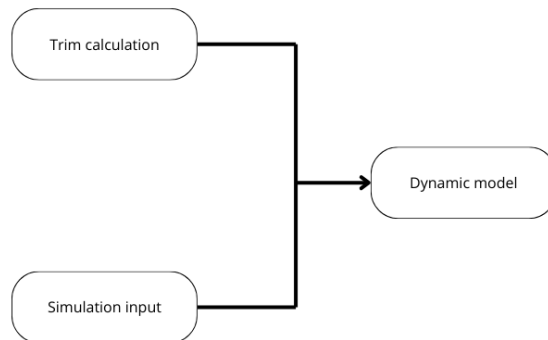
Figure 2.32: Input model

Chapter 3

Model validation

To validate the model, results were compared with simulations given by the FlightLab flight simulator. Results for the hover conditon and forward flight at 30,60,90 and 120 knots were achieved by giving doublet inputs of collective, cyclic and pedal.First, a description of the trim algorithm used is made, comparing the model and FlightLab results. Next, numerical simulations are shown.

3.1 Trim

From a theoretical point of view, the trim is defined like a state where all the rates of change of the state variables are equals to zero.The trim problem can be then expressed by the following equation:

$$\nabla f(x, u, t) = 0 \tag{3.1}$$

This is equal to state that the sum of all forces and moments is equal to zero. Finding an optimum trimmming point is an hard task in the study of helicopter flight dynamics, since the number of state that must be determined is really high. In this case, the vector state is defined as:

$$x^T = \{x, y, z, u, v, w, \phi, \theta, \psi, p, q, r, \lambda_{MR}, a, \dot{a}\}^T \tag{3.2}$$

where $a^T = \{a_0, a_1, b_1\}^T$, $\dot{a}^T = \left\{\dot{a_0}, \dot{a_1}, \dot{b_1}\right\}^T$. The input vector is defined as:

$$u^T = \{\theta_0, \theta_{1s}, \theta_{1c}, \theta_p\}^T \tag{3.3}$$

A set of non linear equation must be solved to satisfy the relation 3.1 and find the global minima. It is really important to choose properly the initial condition in order to avoid local minima and instability.

3.1.1 Trim algorithm

In literature, many examples are reported in details. In [13] is described the trim evaluation using an AFCS to stabilize the helicopter at the desired state, instead in [12] a genetic alghoritm is used to find the global minima of the problem. Again, Padfield [6] proposed a trim method whereby equilibrium is first established in the longitudinal plane and then in the latero-directional plane. However, the most classic approaches are those that make use of a descent method such as the gradient method, whereby states are perturbed as an input condition changes. In this way, the optimal condition is calculated from a given set of initial conditions, varied to obtain the optimal trim condition.

For the present work, an optimisation algorithm of the type fmincon was first tried, as proposed in [11]. This type of code has as its main objective the optimisation of a cost function varying the state and input variables within a specified range. In the case of the trim calculation, since the accelerations must be zero, the objective function was the sum of the absolute values of all the accelerations: linear, angular, flapping. As this type of approach did not give the desired results, it was preferred to call the Simulink model directly through the trim Matlab routine and to calculate the equilibrium state using the Sequential Quadratic Programming (SQP) method. The convergence or non-convergence of the algorithm is determined by the choice of initial conditions, which if poorly placed can lead to divergence of the calculation. As described in [1], SQP consists of three stages:

- Updating Hessian Matrix
- QPS
- Initialization and search of the minimum

First af all, at each iteration an approximation of the Hessian matrix is calulated as:

$$H_{k+1} = H_k + \frac{q_k q_k^T}{q_k^T s_k} - \frac{H_k s_k s_k^T H_k^T}{s_k^T H_k s_k} \tag{3.4}$$

where $s_k = x_{k+1} - x_k$ and

$$q_k = \left(\nabla f(x_{k+1}) + \sum_{i=1}^{m} \lambda_i \cdot \nabla g_i(x_{k+1}) \right) - \left(\nabla f(x_k) + \sum_{i=1}^{m} \lambda_i \cdot \nabla g_i(x_k) \right) \tag{3.5}$$

At this stage of the algorithm, the states q_k such that $q_k^T s_k < 0$ are modified so that this relationship is positive and the Hessian matrix is positive. The states that instead satisfy the relation are modified as little as possible. The procedure is repeated until a given tolerance

is satisfied.

At each stage, a Quadratic Problem is solved in the following form:

$$\min_{d \in R^n} q(d) = \frac{1}{2} d^T H d + c^T d$$

$$A_i d = b_i, \quad i = 1, ..., m_e \tag{3.6}$$

$$A_i d \leq b_i, \quad i = m_e + 1, ..., m$$

First, a feasible point is calculated. Secondly, a series of points converging to the solution is generated. In the end, the state q is evaluated as a function of a generic vector p, in the following way:

$$q(p) = \frac{1}{2} p^T Z_k^T H Z_k p + c^T Z_k p \tag{3.7}$$

where Z_k is such that $d_k = Z_k p$. The solution is then differentiated to find the minimum such that:

$$\nabla q(p) = Z_k^T H Z_k p + Z_k^T c = 0 \tag{3.8}$$

The method evaluates then the solution in the form:

$$x_{k+1} = x_k + \alpha d_k \tag{3.9}$$

where the step lenght α is given by:

$$\alpha = \min_{i \in \{1, ..., m\}} \left\{ \frac{-(A_i x_k - b_i)}{A_i \hat{d}_k} \right\} \tag{3.10}$$

After finding a feasible initial condition, the algorithm is initialised and proceeds with the calculation of the equilibrium state and the search for the minimum equilibrium point.

3.1.2 Trim validation

The numerical results obtained with the trim algorithm are shown below and enlisted with the trim results given by FlightLab. They are divided into tables according to the flight condition analysed. Analyses were carried out considering an altitude of 1000 ft and zero flight path or sideslip angle. Furthermore, only the fixed point or pure forward flight condition was analysed, without considering any turns, angular velocities or reverse flight.

Variable	Model	FlightLab
$\phi[deg]$	-2.555	-1.7805
$\theta[deg]$	5.0026	5.0839
$\psi[deg]$	0	0
$p[deg/s]$	0	0
$r[deg/s]$	0	0
$q[deg/s]$	0	0
$z[m]$	-304.8	-304.8
$u[m/s]$	0	0
$v[m/s]$	0	0
$w[m/s]$	0	0
$a_0[deg]$	2.4134	2.3617
$a_1[deg]$	-0.5214	-0.1375
$b_1[deg]$	-0.5099	-1.0600
$\theta_0[deg]$	7.7591	7.8818
$\theta_{1s}[deg]$	0.0784	0.3310
$\theta_{1c}[deg]$	-0.6068	-1.0847
$\theta_p[deg]$	-9.1500	-10.9780

Table 3.1: Hover trim condition

Variable	Model	FlightLab
$\phi[deg]$	-1.7702	-0.9974
$\theta[deg]$	4.7956	4.7178
$\psi[deg]$	0	0
$p[deg/s]$	0	0
$r[deg/s]$	0	0
$q[deg/s]$	0	0
$z[m]$	-304.8	-304.8
$u[m/s]$	15.3994	15.4
$v[m/s]$	-0.0223	-0.0219
$w[m/s]$	1.2915	1.27
$a_0[deg]$	2.2804	2.2242
$a_1[deg]$	-0.3325	-0.3266
$b_1[deg]$	-0.4125	-0.0115
$\theta_0[deg]$	6.7210	6.4213
$\theta_{1s}[deg]$	1.2210	1.5984
$\theta_{1c}[deg]$	-0.6273	-2
$\theta_p[deg]$	-5.6720	-6.2712

Table 3.2: 30 knots trim condition

Variable	Model	FlightLab
$\phi[deg]$	-1.4081	-0.7566
$\theta[deg]$	3.6107	3.7375
$\psi[deg]$	0	0
$p[deg/s]$	0	0
$r[deg/s]$	0	0
$q[deg/s]$	0	0
$z[m]$	-304.8	-304.8
$u[m/s]$	30.8061	30.8167
$v[m/s]$	-0.2504	-0.0263
$w[m/s]$	1.9387	2.0106
$a_0[deg]$	2.1944	2.1152
$a_1[deg]$	-0.4299	-0.6191
$b_1[deg]$	-0.2751	0.2407
$\theta_0[deg]$	5.56	5.4798
$\theta_{1s}[deg]$	1.933	2.4458
$\theta_{1c}[deg]$	-0.6936	-1.508
$\theta_p[deg]$	-3.4250	-3.5803

Table 3.3: 60 knots trim condition

Variable	Model	FlightLab
$\phi[deg]$	-1.4923	-0.9912
$\theta[deg]$	2.7879	2.3990
$\psi[deg]$	0	0
$p[deg/s]$	0	0
$q[deg/s]$	0	0
$r[deg/s]$	0	0
$z[m]$	-304.8	-304.8
$u[m/s]$	46.221	46.2237
$v[m/s]$	-0.0003	-0.0333
$w[m/s]$	1.934	1.9363
$a_0[deg]$	2.2403	2.1267
$a_1[deg]$	-1.0318	-1.2777
$b_1[deg]$	-0.3497	0.0573
$\theta_0[deg]$	6.114	6.0140
$\theta_{1s}[deg]$	3.399	3.8304
$\theta_{1c}[deg]$	-0.9572	-1.0409
$\theta_p[deg]$	-3.063	-3.3634

Table 3.4: 90 knots trim condition

Variable	Model	FlightLab
$\phi[deg]$	-2.3794	-1.5936
$\theta[deg]$	0.7646	1.0089
$\psi[deg]$	0	0
$p[deg/s]$	0	0
$r[deg/s]$	0	0
$q[deg/s]$	0	0
$z[m]$	-304.8	-304.8
$u[m/s]$	61.4451	61.5671
$v[m/s]$	-0.0299	-0.0299
$w[m/s]$	0.3431	1.0834
$a_0[deg]$	2.3491	2.2471
$a_1[deg]$	-1.6100	-2.5223
$b_1[deg]$	-0.6305	-0.2808
$\theta_0[deg]$	7.8190	7.7191
$\theta_{1s}[deg]$	5.4930	6.2928
$\theta_{1c}[deg]$	-1.3990	-0.7787
$\theta_p[deg]$	-3.9700	-4.3698

Table 3.5: 120 knots trim condition

Looking at the figure 3.1, it can be seen that the data for collective, pedal and longitudinal cyclic are very close to the FlightLab data, with an error of about half a degree, except in hover, where the pedal is much lower. The answer to this can be found in the simplified model of the tail rotor, which, by not taking into account dynamic inflow or flapping dynamics, is too powerful in the fixed-point flight condition compared to the real situation. As the speed increases, these two dynamics are dampened, also by the interaction with the main rotor wake, so that the difference is reduced. The differences are greater for the lateral cyclic control, for which results show the greatest discrepancies. This is due to the lack of a dynamic inflow within the model, whereby the coupling dynamics between the longitudinal and lateral planes are lost, resulting in a difference in the calculated control inputs. This is also reported in [16], where it is shown that, for the model described by Cheng and used in this work, the addition of this dynamic leads to an alignment of the cyclic results with the real ones. This can also be seen in the results for TPP angles and pitch and roll angles, shown in figure 3.1,3.2. Indeed, it can be observed that the coning angle, as well as the pitch angle and longitudinal TPP angle, are quite representative of the FlightLab simulations, while the lateral TPP and roll angle highlight the problems discussed above.
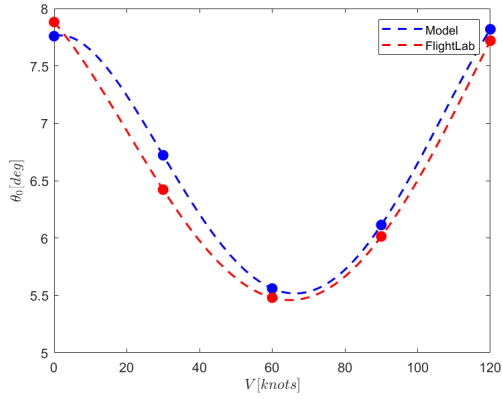
(a) Collective
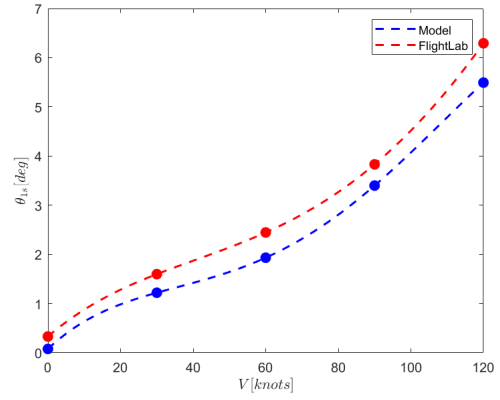
(b) Longitudinal cyclic
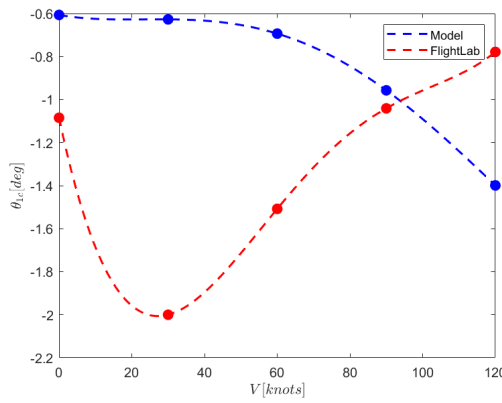
(c) Lateral cyclic
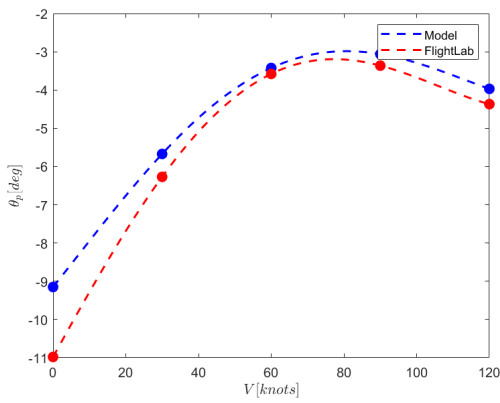
(d) Pedal
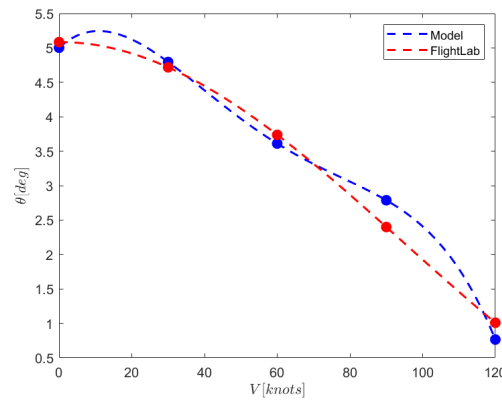
(e) Pitch
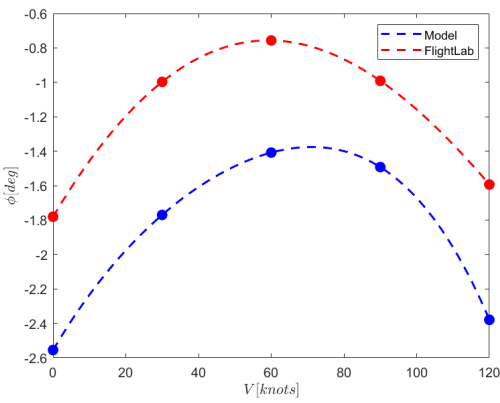
(f) Roll

Figure 3.1: Comparison between trim input of the model and FlightLab
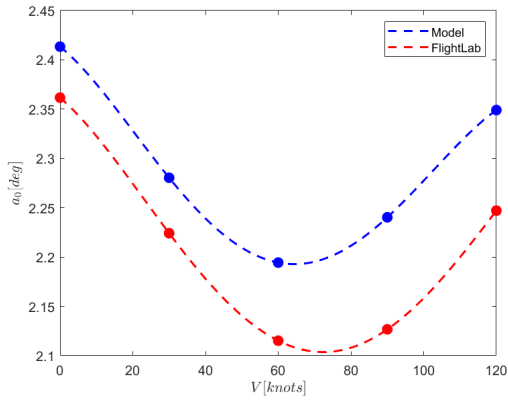
(a) Coning TPP angle
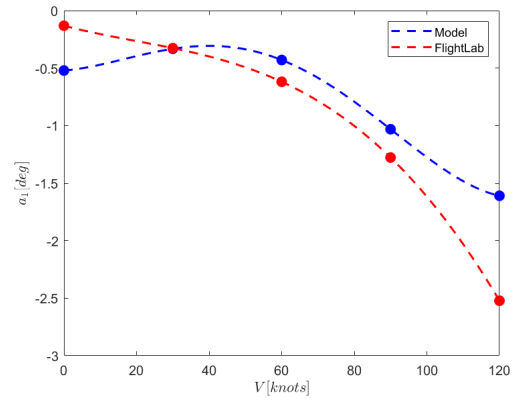
(b) Longitudinal TPP angle
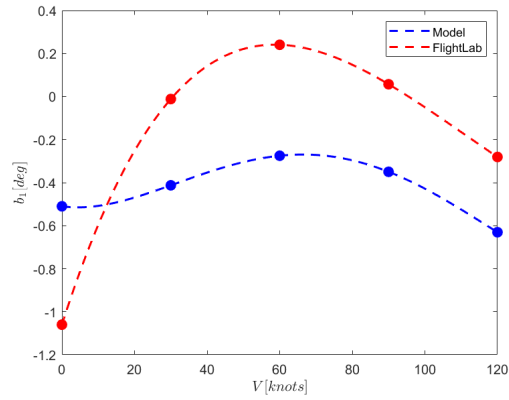
(c) Lateral TPP angle

Figure 3.2: Comparison between TPP trim state of the model and FlightLab results

47

3.2   Simulations

Numerical simulations were performed for each flight conditions to validate the model. The tests carried out concern simulations obtained by giving doublet type inputs with an amplitude of 0.5 inches of the type shown in figure 3.3.
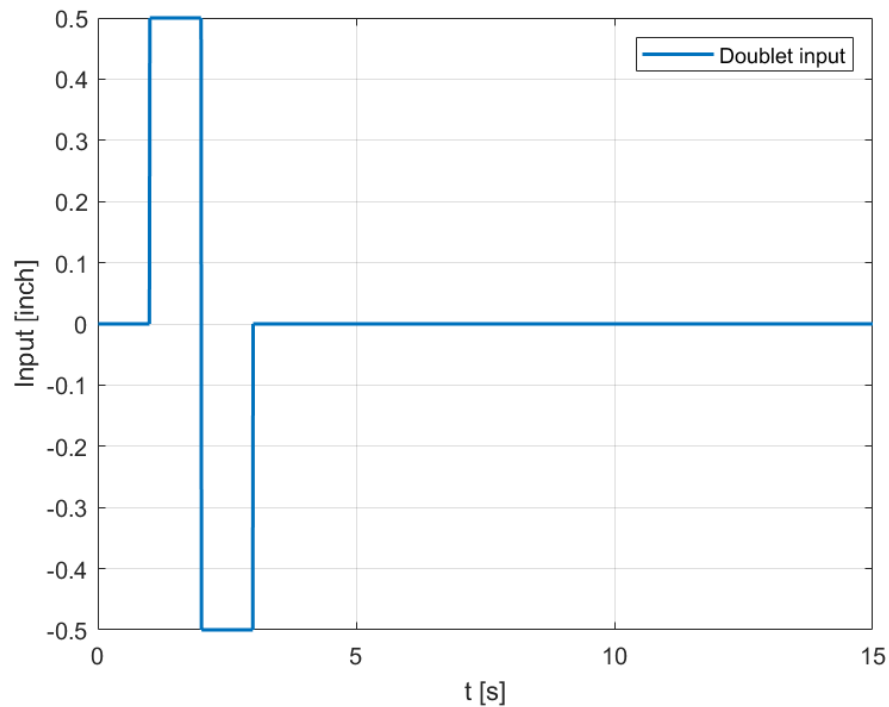
Figure 3.3: Doublet input

The flight conditions analysed were chosen to cover the greatest possible range within the flight envelope. In particular, the fixed-point flight condition is particularly important given its peculiarity for helicopters. Moreover, this is the initial condition for the study of axial flight and the subsequent VRS analysis, as presented in the following chapter.
For ease of discussion, only results of angular rates and linear velocities are reported.

3.2.1 Hover condition

Collective doublet

(a) Rates

(b) Linear velocities
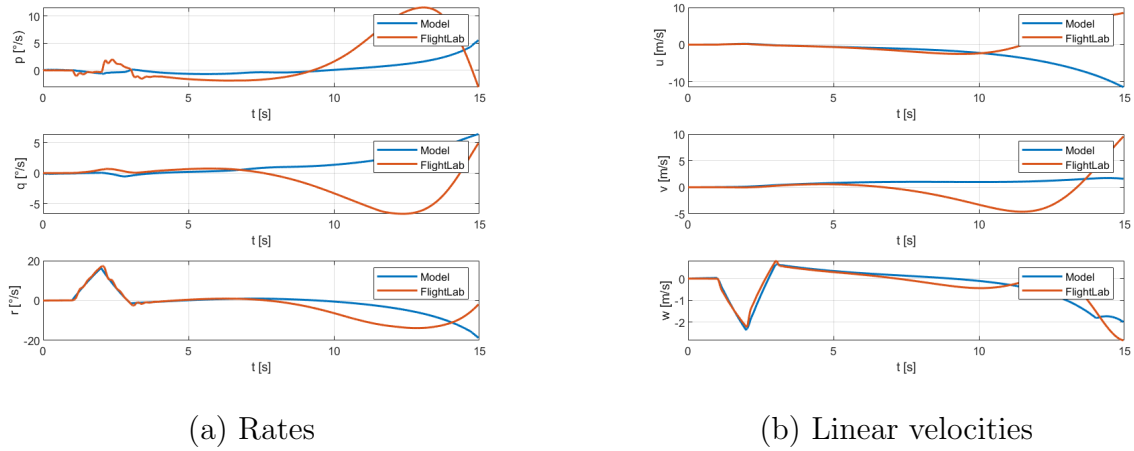
Figure 3.4: Response to a doublet collective input at hover

(a) Rates

(b) Linear velocities
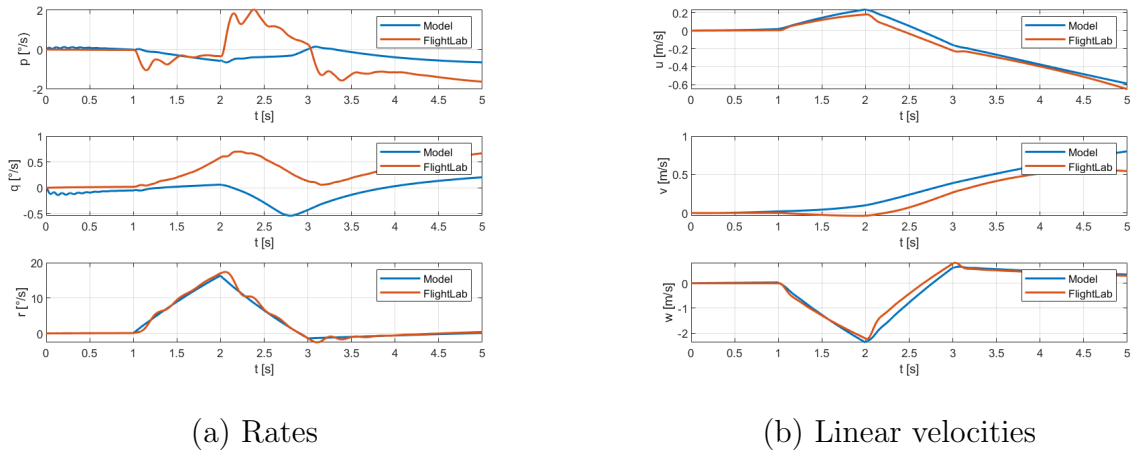
Figure 3.5: Zoom of the response to a doublet collective input at hover

Longitudinal doublet
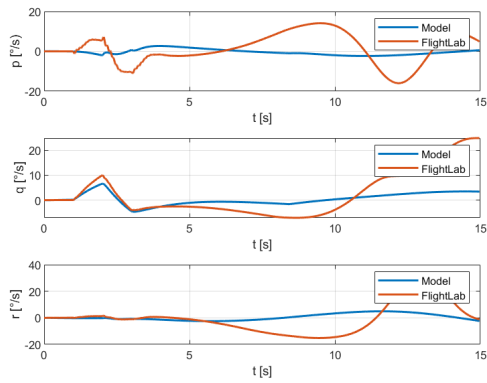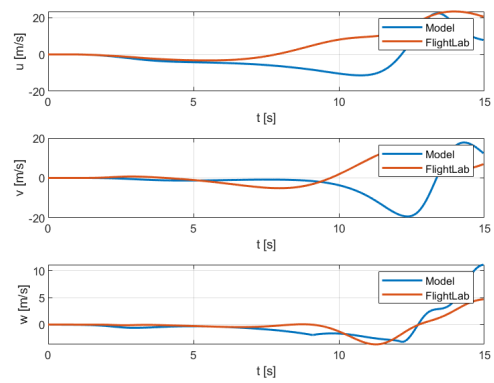
(a) Rates

(b) Linear velocities

Figure 3.6: Response to a doublet longitudinal input at hover
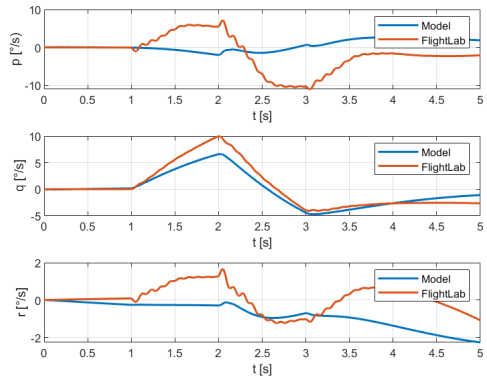
(a) Rates
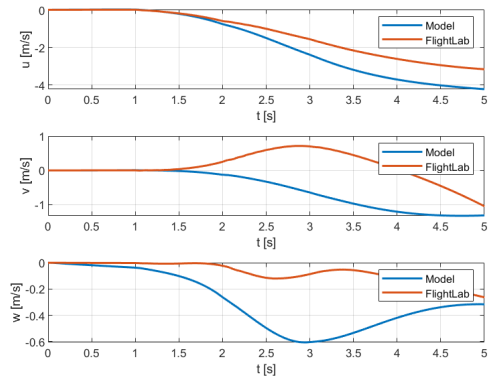
(b) Linear velocities

Figure 3.7: Zoom of the response to a doublet longitudinal input at hover

Lateral doublet
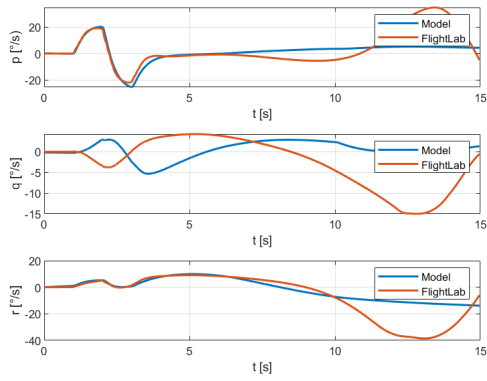
(a) Rates
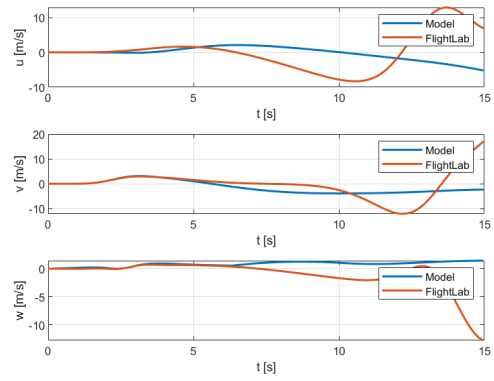
(b) Linear velocities

Figure 3.8: Response to a doublet lateral input at hover
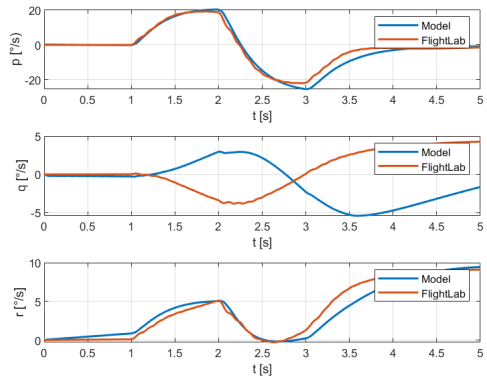
(a) Rates
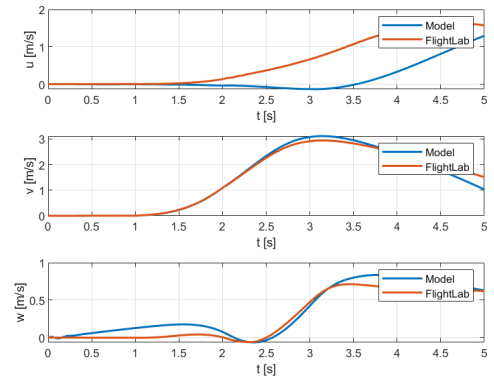
(b) Linear velocities

Figure 3.9: Zoom of the response to a doublet lateral input at hover

Pedal doublet
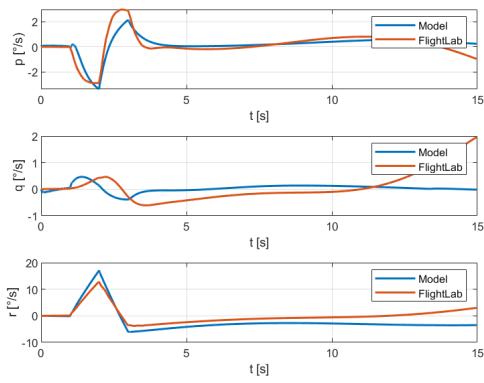
(a) Rates
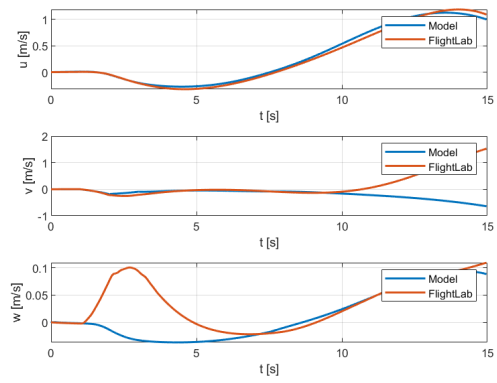
(b) Linear velocities

Figure 3.10: Response to a doublet pedal input at hover
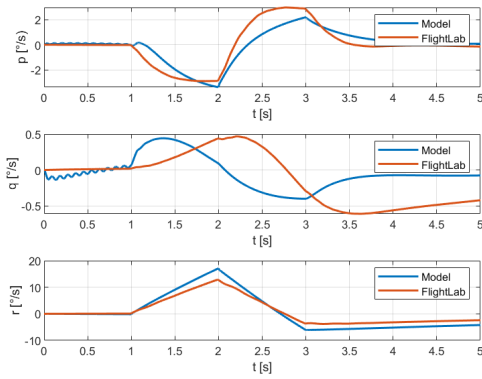
(a) Rates
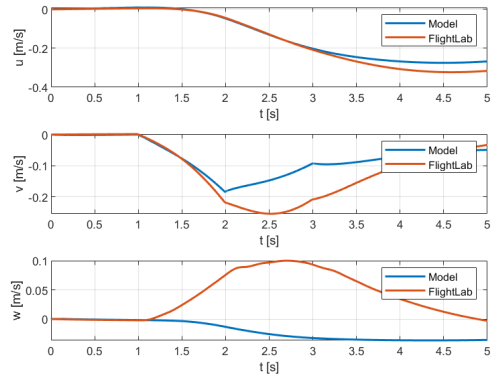
(b) Linear velocities

Figure 3.11: Zoom of the response to a doublet pedal input at hover

3.2.2 Forward flight at 30 knots

Collective doublet

(a) Rates

(b) Linear velocities
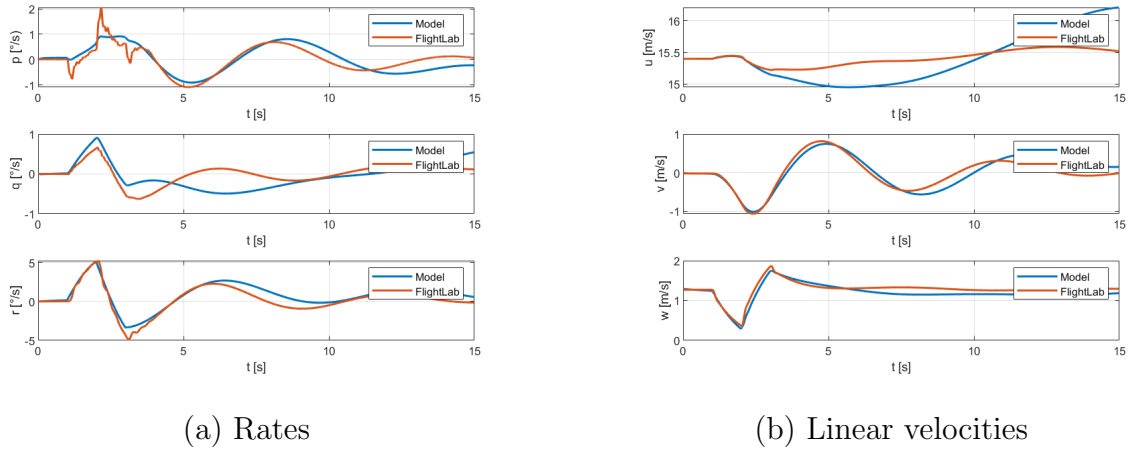
Figure 3.12: Response to a doublet collective input at 30 knots

Longitudinal doublet

(a) Rates

(b) Linear velocities
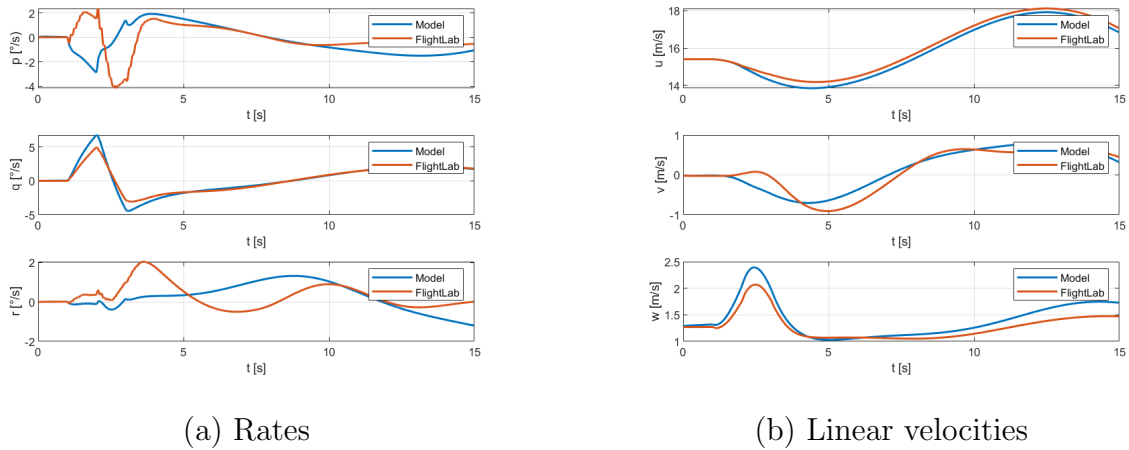
Figure 3.13: Response to a doublet longitudinal input at 30 knots

Lateral doublet
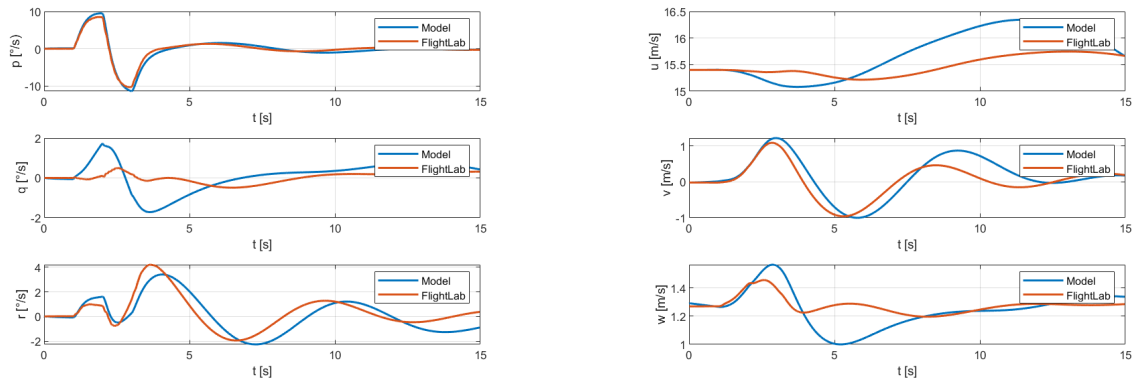
(a) Rates

(b) Linear velocities

Figure 3.14: Response to a doublet lateral input at 30 knots

Pedal doublet
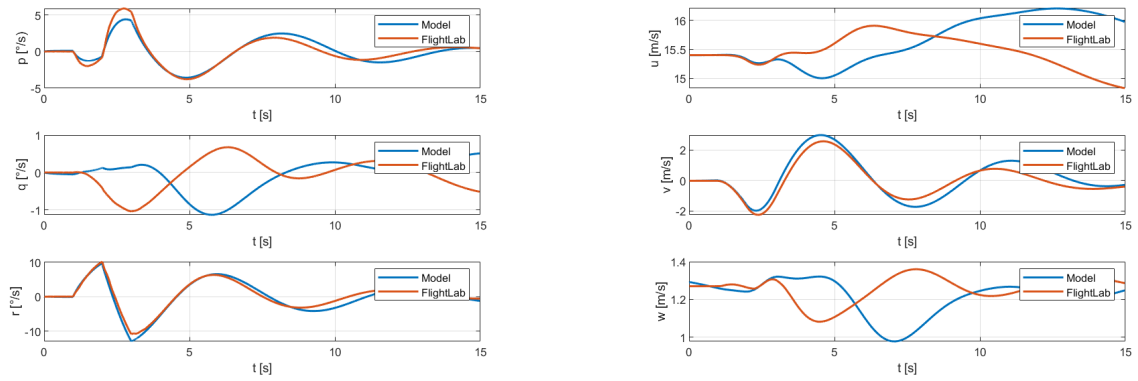
(a) Rates

(b) Linear velocities

Figure 3.15: Response to a doublet pedal input at 30 knots

3.2.3 Forward flight at 60 knots

Collective doublet

(a) Rates

(b) Linear velocities
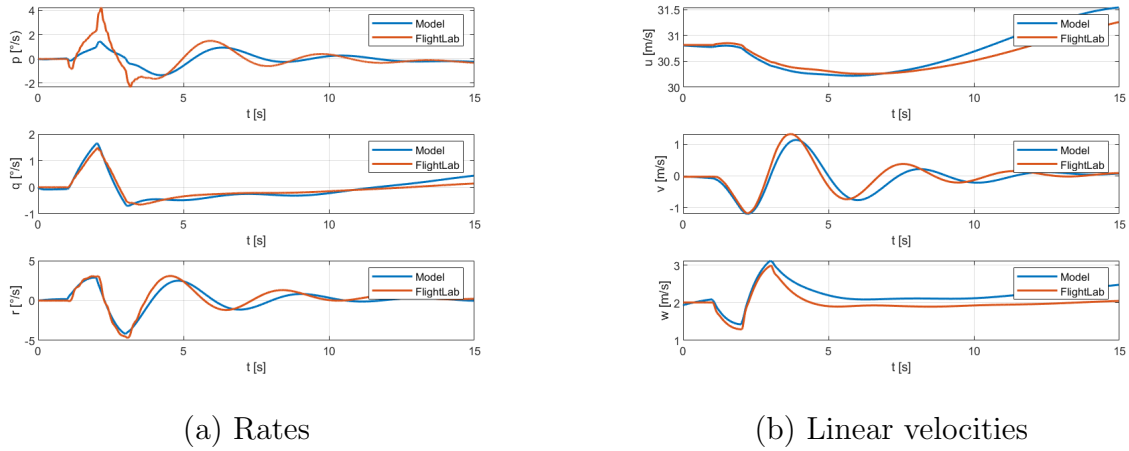
Figure 3.16: Response to a doublet collective input at 60 knots

Longitudinal doublet

(a) Rates

(b) Linear velocities
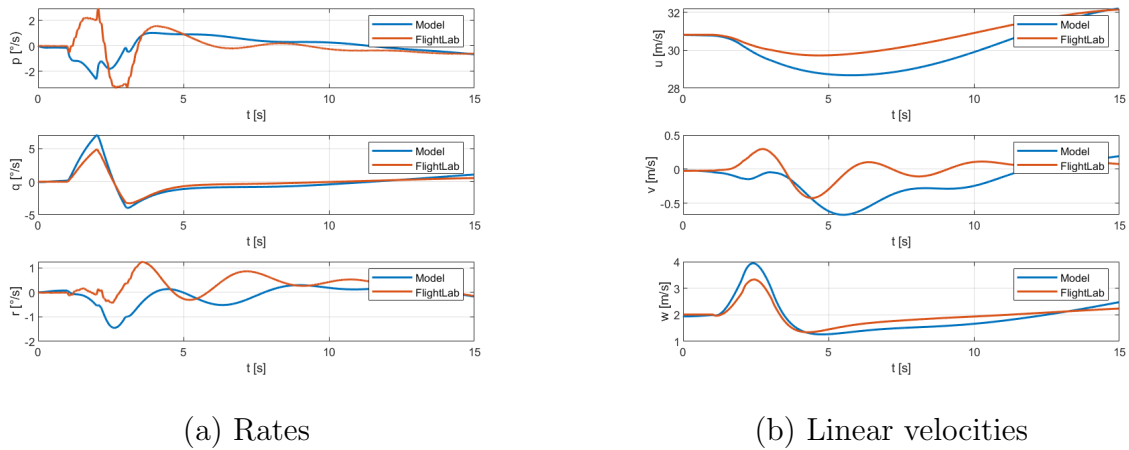
Figure 3.17: Response to a doublet longitudinal input at 60 knots

Lateral doublet
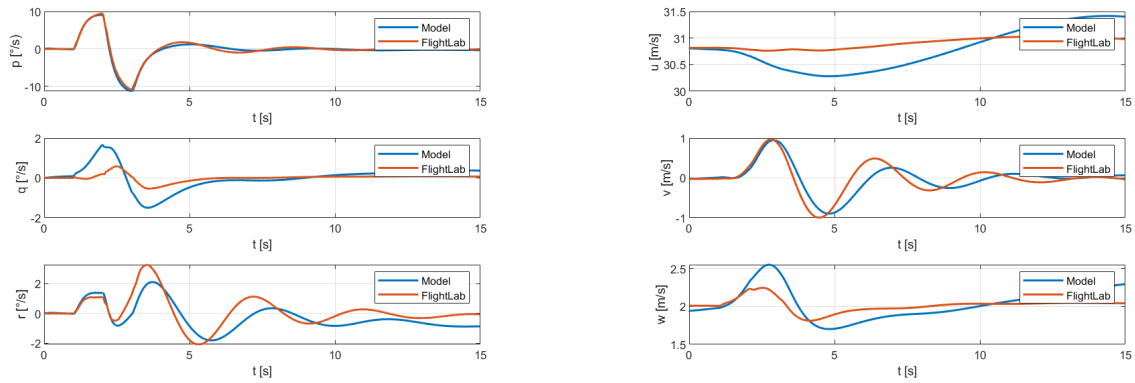
(a) Rates

(b) Linear velocities

Figure 3.18: Response to a doublet lateral input at 60 knots

Pedal doublet
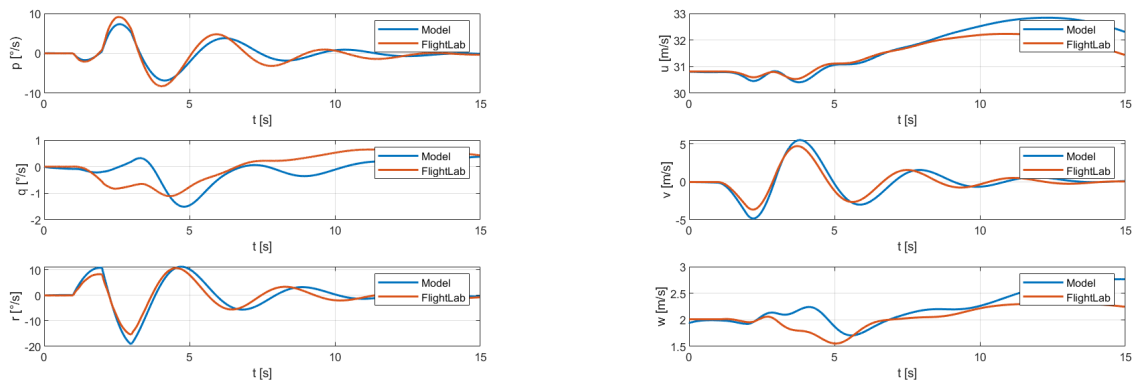
(a) Rates

(b) Linear velocities

Figure 3.19: Response to a doublet pedal input at 60 knots

3.2.4 Forward flight at 90 knots

Collective doublet

(a) Rates

(b) Linear velocities
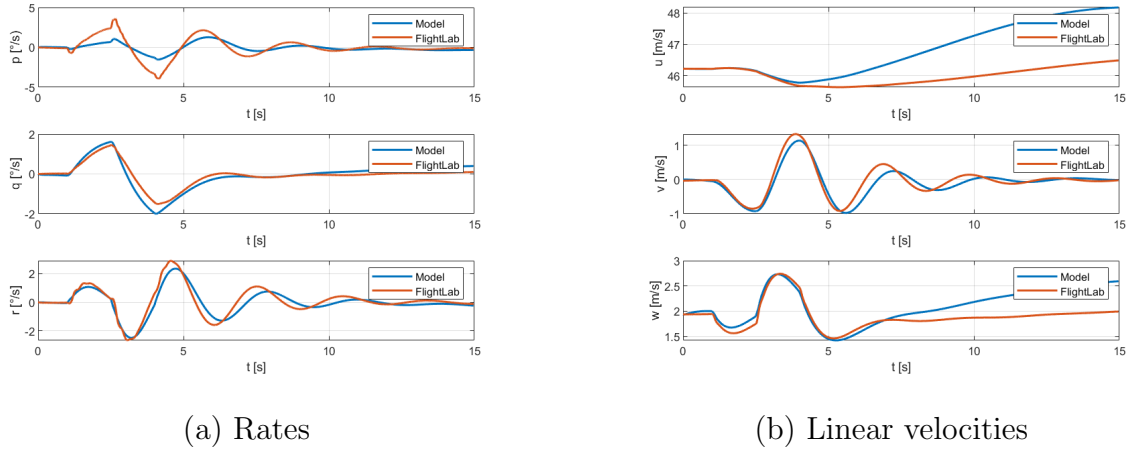
Figure 3.20: Response to a doublet collective input at 90 knots

Longitudinal doublet

(a) Rates

(b) Linear velocities
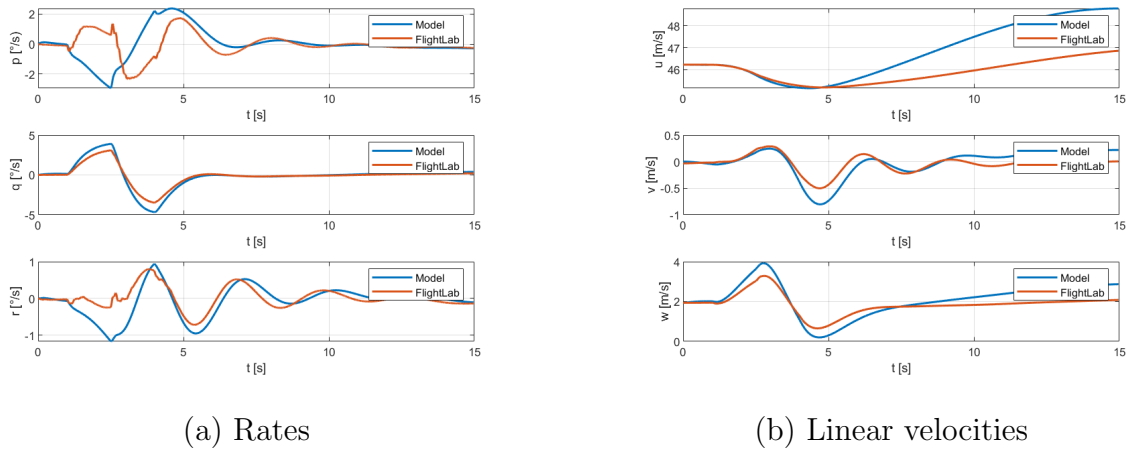
Figure 3.21: Response to a doublet longitudinal input at 90 knots

Lateral doublet
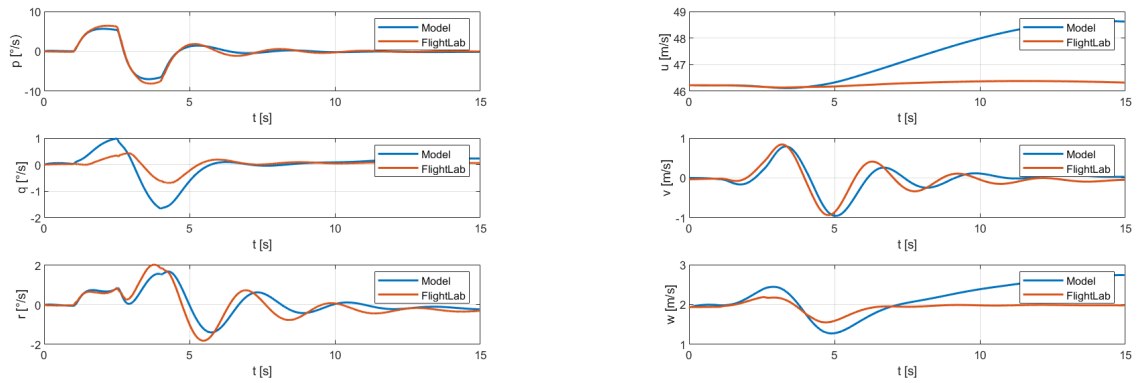
(a) Rates

(b) Linear velocities

Figure 3.22: Response to a doublet lateral input at 90 knots

Pedal doublet
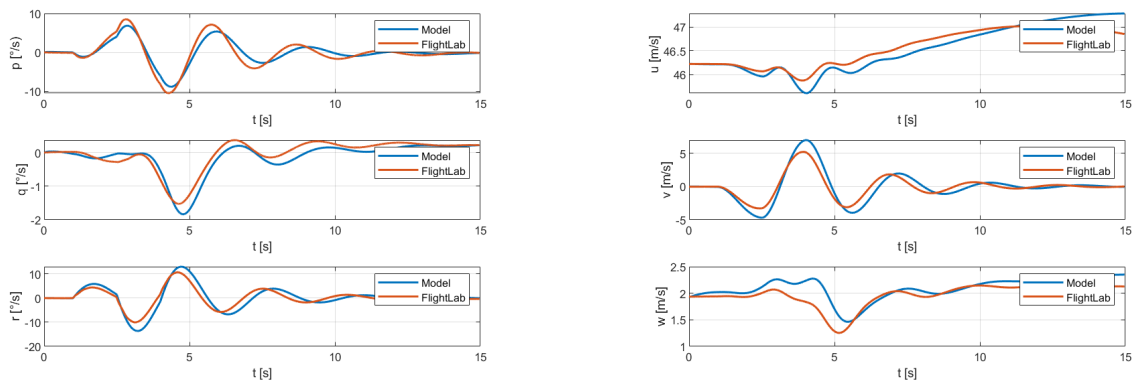
(a) Rates

(b) Linear velocities

Figure 3.23: Response to a doublet pedal input at 90 knots

3.2.5 Forward flight at 120 knots

Collective doublet
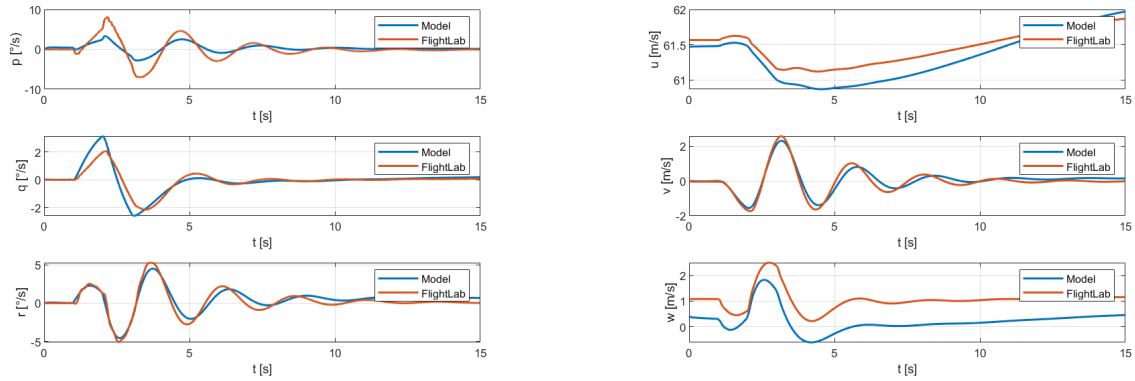
(a) Rates

(b) Linear velocities

Figure 3.24: Response to a doublet collective input at 120 knots

Longitudinal doublet
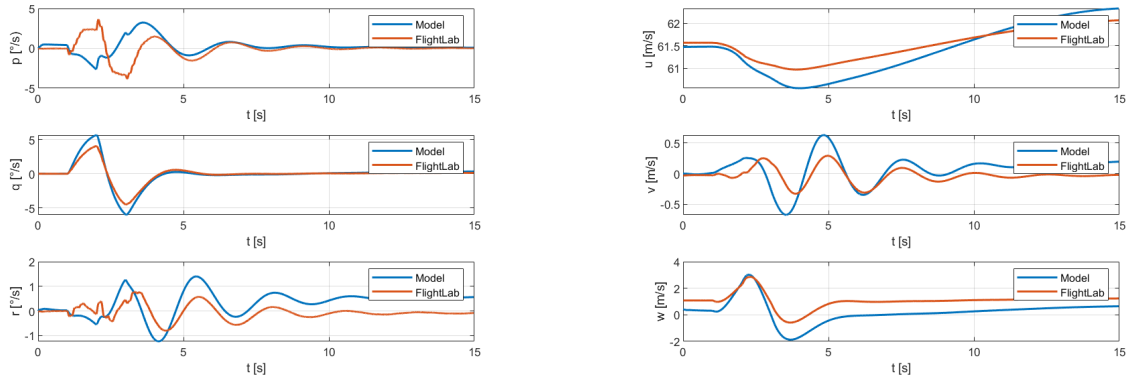
(a) Rates

(b) Linear velocities

Figure 3.25: Response to a doublet longitudinal input at 120 knots

Lateral lateral
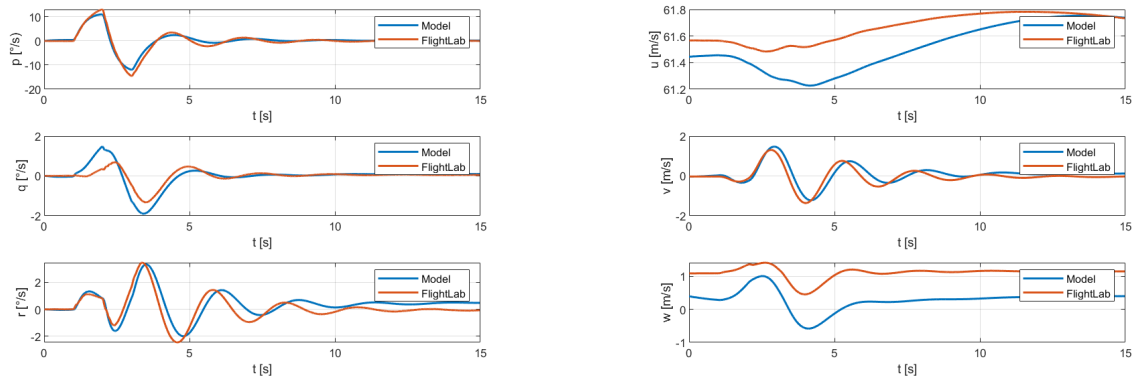
(a) Rates

(b) Linear velocities

Figure 3.26: Response to a doublet lateral input at 120 knots

Pedal doublet
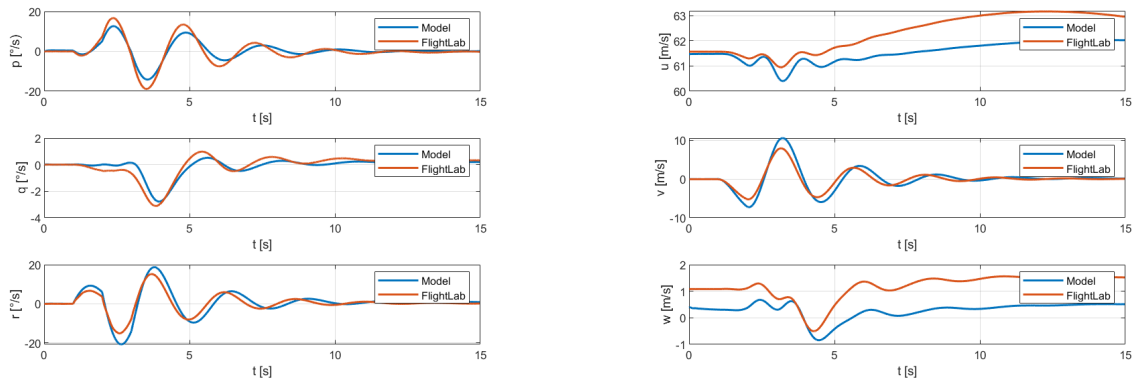
(a) Rates

(b) Linear velocities

Figure 3.27: Response to a doublet pedal input at 120 knots

3.3 Analysis of the results

Looking at the results, the following observations can be made.

Regarding the pitch and roll dynamics, it can be observed that the on-axis behaviour is consistent with what is shown by FlightLab, while the off-axis response is the opposite. The reason for this discrepancy is the modelling of the inflow.FlightLab implements a dynamic inflow model based on the Peters-He theory [15], while this work considers an uniform inflow. As pointed out by Padfield [6], dynamic inflow activates longitudinal and lateral coupling dynamics.

For example, considering a longitudinal velocity perturbation - remembering that the same reasoning applies to a lateral perturbation - this produces a variation in the wake angle and consequently an increase in the longitudinal inflow. The following relationship applies:

$$\frac{\partial \lambda_{1c}}{\partial \mu} \approx \frac{1}{2} \tag{3.11}$$

The inflow variation in turn causes a change in the blade incidence which is equivalent to a cyclic variation. This makes the lateral flapping angle to vary which is, according to the relationship, correlated with the rotor stiffness S_β:

$$\frac{\partial \beta_{1s}}{\partial \lambda_{1c}} = -\frac{1}{1 + S_\beta^2} \tag{3.12}$$

It is therefore clear that a velocity perturbation, due to a flapping angle change, induces a variation in the direction of the force components, leading to an asymmetry in the generated moments. This explains why the roll and pitch responses obtained with the implemented model show the opposite behaviour to that expected. In addition, combined to a flapping dynamic described in an Individual Blade Coordinate System as in the FlightLab model, dynamic inflow results in larger oscillations in the main rotor compared to those of the implemented model, which are instead damped immediately.

This behaviour can be observed in Figure 3.28, which shows the response of the main rotor following a collective doublet command at a flight condition of 60 knots. Furthermore, obsering figure 3.29, it can be seen that the relative error in the steady state is usually comprised between $2-8\%$, apart for the Y force which shows a greatest error due to the deficiencies of the model. The more damped dynamics of the TPP also cause major fluctuations in the error during transients due to the input given.

The dynamic inflow is therefore responsible for an altered off-axis behaviour of the helicopter. This can also be observed in the case of speeds. It can be seen that in the case of lateral
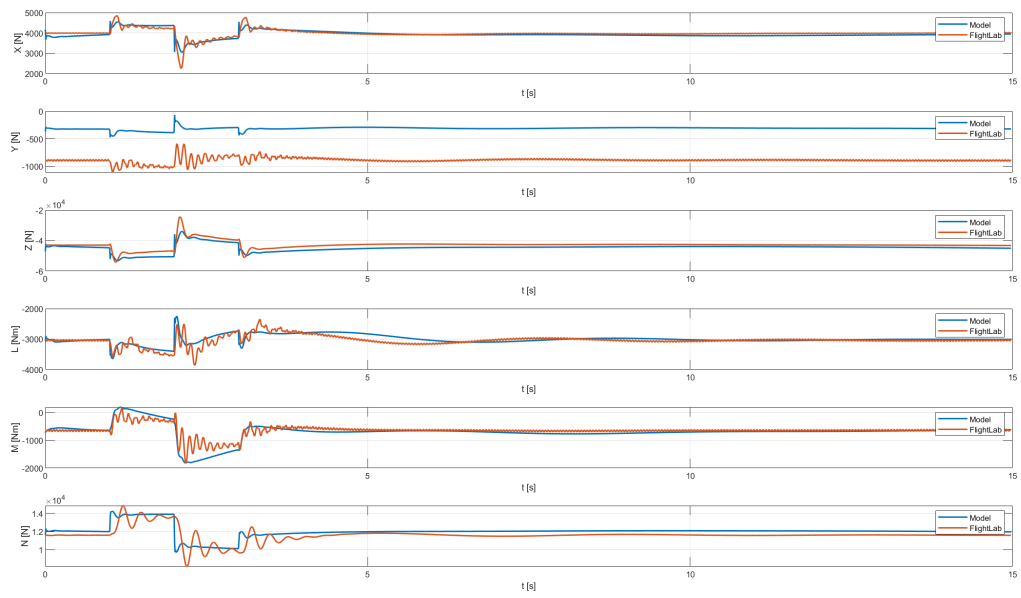
Figure 3.28: Main rotor response after a doublet collective input at 60 knots
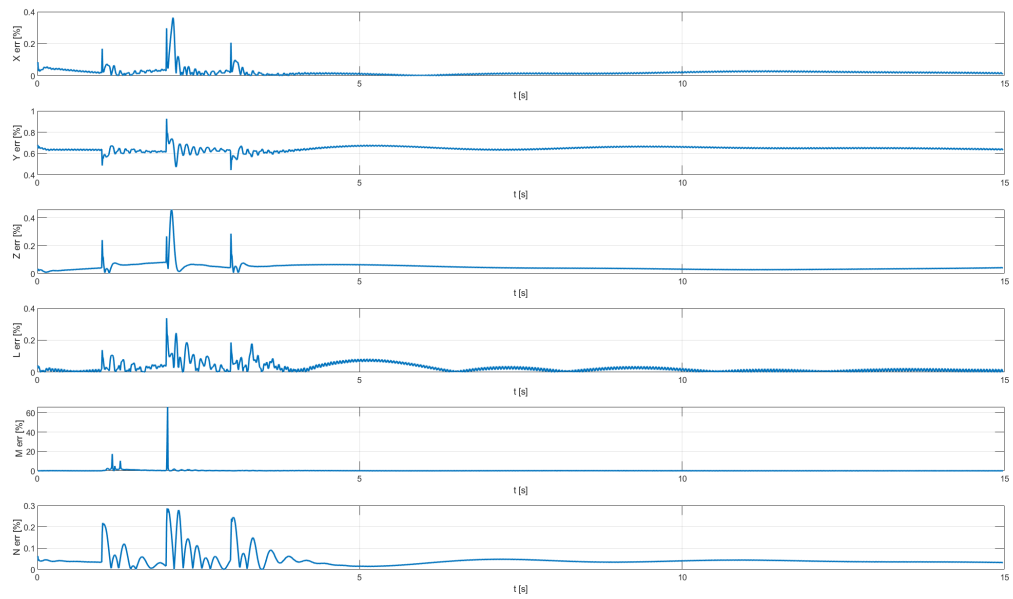
Figure 3.29: Main rotor relative error between the model and FlightLab

or cyclical control, the on-axis speed response is congruent with the expected one, while the longitudinal and vertical speeds show different responses. The same happens in the case of the longitudinal input, where the lateral speed does not give the expected results.

It can also be seen that as the speed increases, the differences in response become smaller and the simulations give results that are congruent with those of FlightLab. This is due to the fact that the stability of the helicopter increases. In fact, the contributions of the static and dynamic stability derivatives, such as X_u, M_u and M_w, increase in absolute value. This is also due to the fact that the stabiliser has a greater effect in damping pitching moment variations caused by a change in rotor thrust, as opposed to what happens at low speed or hover. In addition, the Z_w derivative stabilises as speed increases, making the helicopter less sensitive to changes in vertical speed.

Looking at the pitch response, there is a higher peak in the response compared to FlightLab. This can be attributed to a slight difference in the M_q derivative. As reported by Padfield, this is equal to:

$$(M_q)_h \approx -\frac{N_b S_\beta I_\beta \Omega}{I_{yy}} \left(1 + S_\beta \frac{\gamma}{16}\right) \tag{3.13}$$

This could be caused by a difference in the Lock number between the two models, as well as a difference in the mathematical model of the rotor, or in the angular velocity of the rotor. In FlightLab, tha rotor speed is not constant, as results in the model implemented since the engine is kept ideal. The calculation of the Lock number depends on both the geometric parameters of the airfoils and their aerodynamic coefficients, as shown in the following equation:

$$\gamma = \frac{\rho c a_0 R^4}{I_\beta} \tag{3.14}$$

As described in section 2.3.7, blades of the Bell 412 consist of four different airfoils and have a variable chord. FlightLab correctly takes this into account, whereas the developed model only considers a single airfoil profile and a constant chord along the blade. Another reason for the difference in pitch behaviour may be related to the implemented stabiliser model and a slight difference in the evaluation of the inflow velocities at the stabiliser and the angle of incidence.

The same can be seen for the roll and yaw response to a pedal input. Again, the model shows larger peaks, mainly due to the tail rotor model used. In fact, looking at the yaw response generated after a collective command, the two models have almost identical curves, so the main rotor is not responsible for this difference in yaw response. As for the case of

the M_q derivative, in this case is the N_r derivative that is affected. This is equal to:

$$N_r \approx -l_t \frac{M_a}{I_{zz}} Y_r \tag{3.15}$$

where M_a is the helicopter mass and Y_r is the sideforce generated by the tail rotor. The difference in response can therefore be attributed to a different calculated side force, which is found in the rotor model used. As can be seen in fiure 2.19, forces and moments generated by the model developed show larger peaks than the FlightLab model, so this proves that the model described in section 2.4 and used for this work is therefore too approximate.

Observing the response to a collective control input, without any coupling effects between the longitudinal and lateral planes, a higher fidelity can be noted between the obtained results and those from FlightLab.The most significant differences generally occur in the roll rate response, where the model appears more damped, and in the pitch rate response, where larger peaks are again observed.

Looking at the phases following the application of the doublet, an asymmetry in the results can often be observed, especially in hover. This difference is due to the effect of the main rotor's downwash on the empennages, fuselage and tail rotor. The downwash causes a variation in the local vertical speed, which in turn leads to a different distribution of the dynamic pressure and consequently of the forces. In addition, the effect of the downwash varies for each flight condition, so it must be studied carefully to obtain the most accurate results. In FlightLab, the interference of the main rotor is described in [9], while in the implemented model it is taken into account by a parameter k that varies between 0 and 1, as described by the equations 2.50,2.65,2.76. The implementation of more accurate wake models, beyond simple tuning, would significantly improve the quality of the simulations. In fact, the tuning of the k coefficient is based on empirical considerations, whereas a more accurate wake model would allow the actual percentage of area affected by the main rotor downwash to be taken into account. In this way, the response of the model would be more plausible.

Looking at the speeds, it can be seen that the trim value calculated at high speed sometimes differs from that proposed by FlightLab, especially in the longitudinal and vertical components. This is due to a difference in the output required by the trim algorithm used and that of this model. In fact, in this work, the speed components are choosen as initial conditions at the user's discretion and let free to vary, while the ramp angle or sideslip angle are not considered as trim variables.

Chapter 4

VRS modeling

4.1 Vortex Ring State introduction

The last part of the project concerns the study of the Vortex Ring State. This was done by implementing two mathematical models: Young and Johnson. Both are aimed at finding a solution to the calculation of the inflow in the region where Momentum Theory fails to calculate this parameter. If with the first model a simple approximation is given, the second proposes to describe the invalidity region with a third-degree polynomial using a calculation algorithm based on experimental data.
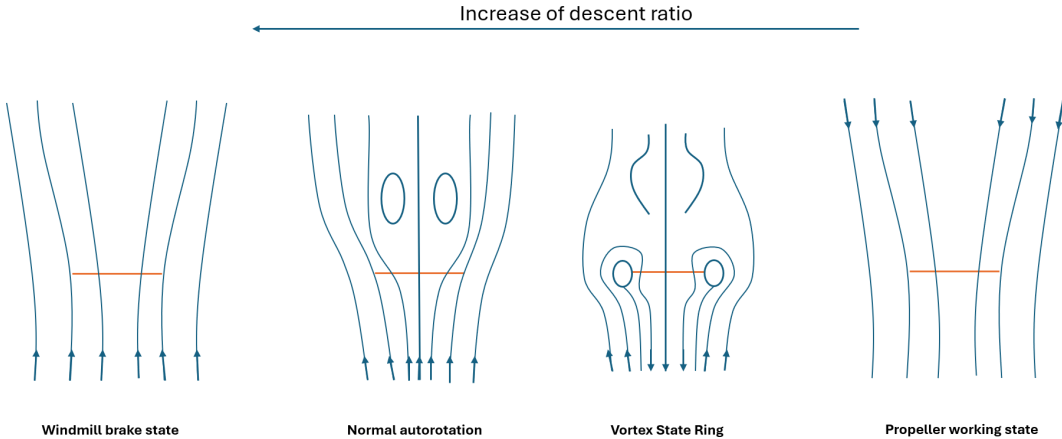
Figure 4.1: Inflow development in axial flight

As known from theory and described by many authors, momentum theory is incompatible with the calculation of inflow in the region where the rate of descent is between $-2 \leq$

$V_z/v_h \leq 0$. In this section, in fact, the evolution of the inflow through the rotor strongly depends on the vertical speed, as shown in figure 4.1. Although for small rates of descent the flow through the rotor is smooth, when the axial velocity is about equal to the inflow, the wake can no longer be convected away. In this situation, air recirculation is then observed, causing vibrations, loss of blade thrust and an increase in the rate of descent. If the axial velocity were to increase again, then the wake would be ejected from the rotor and the airflow through the blades would be smooth again, but with the opposite direction to the small descent rates.

The criticality of the descent phase is a decrease in the relative angle between the blade and the incident flow, resulting in a reduction in local lift. This results in a sudden loss of thrust and a significant increase in the helicopter's rate of descent until the vortices are dissipated and proper flow through the rotor is restored. Furthemore, it can be seen an increase of the power required by the rotor due to the increase in torque and the thrust fluctuations. Looking at the figures 4.3 and 4.7, it should be noted that the section where the curve assumes a negative slope is the most critical for the development of the VRS. In fact, an increase in the descent speed corresponds to an increase in the inflow speed, with a consequent reduction in the angle of attack of the blades and a loss of rotor thrust. This can be seen in the figure 4.2.
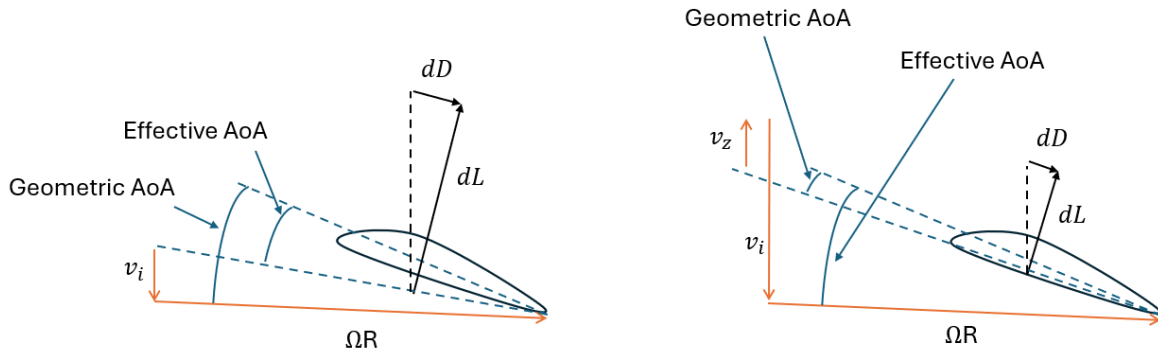
Figure 4.2: Incidence variation due to induced velocity in descent flight

In literature many models are described. Leishman [7] proposed to fit the two branches of Momentum Theory related to climb and descent flight through a fourth degree polynomial of the type:

$$\frac{v_i}{v_h} = k + k_1 \left(\frac{V_c}{v_h}\right) + k_2 \left(\frac{V_c}{v_h}\right)^2 + k_3 \left(\frac{V_c}{v_h}\right)^3 + k_4 \left(\frac{V_c}{v_h}\right)^4 \qquad (4.1)$$

where the $k_1 = -1.125, k_2 = -1.372, k_3 = -1.718, k_4 = -0.655$ are given to best fit experimental data.

Instead, Jimenez and Taghizad [19] proposed a model to describe VRS development in the presence of forward flight. First the inflow is evaluated by solving the following equation:

$$1 = \lambda^2[\mu^2 + (\lambda + \mu_z)^2] \tag{4.2}$$

Then, the VRS boundaries are predicted with the following relation:

$$\sqrt{\left(\frac{\mu}{k}\right)^2 + \left(\frac{\lambda}{2} + \mu_z\right)^2} \leq \epsilon \tag{4.3}$$

where $k > 1$ and the threshold ϵ are evaluated thanks to flight test available.

Other two models are presented by Young and Johnson, as described in the next sections.

4.2 Young's aproximation

Young's model, figure 4.3, is based on the linear interpolation of flight test campaigns data carried out by Castles and Gray [25]. Normalising speeds with respect to blade tip speed, ΩR, it approximates the sections of the region between $-2 \leq -\mu_d/\lambda_h \leq 0$ with straight lines.
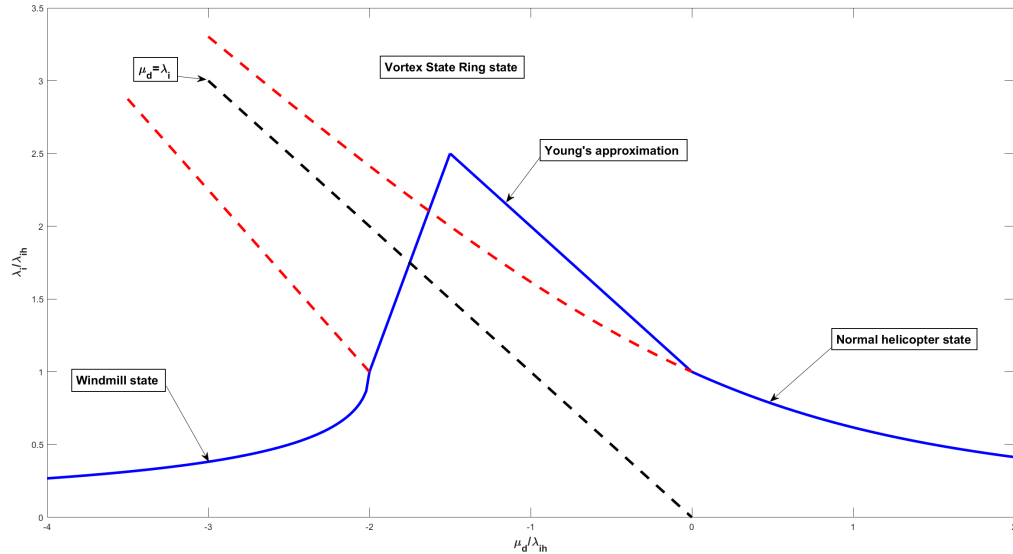
Figure 4.3: Young's model

As described by Padfield [6], it is given by the following equations:

$$\lambda_i = \lambda_{i_h}\left(1 + \frac{\mu_d}{\lambda_{i_h}}\right), \quad 0 \leq -\mu_d \leq -1.5\lambda_{i_h} \tag{4.4}$$

$$\lambda_i = \lambda_{i_h}\left(7 - 3\frac{\mu_d}{\lambda_{i_h}}\right), \quad -1.5 < -\mu_d \leq -2\lambda_{i_h} \tag{4.5}$$

One important feature of that model is the identification of the point of ideal autorotation when $\frac{\mu_d}{\lambda_{i_h}} = 1.8$. This can not be taken into account by the Momentum Theory.

Thanks to its descriptive simplicity, the implementation of this algorithm is particularly convenient from the perspective of code integration and computational cost, providing a good estimate of the inflow for the considered descent rate. However, since it relies on Momentum Theory, it cannot account for unsteady effects such as vortex dynamics or more complex aerodynamic interactions. Its use is therefore possible to estimate the region where the VRS might occur, allowing for the prevention of the aircraft's entry into it. Outside of the range described by equations 4.4,4.5, Momentum Theory for axial flight is used as described by 2.24.

The validity of this model lies in the axial flight region alone and one of the most important limitation of the model is that it identifies the upper limit of the vortex state ring region in the hovering situation. Unlike other more faithful models, this one is more conservative and the quality of the results is compromised by this too loose boundary. Should a limit be set to consider a minimum forward speed, the results show an excessive inflow variation which is followed by an higher rate of climb variation.This can easily be seen in the figure 4.4, where it can be observed that as the maximum threshold increases, there are greater peak of rate of climb. With regard to the activation of the VRS, as the threshold increases, it is active for a longer period of time, as shown in figure 4.5.
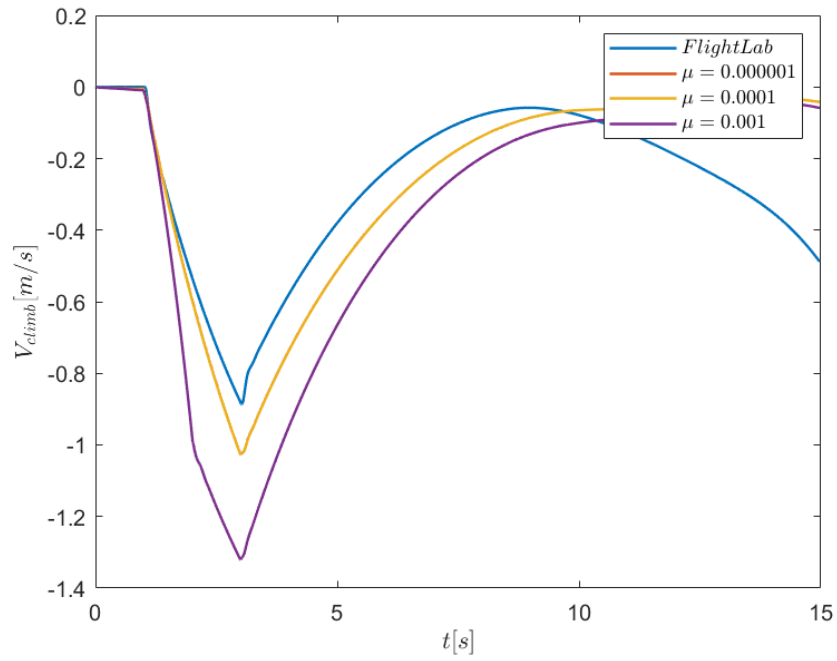
Figure 4.4: Variation of the climbing velocity with respect of the advance ratio
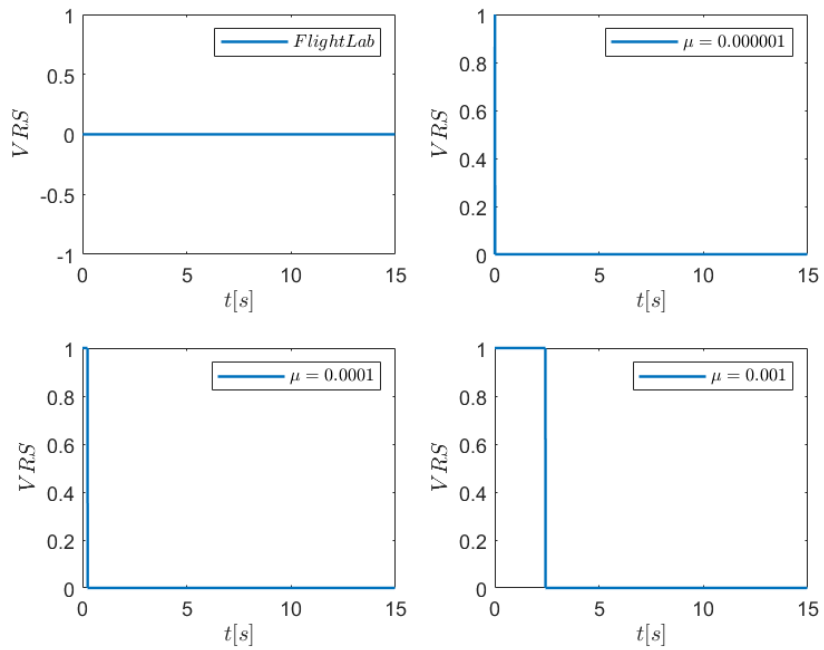
Figure 4.5: Variation of the VRS activation with respect of the advance ratio

4.3 Wayne Johnson model

The model proposed by Johnson is primarily aimed at implementation in real-time simulators. It is therefore particularly suitable for developing training simulators to test the aircraft's entry into the VRS and the recovery maneuvers to exit it. As described in [17], the model was developed based on flight tests conducted on helicopters and tiltrotors. The developed algorithm is thus capable of correctly approximating the experimental data knowing VRS envelope ranges, which are obtained for the aircrafts studied as can be seen in the figure.
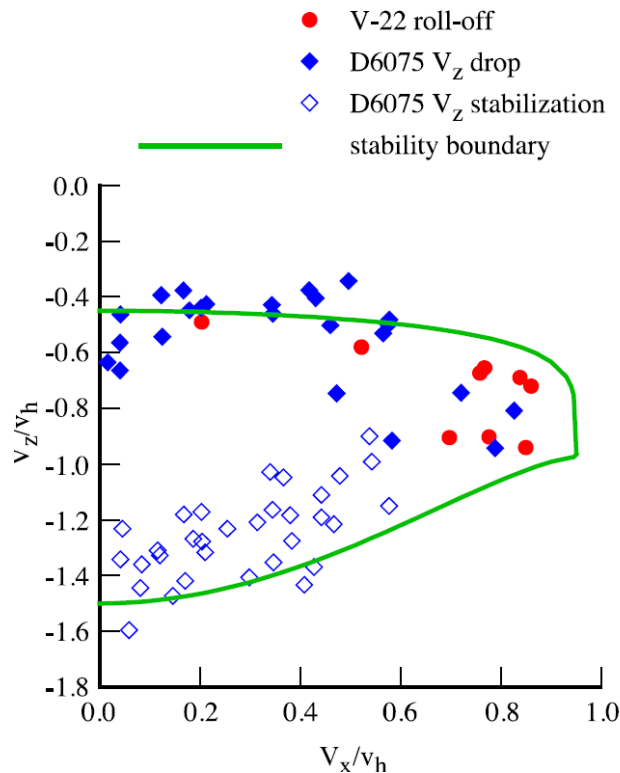
Figure 4.6: VRS boundaries found by Johnson [17]

The algorithm presented is capable of taking into account flight conditions that are not purely axial, being therefore particularly useful as the VRS is also able to develop in these situations with a minimum forward speed. Constraints must therefore be imposed for the maximum and minimum axial velocity and for the forward speed. Having found these, the model proposes to eliminate the singularity corresponding to the autorotation regime by merging the curves obtained from Momentum Theory with the new one at the point of null derivative. Subsequently, the third-degree polynomial is obtained so that it best interpolates

the experimental data.

4.3.1 Algorithm description

First, the algorithm proposes to eliminate the singularity given by the ideal autorotation point for axial flight. This is done by constructing an initial curve to be used in subsequent calculations. As shown in figure 4.7, this is the red baseline curve. This type of polynomial is also used to construct the negative slope of the blue curve, i.e. the curve describing the variation of the inflow in the Vortex Ring State. To eliminate the singularity, a constraint on the forward velocity is first imposed. Two points are found on the two branches described by the momentum theory, which are connected by the interpolating polynomial. It is observed that as the speed increases, the two points move towards each other, so that the area of invalidity becomes narrower and the slope of the curve becomes less steep. The polynomial used to construct the baseline curve is as follows:

$$V_z + v = V_z \left(aV_z^2 - b + cV_x^2 \right) \tag{4.6}$$

It is related to the Momentum Theory curves in the following way. At point A, the constraint that the inflow velocity is equal to the derivative of the inflow variation with respect to the vertical velocity is satisfied, while at point B, only the correspondence of the inflow to the value described by momentum theory is sought.

In addition to the constraints defined by points A and B, constraints on the forward and descent speeds are also identified, resulting in three characteristic speeds. The maximum and minimum increases in the inflow variation observed during the VRS are calculated from those on the descent speed. Two further points are then identified to connect the baseline curve and the inflow polynomial, D and E. Evaluated inflow is then given by the following equation:

$$\lambda = k \left(\lambda_{base} + f \Delta \lambda_{VRS} \right) \tag{4.7}$$

where $k > 1$ takes into account for additional losses while $f > 0$ allows a reduction of the instability caused by the VRS. In the current model, due to the lack of flight tests to validate the model for the specific case of the Bell 412, these two parameters are both set to 1.
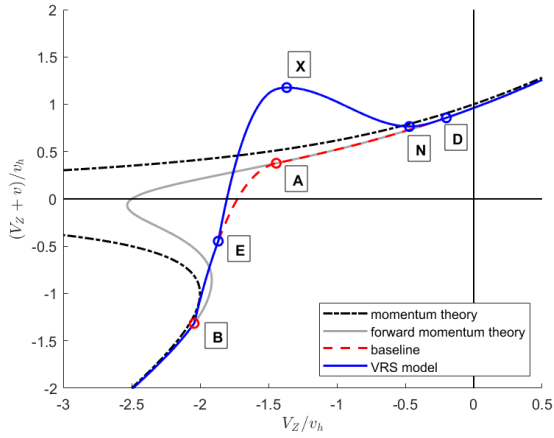
(a) Johnson VRS model
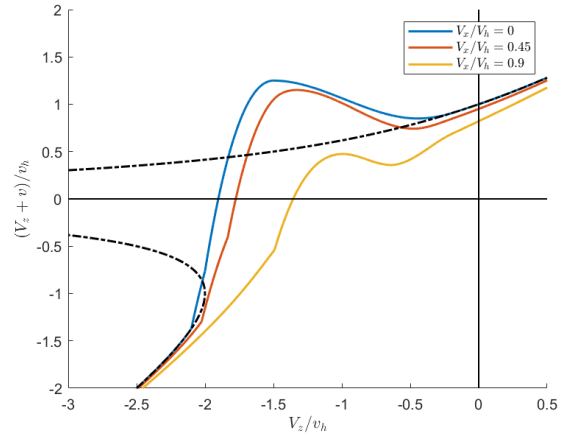
(b) Effect of forward velocity variation

Figure 4.7: Johnson Vortex Ring State model

Figure 4.8 shows the algorithm's flowchart used for constructing the two polynomials, given the velocity V_z and V_x and assuming $V_{zA} > V_{zB}, V_{zD} > V_{zN} > V_{zX} > V_{zE}, V_{zA} \geq V_{zB}$. Regarding the characteristic velocities, values used are described in the paper and are reported in the table 4.1

point	parameter	values
	Baseline Model	
A	V_{zA}	-1.5
B	V_{zB}	-2.1
C	V_{xC}	0.75
	VRS Model	
D	V_{zD}	-0.2
N	V_{zN}	-0.45
	$(V+v)_N$	1.25
E	V_{zE}	-2
M	V_{xM}	0.95

Table 4.1: Speed thresholds

Figure 4.8: Johnson algorithm's flowchart

73

4.3.2 Implementation

The Simulink's implementation was carried out as follows. Due to the lack of available flight tests for the Bell412, ranges described in the paper were considered valid. Then, in a Matlab script, the baseline and VRS curve described by the algorithm were calculated as shown in figure 4.8.The calculated vectors, containing the values of $(V_z + v)/v_h$ and V_z/v_h, were then passed to the model as variables. During the simulation, calculation of the vertical velocity gives the x-coordinate of the graph, and this is used to find the corresponding y-value by matching the position inside the vectors. Data contained in the vector are instead linearly interpolated if there is no exact match between the calculated coordinate and the corresponding value in the vector.

4.3.3 Model weaknesses

The model described, being based on Momentum Theory, considers a uniform flow and is unable to evaluate an unsteady three dimensional flow. Furthermore, within the VRS development region, vibrations developed by aerodynamic instability should be taken into account. To further improve the model during the development of the VRS, Johnson suggested only the introduction of factors k and f that take into account additional aerodynamic dissipations compared to the ideal case. In this case, there is no oscillatory character, as might be expected, but simply a deterioration in performance evaluated as described by 4.7. Other models exist in the literature which describe this phenomenon more precisely. Basset [18], for example, proposed the introduction of an harmonic function to take into account vibrations and the oscillatory nature of the thrust variation. This is then given by:

$$\lambda_i = \sum_{i=1}^{n} A_i cos\left(\omega_i t + \phi\right) \tag{4.8}$$

Magnitude and phase can be evaluated on the basis of flight tests. If it were possible to carry out this type of test in the future for the Bell 412, it would be useful to include this last part in the model.
Another lack of the model is its inability to take into account the geometric factors of the rotor and blades. In fact, the algorithm is purely based on speed thresholds used to interpolate the experimental data. It is therefore not possible to assess how the geometric characteristics of the blades affects the resulting inflow variation.

4.4 Model validation

Initially, the two models were validated by comparing the results obtained with those derived from FlightLab simulations. In particular, three different simulations were carried out with a step command held for two seconds with amplitudes of 0.25, 0.5, 0.75 inches, as shown in figure 4.9. In this way, starting from the trim hover condition reported in 3.1 , a descent rate was imposed in order to evaluate the climbing velocity and to assess whether or not entry into the Vortex Ring State had occurred. Two types of graphics are then presented. The first show the evolution of the descent rate during the simulation, while the second represent the activation of the VRS flag.

Next, the results obtained by increasing the application time of the collective reduction are shown. In this case, there is no comparison with the FlightLab simulations, only a comparison with the results of the Johnson model.

In the last section, Johnson model is compared with FlightLab simulations for larger collective reductions of 1,2,3 inches. In this case, the input is given for 4 seconds and not only hover but also advanced flight is considered.
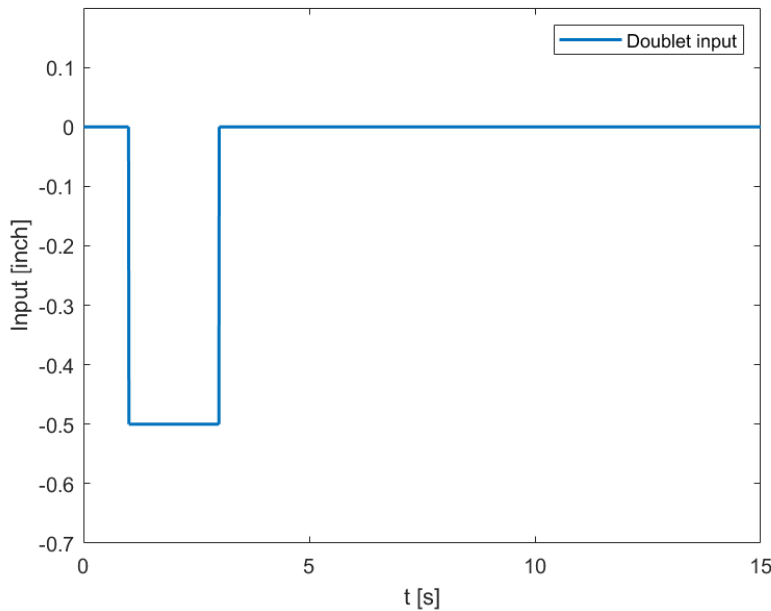
Figure 4.9: Collective reduction to activate the VRS

4.4.1 Johnson and Young model comparison with FlightLab

0.25 inches
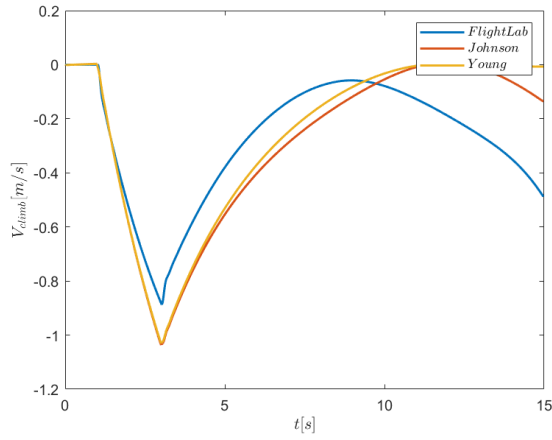
(a) Climbing velocity
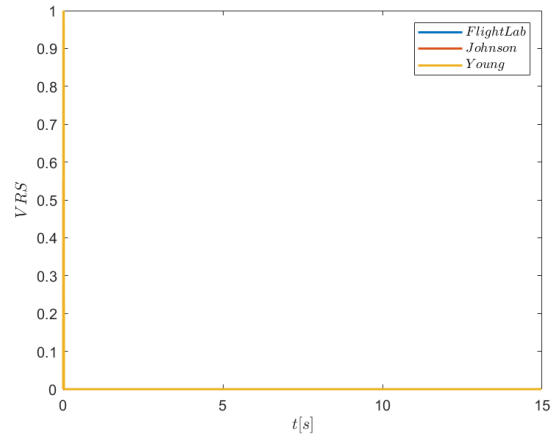
(b) Activation VRS flag

Figure 4.10: Response to an input of 0.25 inches

0.5 inches
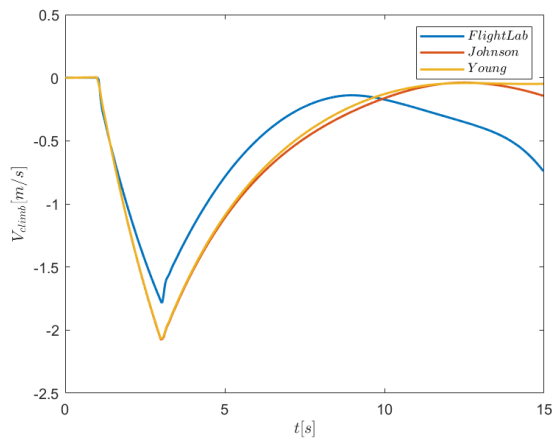
(a) Climbing velocity
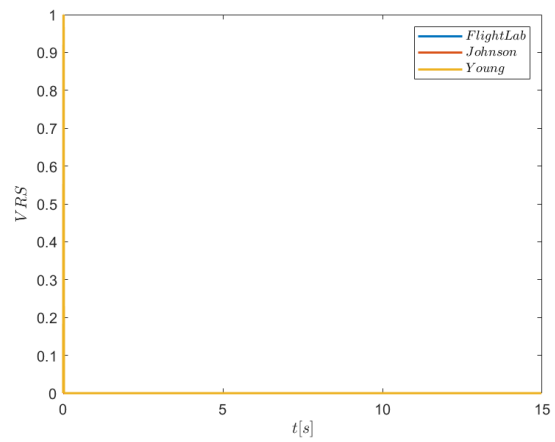
(b) Activation VRS flag

Figure 4.11: Response to an input of 0.5 inches

0.75 inches
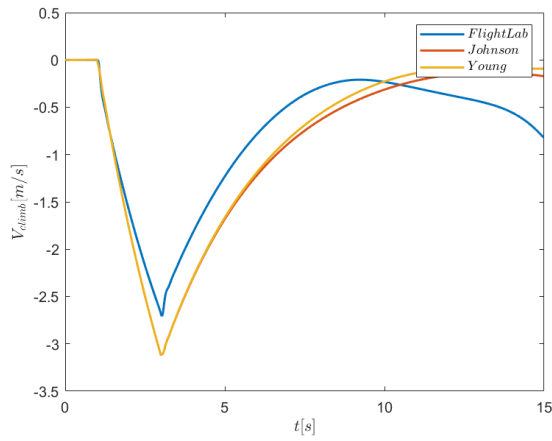
(a) Climbing velocity
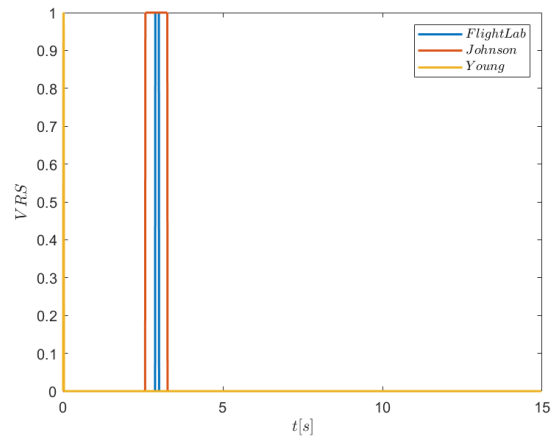
(b) Activation VRS flag

Figure 4.12: Response to an input of 0.75 inches

4.4.2 Variation of collective reduction

0.25 inches
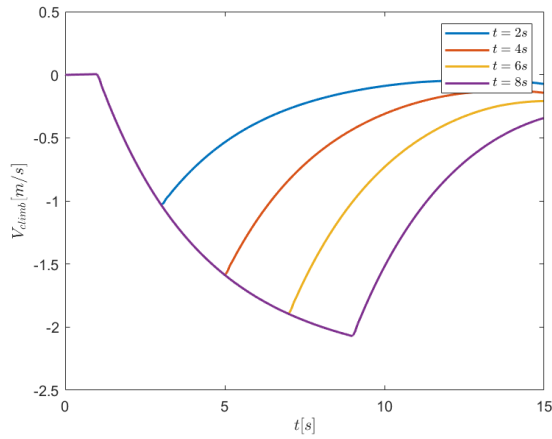
(a) Climbing velocity
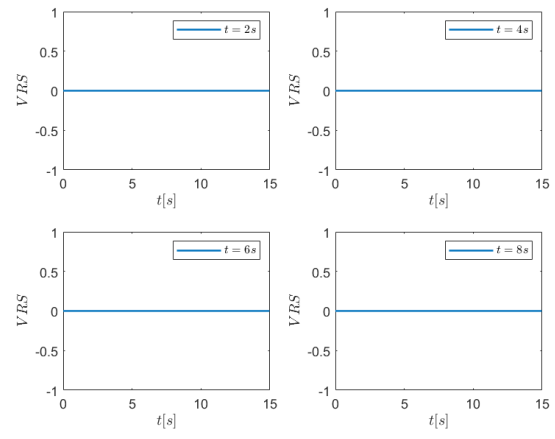
(b) Activation VRS flag

Figure 4.13: Comparison with different time of collective reduction for the 0.25 inches case

0.5 inches
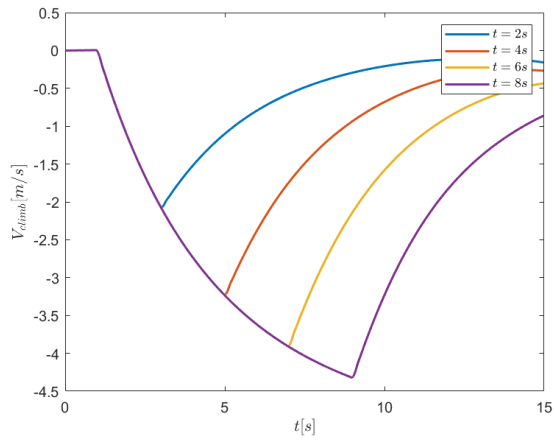
(a) Climbing velocity
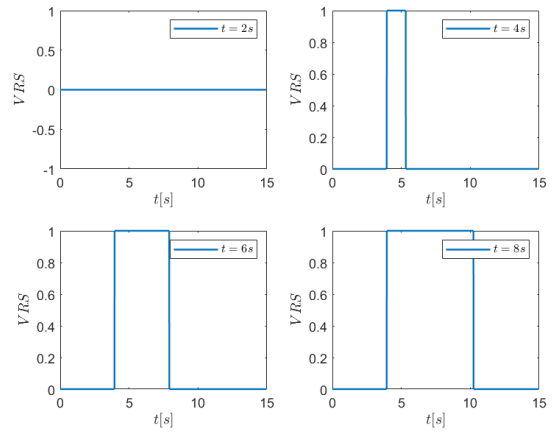
(b) Activation VRS flag

Figure 4.14: Comparison with different time of collective reduction for the 0.5 inches case

0.75 inches
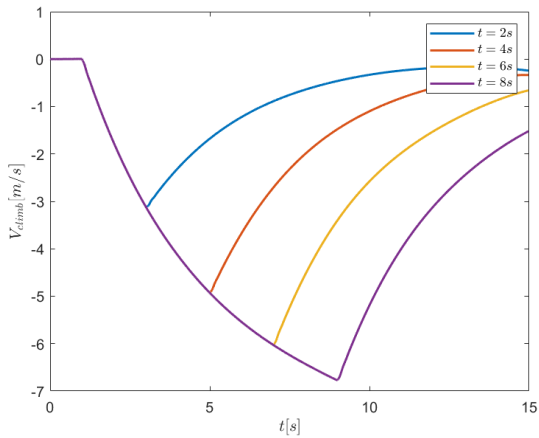
(a) Climbing velocity
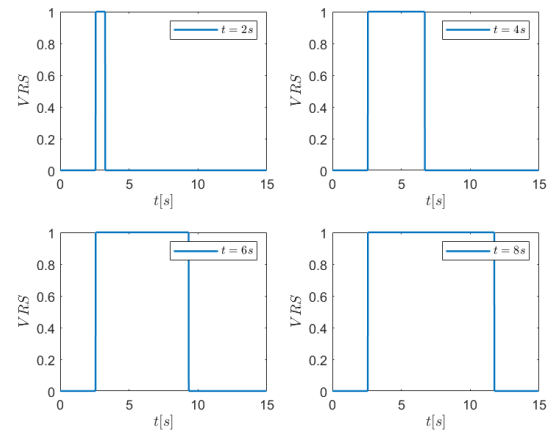
(b) Activation VRS flag

Figure 4.15: Comparison with different time of collective reduction for the 0.75 inches case

4.4.3   Johnson model comparison with FlightLab

1 inch collective reduction

(a) Climbing velocity

(b) Activation VRS flag
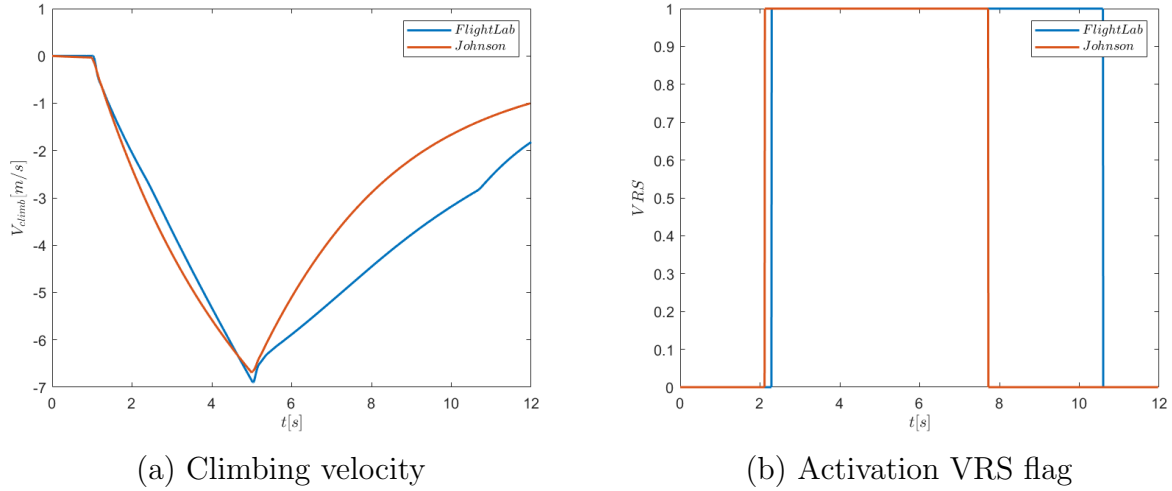
Figure 4.16: Response to a 1 inch collective reduction in the hover condition

(a) Climbing velocity

(b) Activation VRS flag
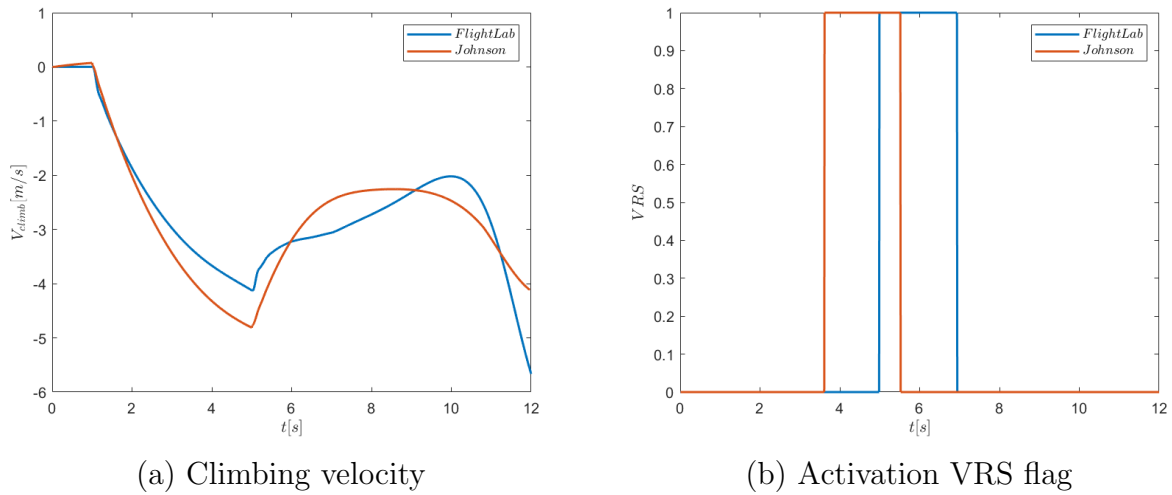
Figure 4.17: Response to a 1 inch collective reduction in the 20 knots condition
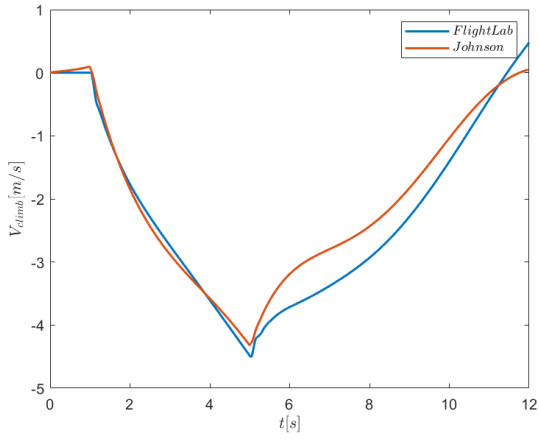
(a) Climbing velocity
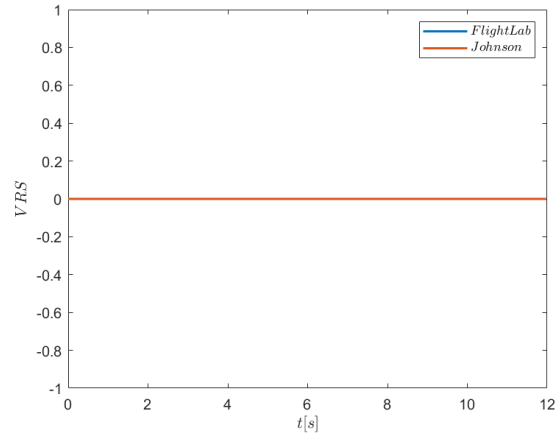
(b) Activation VRS flag

Figure 4.18: Response to a 1 inch collective reduction in the 40 knots condition
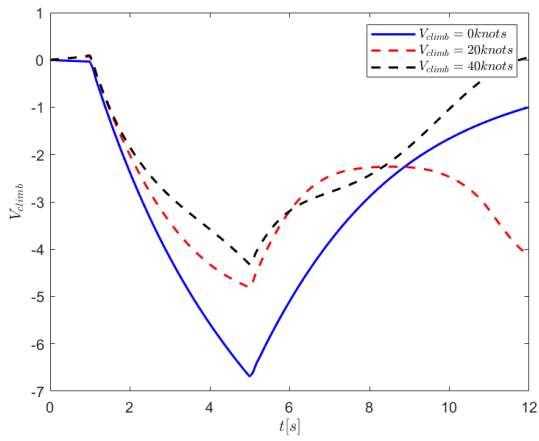
(a) Climbing velocity
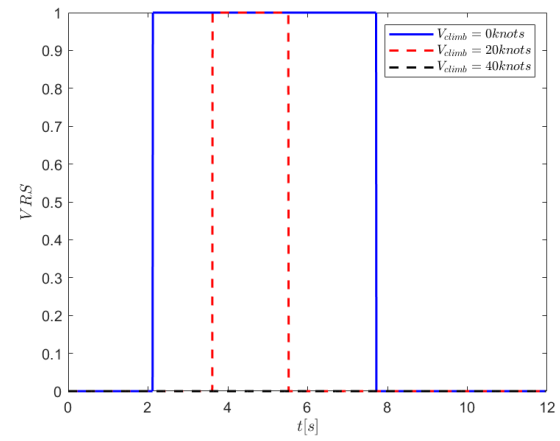
(b) Activation VRS flag

Figure 4.19: Response to a 1 inch collective reduction for different flight conditions

2 inches collective reduction
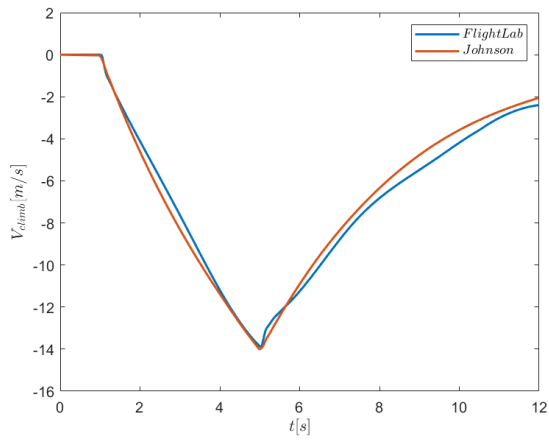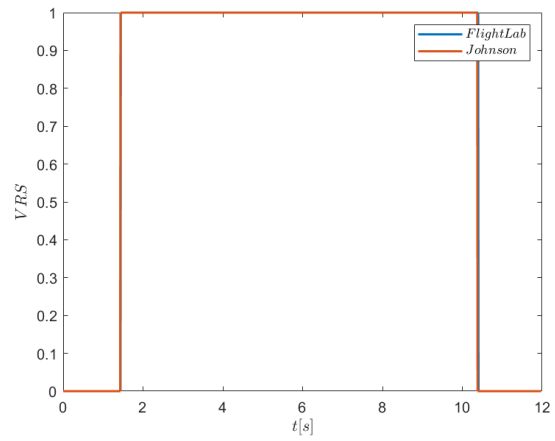
(a) Climbing velocity   (b) Activation VRS flag

Figure 4.20: Response to a 2 inches collective reduction in the hover condition
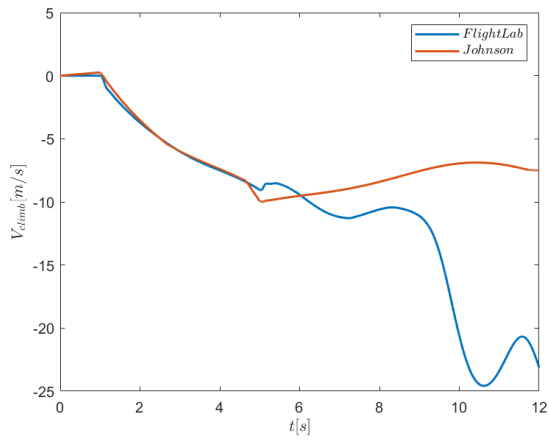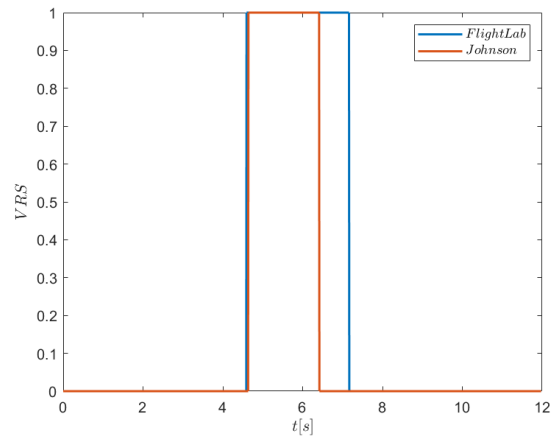
(a) Climbing velocity   (b) Activation VRS flag

Figure 4.21: Response to a 2 inches collective reduction in the 20 knots condition
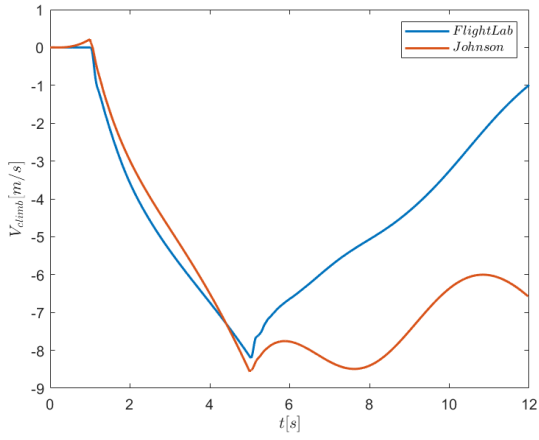
(a) Climbing velocity
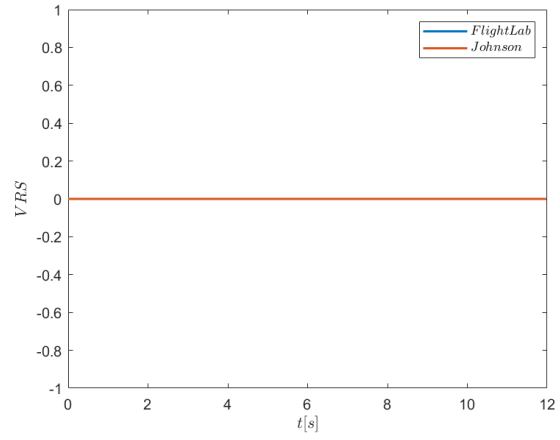
(b) Activation VRS flag

Figure 4.22: Response to a 2 inches collective reduction in the 40 knots condition
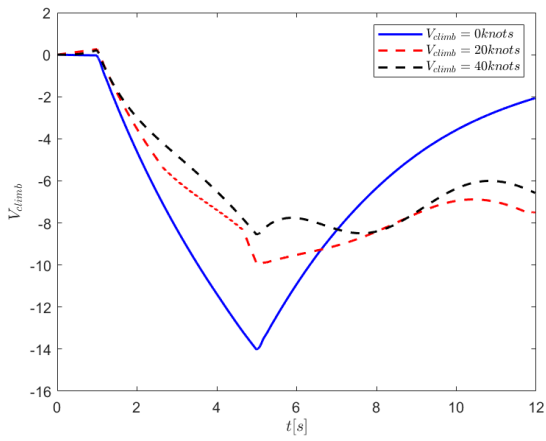
(a) Climbing velocity
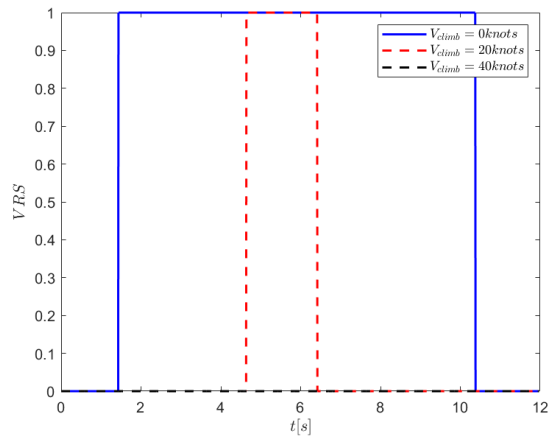
(b) Activation VRS flag

Figure 4.23: Response to a 2 inches collective reduction for different flight conditions

3 inches collective reduction
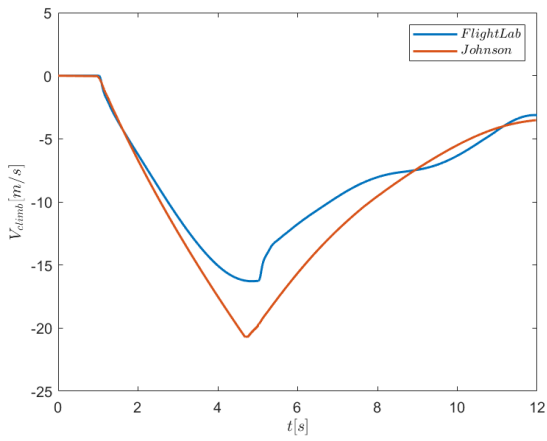
(a) Climbing velocity
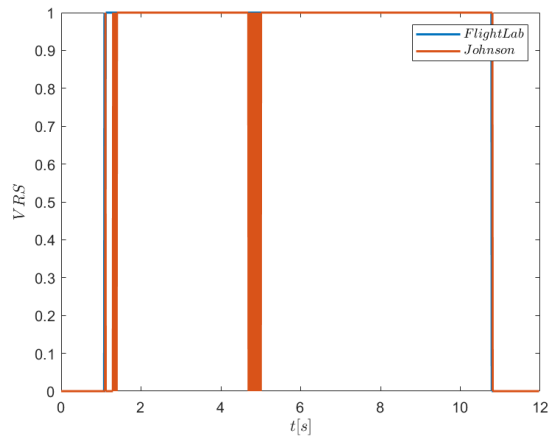
(b) Activation VRS flag

Figure 4.24: Response to a 3 inches collective reduction in the hover condition
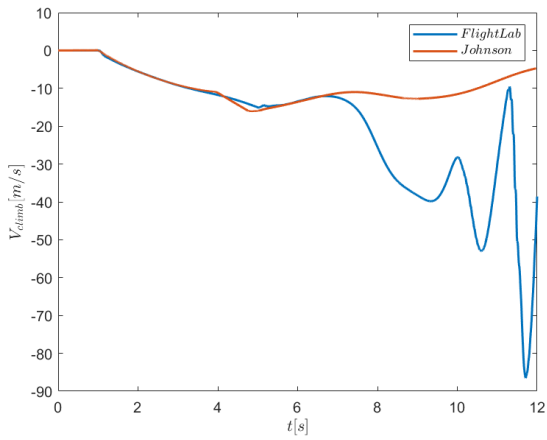
(a) Climbing velocity
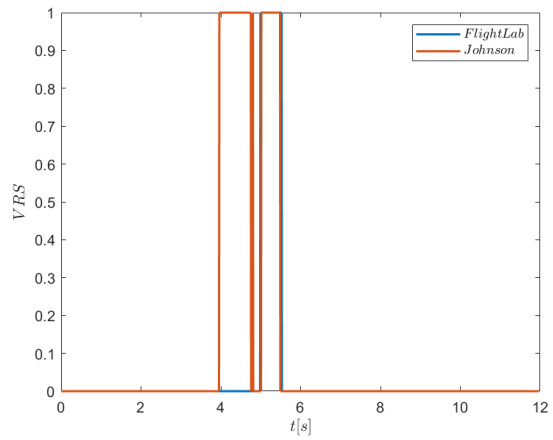
(b) Activation VRS flag

Figure 4.25: Response to a 3 inches collective reduction in the 20 knots condition
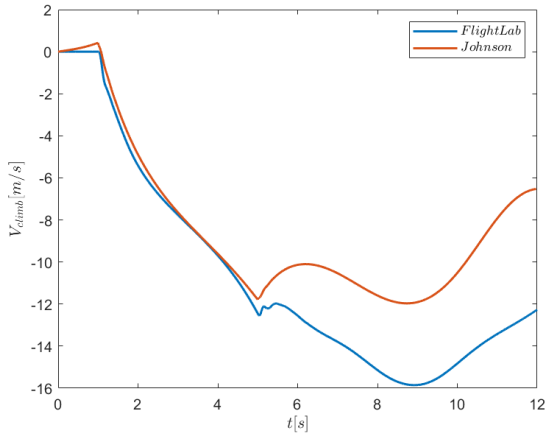
(a) Climbing velocity
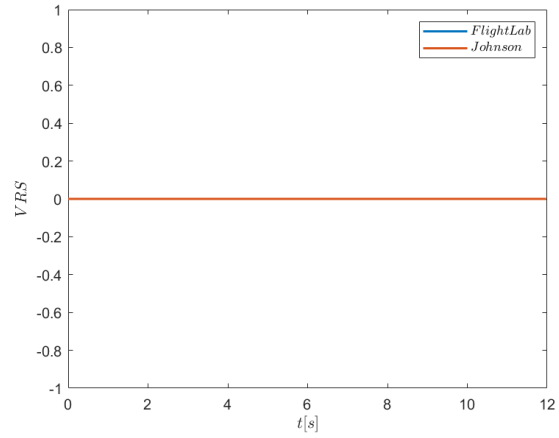
(b) Activation VRS flag

Figure 4.26: Response to a 3 inches collective reduction in the 40 knots condition
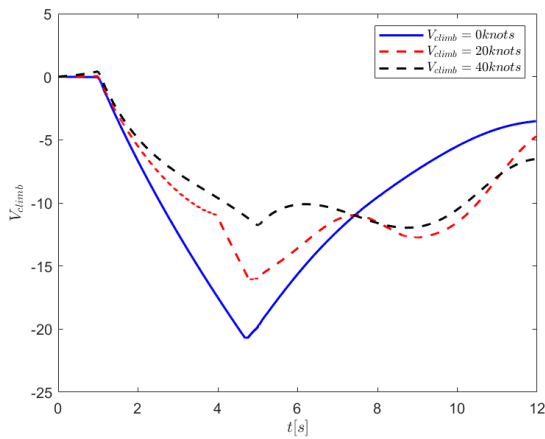
(a) Climbing velocity
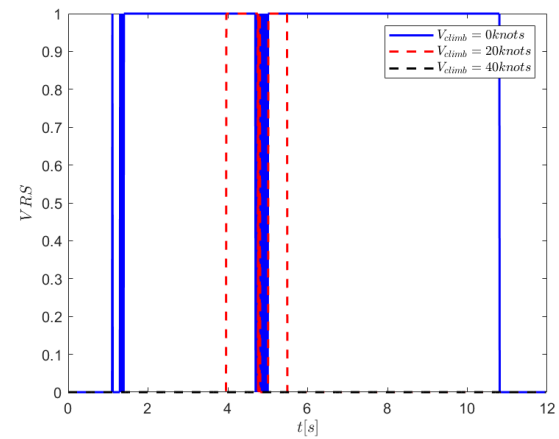
(b) Activation VRS flag

Figure 4.27: Response to a 3 inches collective reduction for different flight conditions

4.4.4 Analysis of the results

In section 4.4.1, a comparison of the two models immediately shows that in the case of VRS activation, Johnson's model is fully successful in describing this phenomenon. In the first two cases studied, the results are identical to those of FlightLab and the VRS is not activated. As for the last benchmark, however, there is activation of the VRS at a speed of 2.54 m/s, as shown by FlightLab in figure 4.12, corresponding to the threshold of 500 ft/min typical of the Bell 412 for hover. Considering the case of a collective reduction held for two seconds, it can be seen that the helicopter only enters the VRS state at an input amplitude of 0.75

inches, which is the only one capable of providing a sufficiently high rate of descent for this state to develop. In the latter case, the difference in activation time is about half second, due to difference in the response of the two models. This can be due to a worst approximation of the inflow calculation in the model developed then the one used in FlightLab. However, the activation threshold corresponds to the values predicted by theory, confirming the validity of the model.

As far as Young's model is concerned, it is not suitable to describe the activation of the Vortex Ring State. In fact, in each of the simulations carried out, it can be observed that the flag is activated at the first instant, only to be extinguished in the remaining part of the simulation. This is due to the fact that Young's model is only valid for a purely axial flight, which is why the flag is active at instant zero. In fact, the simulation is run from trim conditions which, for hovering, involve zero forward velocities on all three axes. As soon as a minimum speed is reached, the code enters the advanced flight section, where the way the inflow is calculated changes and the flag is deactivated.

It can be observed that the change in climb rate is almost completely identical for both models, as shown in figure 4.10,4.11, 4.12. This can be attributed to the fact that Young and Johnson algorithm are extensions of Momentum Theory, both considering a uniform inflow and neglecting 3D unsteady effects. However, the model presented by Johnson shows a slightly bigger difference compared to that of Young.

Looking at the results of section 4.4.2, it can be seen that the time variation for which the collective is lowered greatly affects the helicopter's entry into the VRS. As far as the variation of 0.25 inches is concerned, as shown in figure 4.13, this is in no way sufficient to activate this state. It is different for the input condition of 0.5 inches, as can be seen in figure 4.14, whereby a reduction for a time greater than 2s activates the VRS. The longer the time, the longer the state. As far as the 0.75 inches variation is concerned, as in figure 4.15, a larger collective reduction allows this phenomenon to be better observed, in contrast to the results presented in figure 4.12 where it only occurs for about 0.5s. For this last case, it is easier to appreciate the loss of altitude caused by the VRS entry, as shown in figure 4.28. It can be seen that in the case of a collective reduction of only two seconds, the model predicts a very short VRS development. This is in fact about 13 metres and is the normal response to a command reduction of this type. As time increases, however, more significant altitude losses are observed, ranging from 30 to over 60 metres.

In section 4.4.3, Johnson's model is compared with FlightLab for different types of input than in the previous section, as well as for the advanced flight condition. Young's model was not considered since, as seen above, it is only valid for the ideal case of pure axial flight. In
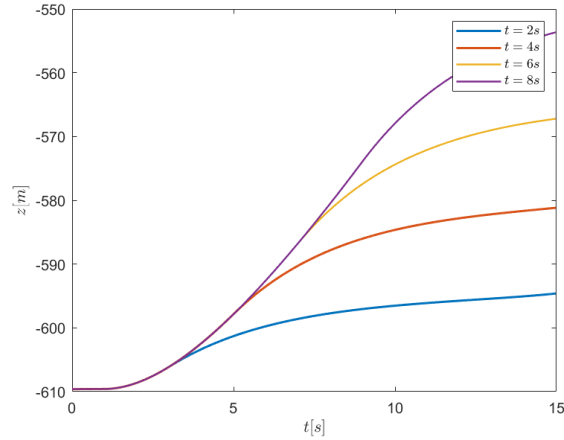
Figure 4.28: Loss of altitude after a 0.75 inches collective reduction

the case of fixed-point flight, the cases studied always allow for the observation of the VRS. In this condition, the model's response is quite consistent with that seen in FlightLab, both in terms of climbing speed and flag activation. The best response occurs for a variation of 2 inches, while in the case of a smaller reduction there is an anticipation of the response and in the case of a larger reduction there is a delay. In all three cases, the VRS occurs over a very long period of time, and it can be seen that this results in a very significant loss of altitude as shown in figure 4.29.
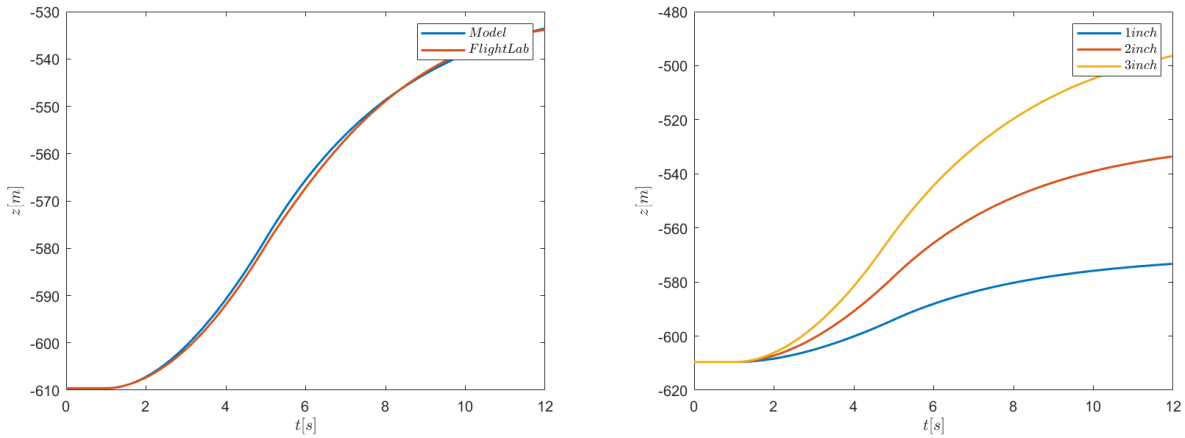
(a) 2 inch collective reduction

(b) Response to different collective reduction

Figure 4.29: Altitude loss during VRS development

Looking at the figure 4.30, the effect on altitude loss can be observed due to a collective 1 inch reduction at different speeds. It can be seen that at higher speeds, such as 20 knots,

the VRS has a greater effect even though it occurs for less time. In fact, the loss of altitude is about the same in the hover and 20 knots case, although in the hover phase it is active for about six seconds, while in the 20 knots case for about 2, as shown in figure 4.19. In the case of a speed of 40 knots, as the unsteady condition does not occur, the loss of altitude is in accordance with the response expected for an input such as that given. Furthermore, it can be observed that in the case of fixed-point flight, a greater reduction in collective corresponds to a more prolonged development of the VRS. The opposite happens in forward flight, as shown by the results for 20 knots. In fact, a higher amplitude command generates a greater velocity change and a sudden increase in the rate of descent, causing the vortices that accumulate in the rotor plane to be swept away more quickly.
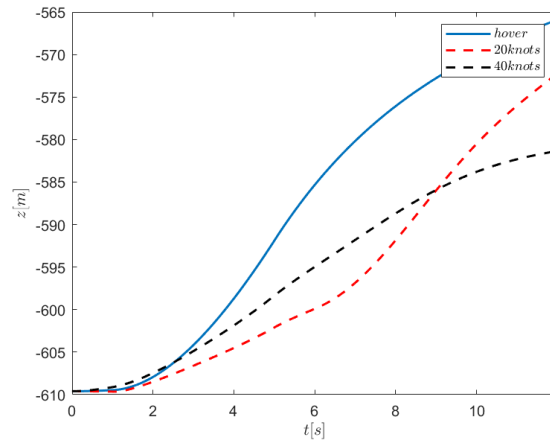
Figure 4.30: Loss altitude at different speed due to a 1 inch collective reduction

As for the advanced flight condition, only in the case of 20 knots is it possible to enter the VRS for all three cases. Looking at the climb speed in figure 4.17,4.21,4.25, its trend in the initial phase of the simulation is consistent with that of FlightLab. Following the activation of the VRS, however, the two models diverge. In FlightLab, in fact, the curves diverge significantly and the observed instability is very pronounced, in contrast to the developed model which is more stable. In this case, in fact, the instability is not able to make the model diverge sharply, but there is a slower divergence. In the 40 knots case, on the other hand, the flight speed is too high for VRS to be established. The vorticity, in fact, as explained by theory, is swept away and does not have time to remain in the plane of the rotor and influence the response of the blades.
On the other hand, if we look at the linear and angular velocity trends, in the case of a 1 or 2 inch reduction, the response presented by the model is more stable than that of FlightLab, while in the case of a 3 inch reduction, the response is the opposite, as shown in figure 4.31.
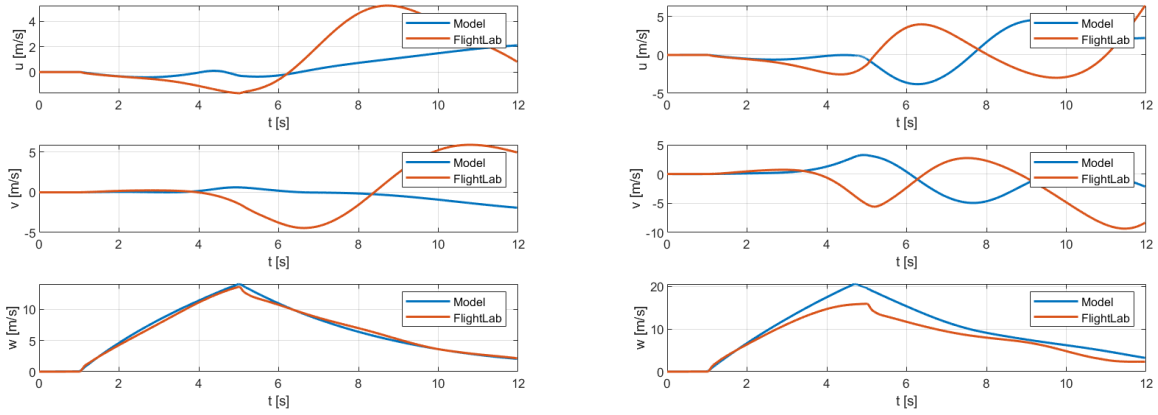
(a) Linear velocities-2 inches collective reduction

(b) Linear velocities-3 inches collective reduction

Figure 4.31: Comparison of the linear velocities for different collective reduction

In this case, it can be seen again how the lack of dynamic inflow affects the model's response.

4.5   Recovery manouvers

As seen in the previous sections, the helicopter's entry into the VRS results in a significant loss of altitude and an unwanted increase in descent speed, which can degenerate into uncontrolled aircraft divergence. Two types of manoeuvres are typically used for vortex recovery. Both aim to increase the rate of descent in order to expel vortices from the blade plane and restore a proper inflow regime through the rotor.

The Vuichard Recovery procedure

As reported in [24], this manoeuvre has three stages:

– Increase the collective and therefore the pedal to maintain the heading.

– Apply a cyclic lateral input between 10 and 20 degrees to impose a lateral movement.

– The manoeuvre ends when the advancing blade reaches the upward flow of the vortex.

This procedure, if carried out correctly, will result in a loss of altitude of between 20 and 50 feet, depending on the time taken.

Recovery in autorotation regime

Similar to the manoeuvre described above is the manoeuvre in which the helicopter enters autorotation [21]. First, a longitudinal cyclic input is applied to cause a pitch down and increase the rate of descent. Then, once the rotor is in autorotation regime and the airflow through the rotor is completely restored, a collective increase cancels the descent speed.

Chapter 5

Conclusion and future works

In this thesis, a non-linear dynamic model of the Bell 412 helicopter has been developed and successfully validated. It promises to be a preliminary model for the development of a training and research simulator. For this purpose, a Vortex Ring State algorithm was correctly implemented and validated, as reported in chapter 4. As for the simulated components, they show a concordance of results with FlightLab, an high-fidelity simulator used for validation. The two rotors show dynamics that are generally consistent with those expected, but are more damped in the case of the main rotor and slightly overestimated in the case of the tail rotor. In addition, due to the lack of dynamic inflow in the main rotor, there is a non-uniformity in the roll and pitch response following longitudinal and lateral cyclic commands, while the on-axis response is entirely satisfactory. However, this dynamic is not such as to affect the quality of the results shown following a collective command, which is fundamental to the analysis of the VRS. For this reason, the dynamic inflow was not considered essential for the continuation of the project. The VRS model developed is based on the algorithm developed by Johnson and is capable of considering both the fixed point and advanced flight cases. It is therefore capable of covering the full range of possible evolution of this transient condition. The flight ranges within which the VRS can evolve are also taken from Johnson's work and these generally show a correspondence of results with those predicted by FlightLab. The most critical problems occur in advanced flight, where the model is unable to observe a correct divergence of states, but is more stable. The reason for this was found to be the lack of a model that correctly evaluates the effect of the downwash on the stabilisers and the fuselage. In fact, the simulations initially show results consistent with those of FlightLab, but then deviate from mid-simulation onwards. In any case, the implemented model provides entirely satisfactory results and can therefore be considered valid.

In view of the results obtained, it is recommended to implement modifications to the model in order to increase the fidelity of the simulator. In particular, the following improvements are recommended:

- Implementation of an engine model that can take into account the variation of angular velocity and torque.
- Implementation of a more accurate mathematical model to describe the flapping dynamics. This can be done either in a multi-blade coordinate system or in a single-blade coordinate system.
- Implementation of a mathematical model for the coupling of lead-lag and flapping dynamics.
- Implementation of a dynamic inflow to achieve better coupling of roll and pitch dynamics.
- Implementation of a more accurate wake model than that described by simple gain tuning.
- Implementation of a model that more accurately describes the flapping dynamics of the tail rotor.
- Implementation of a function to takes into account vibration during the development of the VRS.

Bibliography

[1] W.T.Korek,P.Beecroft,M.Lone,E.Bragado Aldana,A.Mendez,J.Enconniere,H.U.Asad, K.Grzedzinski,M.Mildere,J.Whidborne,W.-C.Li,L.Lu,M.Alam,S.Asmayawati,L.Del Barrio Conde,D.Hargreaves,D.Jenkins, Simulation Framework and Development of the Future System Simulator, The Aeronautical Journal, 2024, 128, pp.2754-2780

[2] Mushfiqul Alam, Michael Jump, Jonathan Rogers, Simulated Flight Trial Assessment of Novel Autorotation Cueing Methods using a Head Down Display, Vertical Flight Society 79th Annual forum Technology Display, May 2023

[3] Robert T.N. Chen, A Simplified Rotor System MAthematical Model for Piloted Flight Dynamics Simulation, NASA Technical Memorandum 78575, May 1979

[4] Peter D.Talbot, Bruce E. Tinling, Wiliam A.Decker, Robert T.N.Chen, A Mathematical Model of a Single Main Rotor Helicopter for Piloted Simulation, NASA techinal memorandum 84281, September 1982

[5] M.D.Takahashi, A Flight-Dynamic Helicopter Mathematical Model with a Single Flap-Lag-Torsion Main Rotor, NASA Technical Memorandum 102267, February 1990

[6] G.D.Padfield, Helicopter Flight Dynamics including a Treatment of Tiltrotor Aircraft, Third Edition, Wiley Editor, 2018

[7] J.Gordon Leishman, Principles of Helicopter Aerodynamics, Second Edition, Cambridge Aerospace Series, 2006

[8] F.J.Bailey, A Simplified Theoretical Method of Determing the Characteristics of a Lifting Rotor in Forward Flight, Report no. 716-National Advisory Committeefor Aeronautics

[9] Mark White, Linghai Lu, Gareth Padfield, Neil Cameron, Dheeraj Agarwal, Rotorcraft Simulation Fidelity, University of Liverpool, 30th September 2021

[10] Francesca Roncolini, Nonlinear Dynamic Model of an Unmanned Rotorcraft:Implementation and Validation, Politecnico di Milano, Department of Aerospace Science and Technology, Academic Year 2018-2019

[11] Alexander Crain, Joseph Ricciardi, Terrin Stachiw, Bell 412 Full Flight Envelope Aircraft Simulation Model DEvelopment and Evaluation with Non Linear Equations,International Mechanical Engineering Congress and Exposition IMECE2021, Virtual, Online, November 1-5,2021

[12] Jiyang Dai, Guohui Wu, Yinhua Wu, Guomin Zhu, Helicopter Trim Research Based on Hybrid Genetic Algorithm, 7th World Congress on Intelligent Control and Automation,Chongqing, China, June 25-27,2008

[13] Anil Demirel, Investigating Trim Algorithms for a Utility Helicopter, Graduate School of Natural and Applied Scienxed of Middle East Technical University, November 2019

[14] Robert T.N.Chen, A Survey of Nonuniform Inflow Models for Rotorcraft Flight Dynamics and Control Applications, NASA Technical Memorandum 102219, November 1989

[15] David A.Peters, David Doug Boyd, Cheng Jian He, Finite-State Induced-Flow Model for Rotors in Hover and Forward Flight, 43rd Annual Forum of the American Helicopter society, St.Louis, May 18-20,1987

[16] Alberto Torasso, Low-order Models and Numerical Techniques for the Analysis of Rotorcraft Flight Mechanics, PhD Dissertation, Politecnico di Torino, Maggio 2012

[17] Wayne Jhonson, Model for Vortex Ring State Influence on Rotorcraft Flight Dynamics, Army/NASA Rotorcraft Division, NASA Ames Research Center, AHS 4th Decennial Specialist's Conference on Aeromechanics, San Francisco, January 21-23,2004

[18] J.V.R. Prasad, Chang Chen, P.M. Basset, S.Kolb, Simplified Modelling and Non-Linear Analysis of a Helicopter Rotor in Vortex Ring State, 30th European Rotorcraft Forum, Marseilles, France, September 14-16,2004

[19] Jérémy Jimenez, André Desopper, Armin Taghizad, Laurent Binet, Induced Velocity Model in Steep Descent and Vortex-Ring State Predicition, Laboratoire ONERA-Ecole de l'Air, Base Aérienne 701, 13661 Salon Air-France

[20] Mark.D.Betzina, Tiltrotor Descent Aerodynamics:a Small-Scale Experimental Investigation of Vortex Ring State, 57th Annual Forum of the American Helicopter Society, Washington DC, May 9-11, 2001

[21] Skander Taamallah, A Qualitive Introduction to the Vortex-Ring State, Autorotation, and Optimal Autorotation, 36th European Rotorcraft Forum, Paris, France, September 7-9,2010

[22] Paul Mullen, Gianni Bernini, Vortex Ring State Prediciton and Analysis

[23] Albert Brand, Mark Dreier, Ron Kisor, Tom Wood, The Nature of Vortex Ring State, Journal of the American Helicopter Society 56,022001 (2011)

[24] United States Helicopter Safety Team, Airman Bulletin 'The Vuichard Recovery'

[25] Castles, W., Jr. and Gray, R.B., "Empirical Relation Between Induced Velocity, Thrust, and Rate of Descent of a Helicopter Rotor as Determined by Wind-Tunnel Tests on Four Model Rotors," NACA TN 2474, October 1951

Web Sites

[1] Constrained Non Linear Optimisation Algorithm, URL:https://it.mathworks.com/help/optim/ug/constrained-nonlinear-optimization-algorithms.html

[2] The Life of Igor Sirkowsky, https://sikorskyarchives.com/home/igor-sikorsky/